1617

Applications of Optical Wavefront Modulation with Deformable Membrane Mirrors

Frédéric Gonté

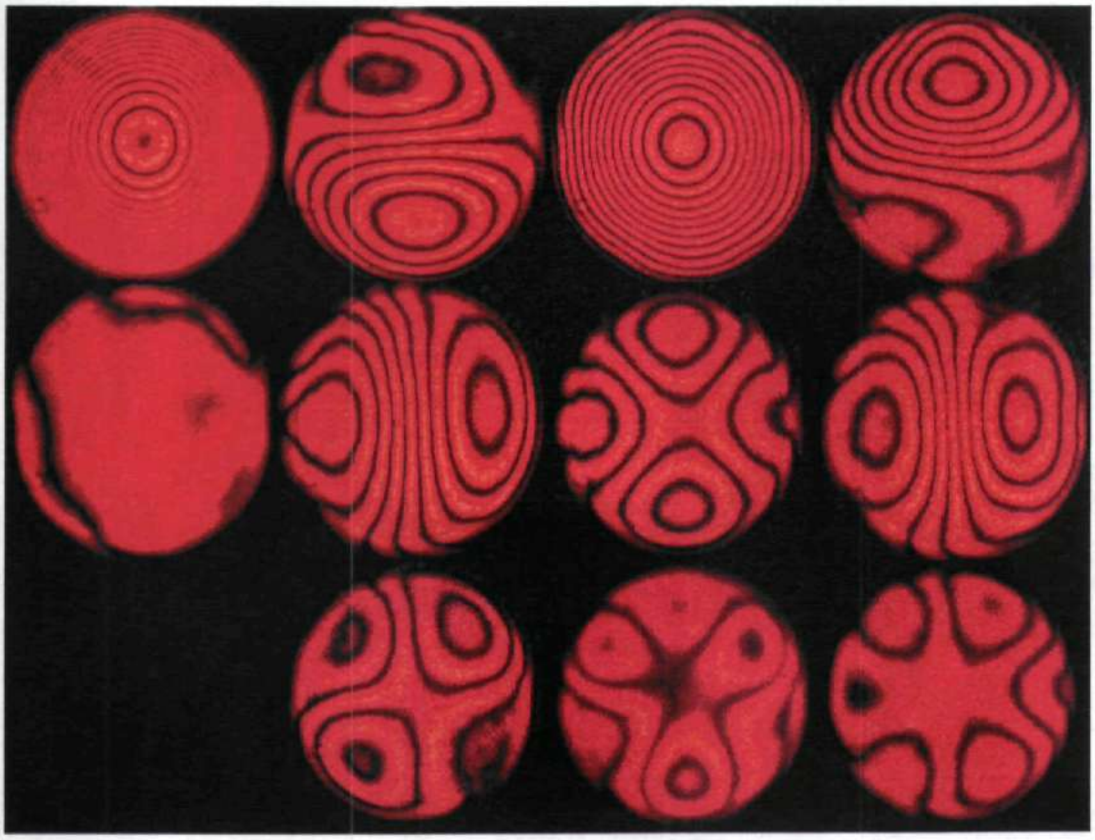

October, 2001

Université de Neuchâtel
Institut de Microtechnique

Applications of Optical Wavefront Modulation with Deformable Membrane Mirrors

Thèse

Présentée à la Faculté des sciences
pour obtenir le grade de docteur ès sciences
Par

Frédéric Gonté

Neuchâtel, octobre 2001

IMPRIMATUR POUR LA THESE

Applications of optical wavefront modulation with deformable membrane mirrors

de M. Frédéric Gonté

UNIVERSITE DE NEUCHATEL

FACULTE DES SCIENCES

La Faculté des sciences de l'Université de Neuchâtel sur le rapport des membres du jury,

MM. R. Dändliker (directeur de thèse), H.P. Herzig,
J.C. Dainty (Londres) et S. Fainman (La Jolla USA)

autorise l'impression de la présente thèse.

Neuchâtel, le 20 novembre 2001

Le doyen:

F. Zwahlen

Contents

Chapter 1

Introduction

> "*Light is always propagated in empty space with a definite velocity c which is independent of the state of motion of the emitting body*" A. Einstein (1879-1955)

The goal of this research was to determine new applications in the field of adaptive optics using newly developed low-cost wavefront correctors. The need of a low cost adaptive optics system compared to the systems proposed in astronomy (which costs several millions of US$) has been recognized at the beginning of the nineties. Several universities made important research efforts to develop such products. The T.U. Delft developed a wavefront corrector on the basis of optical micro-electro-mechanical systems. This corrector is a deformable membrane mirror. The membrane mirrors from T.U. Delft have the characteristics of a challenging new product. They can work at frequencies close to 1 kHz, have no hysteresis, allow several microns of deflection and have a continuous surface of up to five centimeters in diameter with hundreds of actuators. Our research concentrates on the use of deformable membrane mirrors with a diameter of 15 mm and 37 actuators.

During this research we diverged from the classical concept of adaptive optics, which is a close loop real time wavefront correcting system. Instead, we propose the direct optimization of coupling light sources into fibers without a wavefront sensor or to work in open loop condition where the deformable mirror is a phase addressing system to record multiplexed holograms in a photorefractive crystal. The wavefront sensor is then a calibration system to verify the orthogonality between the different phase distributions produced by the membrane mirror.

The basic principles of adaptive optics, which are necessary to understand this research, is described in chapter 2. A short historical view is given and some examples of wavefront correctors and sensors are explained. An introduction to the optical theory applied to this technology is given, in particular the use of the Zernike polynomials for the descriptions of the optical aberrations.

The chapter 3 is focused on the membrane mirror used during this research. We give the physical laws of deflection of the membrane and we show the use of a simulation of the behavior of the membrane under electrostatic load. We also determine the physical limitation of the membrane and the need for calibration for an optimal use.

The chapter 4 is devoted to the development of a Shack-Hartmann sensor used for the hologram recording application. We explain the optical concept of the sensor, its development and the algorithm used to compute the optical wavefront.

The chapter 5 describes the closed loop system developed for the optimization of the coupling of an abberrated coherent light source into a fiber. Different algorithms for the optimization have been elaborated and tested. Then, we present the prototype of a telecom fiber switch, where the membrane mirror is used to correct the aberrations produced by the switching lens. A bundle of monomode fibers is aligned in front of a moving lens and the membrane mirror. The light from one input fiber is collimated by the lens, back reflected by the mirror and coupled into one of the other fiber by displacing the lens laterally. The membrane mirror corrects the aberrations produced by the off-axis use of the lens. Finally we present the results obtained for the coupling of diode pump lasers into double clad doped fibers used for the amplification of signals. We demonstrate that the mirror is useful for the optimization of the fluorescence of the doped fiber and we developed a dynamic coupling system for space born fiber amplifiers. We give the limits of this system.

The chapter 6 describes an open-loop application. The demonstrator is a phase multiplexed holographic memory using the membrane mirror as a wavefront addressor. The signal to be recorded is produced by a liquid crystal display. We can record multiple holograms in a photorefractive crystal using different wavefronts produced by the membrane mirror for each hologram. The phase addressing is based on the Zernike modes produced by the membrane mirror. We will see that the Zernike mode multiplexing is limited by the capability of the membrane mirror to produce independent Zernike modes.

This thesis work is the result of a research undertaken at the Institute of Microtechnology in the context of an European project called MOSIS/ESPRIT[1]. The main problem of the adaptive optics technology remains its cost. This is the reason why MOSIS focused on the development and application of a low cost wavefront corrector where the cost per actuator is in the 50-100 $ range compared to the classical correctors which are in the 1,000-10,000 $ range.

Part of the research developed in the thesis has been presented at different Conferences

SPIE Annual Meeting San Diego, 2001.

Gonté F., Dändliker R., "Phase coding holographic memory using a deformable membrane mirror" Proc. SPIE 4493, 2001

Gonté F., Herzig H.P., Dändliker R., "Massive free-space optical 1XN fiber switch using an adaptive membrane mirror" Proc. SPIE 4493, 2001

Conference on adaptive optics for industry and medicine, Albuquerque 2001.

---

[1] MOSIS is the acronym for Micro-Optical SIlicon Systems. This project is included in the more general European project called ESPRIT (Europe'S PRogram for Information Technologies)

Gonté F., Dändliker R., "Phase coding holographic memory using a deformable membrane mirror".

Gonté F., Herzig H.P., Dändliker R., "Massive free-space optical 1XN fiber switch using an adaptive membrane mirror".

IEEE/LEOS Optical MEMS Okinawa, 2001.

Peter Y-A., Gonté F., Herzig H-P., "Micro-optical fiber switch for a large number of interconnects" Proc. IEEE/LEOS Int. Conf. Opt. Mems 2001, 2001.

IEEE/LEOS International Conference on Optical MEMS Hawaii, 2000.

Peter Y-A., Gonté F., Herzig H-P., "Optical fiber switch using a deformable mirror for a large number of interconnects" Proc. IEEE/LEOS Int. Conf. Opt. Mems 2000, 75-76, 2000.

Diffractive Optics and Micro-Optics, Quebec OSA Topical Meeting, 2000.

Nussbaum P., Gonté F., Boillat C., Herzig H-P., "Low NA fused silica refractive microlenses for Shack-Hartmann wavefront sensor" Proc. OSA Diffractive Optics and Micro-Optics, 247-249, 2000.

Conference on adaptive optics for industry and medicine, Durham 1999.

Gonté F., Courteville A., Rochat E. Haroud K., Collings N. Dändliker R., Vdovin G., Sakarya S., "High power laser diode to fiber coupling using a membrane mirror" Proc. Adaptive optics for industry and medicine, World Scientific, 346-351, 1999.

Chapter 2

Principle of adaptive optics

"Long telescopes may causes objects to appear brighter and larger than short ones can do, but they cannot be so formed as to take away that confusions of the rays which arises from the tremors of the atmosphere. The only remedy is a most serene and quiet air, such as may perhaps be found on the tops of the highest mountains above the grosser clouds." Isaac Newton (1642-1727).

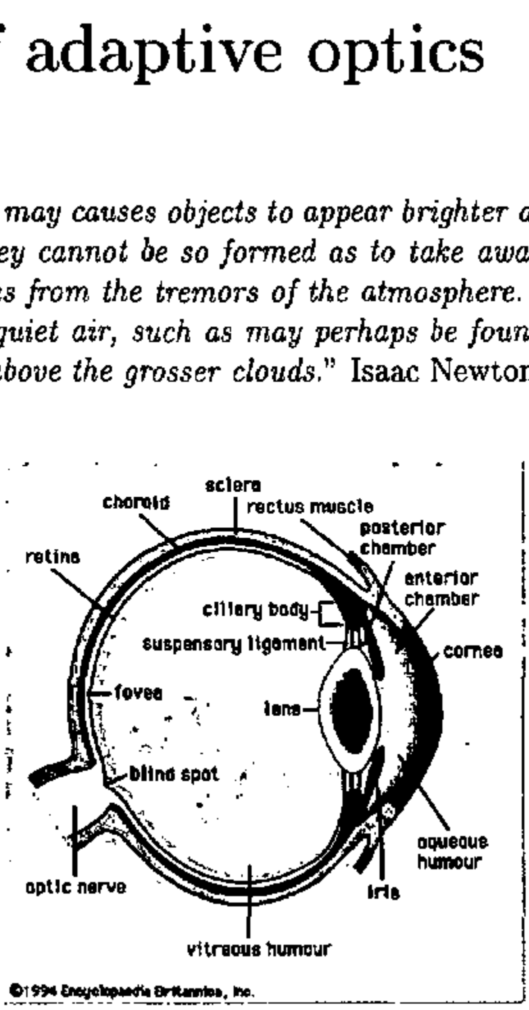

©1994 Encyclopaedia Britannica, Inc.

Figure 2.1: Cross-section of the human eye

The remedy has only been found during the XXth century, that is the adaptive optics technology. It is a technology which gives the capability to correct an optical wavefront distortion in real time[1]. Considering this definition the most obvious and widely used adaptive optics system is the eye (Fig. 2.1). The diameter of the pupil varies according

---

[1] By real time we understand that it reacts faster or at least as fast as the occurred change. For example in astronomy the frequency is around 1kHz.

to the intensity of the light by the action of the radial and circular muscles of the iris. Its diameter can change from 2 to 8 mm. The crystalline lens changes its shape to image any object on the retina, it is connected to the ciliary muscle by ligaments. The crystalline lens focus at infinity when the ciliary muscle are relaxed which flattens the lens. When the ciliary muscles are contracted the crystalline lens is released and under its own elastic force takes a more curved shape which reduce its focal length and allows to image an object at a closer distance. The eye is capable to bring the focus of an object from around 20 cm to infinity in less than a tenth of second, it can limit the intensity by a factor of sixteen and has two detecting systems for low and high intensity[2].

2.1 History of adaptive optics

Figure 2.2: Frontispiece to Friedrich Risner, Opticae Thesaurus, 1572.

According to the legend, the first adaptive optics system has been made by Archimedes in 213 B.C. with the soldier's shield of Syracuse. They have been used to reflect and focus the light on the sails of the Roman's ships, then burned the enemy fleet and delayed the capture of Syracuse. This action is represented in the Figure 2.2. Unfortunately Archimedes has been killed during the sacking of the city in 212 B.C. Adaptive optics has not been needed before the modern edge of optics. This edge starts in the second part of the sixteenth

---

[2] The rods and the cones, the rodes being high speed black and white low intensity photodetectors and the cones being low speed color and high intensity detectors.

century when Friedrich Risner translated Ibn al-Haytham's work[3] in "Opticae Thesaurus" in 1572 and when Giovan Battista de la Porta published "Magia Naturalis" in 1558 and "De Refractione" in 1593. These books give the basic laws of the working principles of several kinds of lenses, they produced a high interest on the scientific of this time and Johann Kepler published in 1604 "Ad Vitellionem paralipomena" where he proposed his laws of translation, reflection and refraction of light[4]. Galileo Galilei had the idea in 1609 to use the newly made Dutch "cylinders" to observe the moon, planets and stars. Due to the discoveries made by Galileo Galilei, the instrument has been named Galilean refractive telescope[5]. Sixty years later Isaac Newton proposed a reflective telescope to find a remedy to the chromatic aberrations observed with the refractive telescope. During its observations with it, Newton recognized a problem that he described and found no solution for it: the Seeing. The seeing is a loss of resolution due to the fluctuation of the refractive index of the atmosphere, it creates a blur around the stars on a picture. Due to this problem, the resolution of a large telescope can be less than the resolution for a 200 mm telescope. The need of a high level of technology to correct such problem prevented the development of a solution before the second part of the XX^{th} century.

2.1.1 First applications: astronomy and military

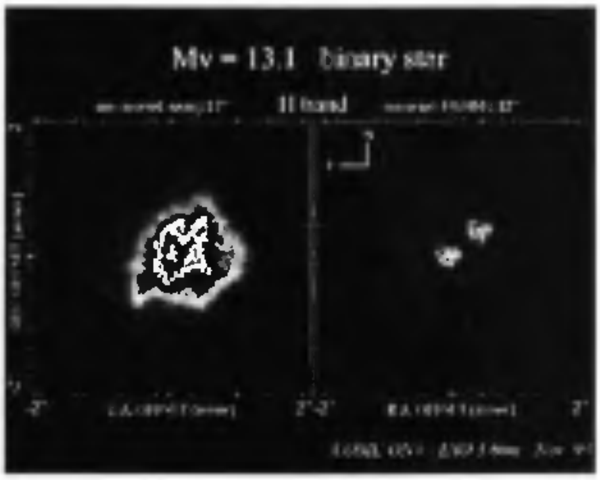

Figure 2.3: Experimental result obtained with COME-ON+

The first publication defining an optical deformable element driven to correct wavefront distortion has been written by Babcock [5] in 1953. It proposes the use of an Eidophor[6]

---

[3] It was written during the second part of the tenth century.

[4] Kepler also developed a telescope with 2 convergent lenses known as the Keplerian telescope in 1611[101], two years after the success obtained by Galileo.

[5] This is an instrument composed of a convergent and divergent lens.

[6] The Eidophor is textually described in [5] as following: "The Eidophor is essentially a thin layer of oil covering a reflecting mirror. A rastered electric charge is deposited on the surface of the oil film by

invented by F. Fischer [39] as a wavefront corrector. Independently Linnick wrote a paper in 1957 [49][7] about the same subject. The development cost of such systems was prohibitive, therefore nobody made an effort in that sense before the seventies. At that time the need for the U.S. air force to take images of satellites in orbit or to control laser beams through the atmosphere imposed the use of a controlled segmented mirror, which is nowadays a typical wavefront corrector. The first practical application in astronomy started to work in 1989, it was a system called COME-ON [80]. It has been used on the 1.52 m telescope of the Observatoire de Haute-Provence (France) and the ESO 3.6 m telescope at La Silla (Chile), it gave diffraction-limited image in the K band ($\lambda = 2.2\mu m$). The choice of an infrared band has been made because it is easier to obtain a diffraction limited image at this wavelength. This system has been updated under tbe name "COME-ON+" and since has been regularly used, an example of its result is given in Figure 2.3, which shows the detection of a binary star from a blurred picture in the H band ($\lambda = 1.68\mu m$). The last evolution which is actually used since 1996 and called "ADONIS" is well explained in [78]. The U.S. military research related to adaptive optics has only been declassified in 1990. The release of science and engineering knowledge from the military side and the demonstration made with COME-ON gave a boost to the research in adaptive optics. Another domain has a strong need of the adaptive optics technology, it is the nuclear fusion using high power laser. The quality of the laser beams is controlled with the help of adaptive optics systems. Such systems are already installed at the Lawrence Livermore National Laboratory.

2.1.2 Evolution and future

Today, every newly developed telescope (Very Large Telescope, Gemini, Keck) is equipped with an active and adaptive optics system. The active optics system[8] corrects the aberrations on the primary mirror, which is a plain or segmented mirror of up to 10 meters of diameter corrected by hundreds of actuators. It corrects the aberrations introduced by the gravity, its angle of inclination and the structural changes due to the temperature. The adaptive optics set-up to correct the atmospheric fluctuations is at the focus of the telescope and works in the 1 kHz range. These systems need a turbulence probe, which can be a bright star or a laser guide star (LGS), which creates an artificial star with its light backscattered in the upper layer of the atmosphere[9]. Thanks to this technology we already imagine space telescopes of 6 m diameters (NGST[10]) and ground telescopes of 100 m

---

conventional cathode-ray techniques, and through electrostatic forces the oil film is distorted according to the desired pattern."

[7] Written in Russian.

[8] This is an adaptive optics system working at low frequency (less than 10 Hz).

[9] They are two types of LGS, the first is a Rayleigh beacon, which backscatter off air molecules in the range of 10-20 km, the second uses the resonant excitation of atoms in the mesospheric sodium layer at an altitude of 90 km [77].

[10] The New Generation Space Telescope will be a deployable mirror of 8 segments with an aperture of 6.5 m [52]. The natural deformation of the segments will be corrected by an adaptive optics system.

(OWL[11]). In France, an inertial confinement fusion called "Laser Megajoule" is being built and will work at the end of this decade.

Besides these developments, research in low cost adaptive optics started at the beginning of the nineties. For this purpose new wavefront correctors and sensors made of micro-electro-mechanical elements have been developed. They are applied in medicine, industrial and new scientific domains, such as eye study, laser welding, free space communication or confocal microscopy. The silicon made membrane mirror, which was used for this thesis, is a key component of this evolution.

2.2 Theory and technology of adaptive optics

The adaptive optics domain is at the boundary of different physical and technological concepts, the four components being optics, mechanics, electronics and computing, that is the reason why this technology took so long to develop. The principle of an adaptive optics system is to measure and correct an optical wavefront. It is a closed-loop system. The wavefront sensor measures the path difference between the disturbed wavefront and the ideal one, and the wavefront corrector makes the correction. We will not give in this section information about air turbulence, Kolmogorov law etc., since our work focuses on systems which are not involved in retrieving informations which has crossed different layers of the atmosphere.

2.2.1 A control loop system

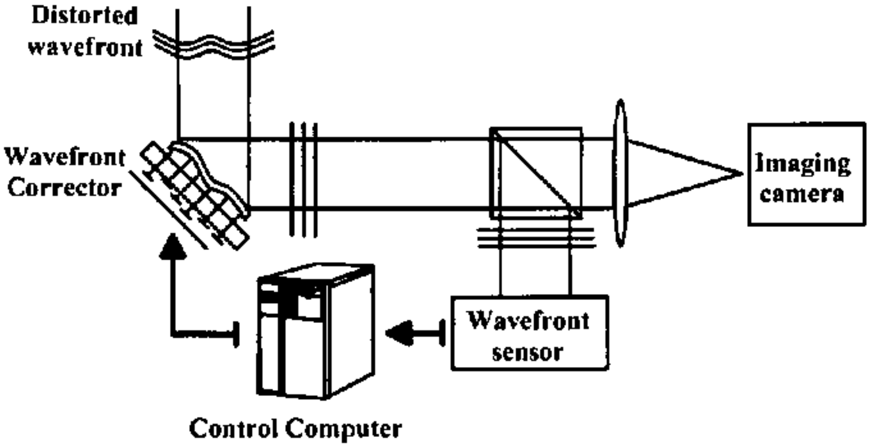

Figure 2.4: Basic adaptive optics imaging system

---

[11] The Over Whelmingly Large telescope is a project of the European Southern Observatory (ESO)[36][26].

An adaptive optics system is before all a multi-variable closed-loop control system. Multi-variable because of the number of mirror actuators acting on the system and closed-loop because of the residual error correction of the wavefront made by the mirror after sensing the corrected wavefront. Figure 2.4 shows the scheme of the system. An adaptive optics system is composed of:

A wavefront corrector which is the most often a deformable mirror.

A wavefront sensor which is nowadays mainly a Shack-Hartmann sensor composed of a matrix of microlenses and a 2-D array of detectors like photodiodes or CCD.

A scientific instrument such as a spectrometer or an imaging camera.

A command control composed of a frame grabber if the wavefront sensor contains a CCD camera or a multiple analog to digital channel receiver, if the wavefront sensor contains a matrix of photon counting detector.

A wavefront shape calculator.

A multi-channel digital to analog converter and a high voltage amplifier to send the calculated position to the actuators of the wavefront corrector.

2.2.1.1 The Adaptive optics servo-loop

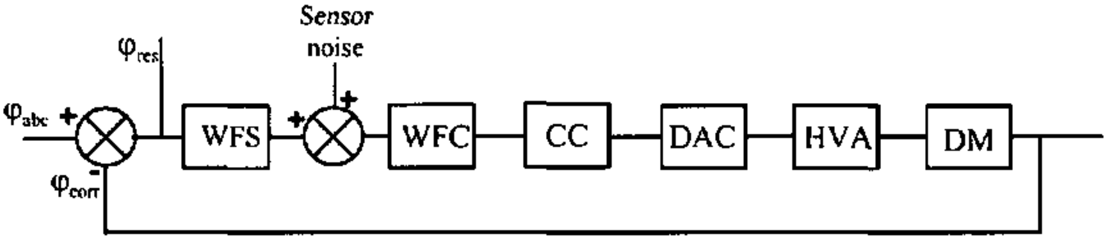

Figure 2.5: Block-diagram of a typical adaptive optics system

Several authors [19] [53] [94] gave full descriptions of the adaptive optics servo-loop system; we will give here only a short summary. The block diagram of an adaptive optics system is shown in Figure 2.5, where WFS is the wavefront sensor, CC is the computer control, DAC is the digital to analog converter, HVA is the high voltage amplifier and DM is the deformable mirror. From the block diagram we can define the transfer function of the adaptive optics system.

The wavefront sensor, whose main part is the photonic detector integrating the optical flux during a time T_{wfs}, averages also during the same time the incoming wavefront. By calling the wavefront perturbation $\varphi(t)$ and the output of the wavefront sensor $M(kT_{wfs})$, which is the kth sample of the continuous function of $M(t)$, this function can be written

$$M(t) = \frac{1}{T_{wfs}} \int_{t-T_{wfs}}^{t} \varphi(t)\, dt = \frac{1}{T_{wfs}} \int_{t-T_{wfs}}^{\infty} \varphi(t)\, dt - \frac{1}{T_{wfs}} \int_{t}^{\infty} \varphi(t)\, dt \qquad (2.1)$$

This demonstrates that the temporal behavior of the detector is the difference of the infinite integral of $\varphi(t)$ and of the same integral with a time lag of T_{wfs}. Taking the Laplace transform, we find that its transfer function is given by

$$WFS(s) = \frac{1 - \mathrm{e}^{-T_{wfs}s}}{T_{wfs}s}. \tag{2.2}$$

The wavefront computer has a time delay τ during which it makes the computation of the wavefront measurement. The corresponding transfer function is

$$WFC(s) = \mathrm{e}^{-\tau s}. \tag{2.3}$$

The main task of the control computer is to calculate the deformable mirror control voltages and to implement the real time compensation to optimize the closed loop. This transfer function is given by [19]

$$CC(s) = \frac{K}{s}, \tag{2.4}$$

where K is the gain.

The digital to analog converter keeps its values during a time T_{dac}, which yields the transfer function

$$DAC(s) = \frac{1 - \mathrm{e}^{-T_{dac}s}}{T_{dac}s}. \tag{2.5}$$

The transfer functions for the deformable mirror and the high voltage amplifier are assumed to be equal to 1, because their temporal response is largely above the working frequency of the system.

2.2.1.2 Optical wavefront sensors

Different technologies are possible to detect and measure optical wavefronts. This can be made by measuring the shift of interference fringes or the shift of a focal spot, produced by a change of the optical path difference, or by the measurement of the irradiance. Table 2.1 represents a non exhaustive list of these techniques, classified by different approaches. The three main systems used up to now are the lateral shear interferometer, the Shack-Hartmann sensor and the curvature sensor.

The lateral shear interferometer [31]: This is the technology which has been the most widely used until the beginning of the nineties. The wavefront is incident on a parallel plate which reflects the wavefront on its first surface and a shifted wavefront on the second surface. Theses two wavefronts are combined to form in their overlap area an interference

Technical approach	Systems
direct OPD wavefront measurement	Radial shear interferometry Point diffraction interferometry
indirect OPD wavefront measurement	Lateral shear interferometry Knife edge Shack-Hartmann
Irradiance based wavefront sensing	Curvature sensor Axial intensity Phase retrieval

Table 2.1: Wavefront sensor list

pattern. This pattern provides the information on the optical path difference compared to the perfect wavefront. Two sheared interferograms at orthogonal directions are required to reconstruct the wavefront.

The curvature sensor: This system, imagined and developed by Roddier in 1988 [76], makes a wavefront curvature measurement instead of the wavefront slope measurement as done by the shear interferometer and the Shack-Hartmann sensor. The wavefront is transmitted through a telescope and is imaged at the focal distance of the telescope. The local wavefront curvature is detected by measuring the irradiance distribution of the beam at a short distance before and after the focus. This curvature creates a lack or an exess of illumination on the two irradiance distributions. This technique provides the measurement of the Laplacian of the wavefront with its radial tilts and aperture edge. It has the advantage when used with a membrane or a bimorph mirror, to be directly related to the deformation.

The Shack-Hartmann sensor: The Shack-Hartmann sensor is the most widely used wavefront sensor nowadays. Because we developed one for this thesis work, it will be fully explained in the chapter 4.

2.2.1.3 Correctors

An optical wavefront can be corrected by transmission or by reflection, but the most classical wave corrector is a deformable mirror. The surface of the mirror can be continuous as shown in Fig. 2.6(a) or segmented as shown in Fig. 2.6(b). In the case of the segmented mirror, one or several actuators are disposed under the segments to produce the tip and tilt of the segments. Most of the actuators are piezoelectric ceramics. An other kind of deformable mirrors having a plane surface is the bimorph mirror. It is composed of a sandwich made of a sheet of reflecting surface (glass, metal), an electrode, a sheet of piezoelectric ceramic and an array of back electrodes conveniently disposed. The voltages applied to the electrode produce a local change in the thickness of the piezoelectric ceramic, which change the shape of the reflecting surface.

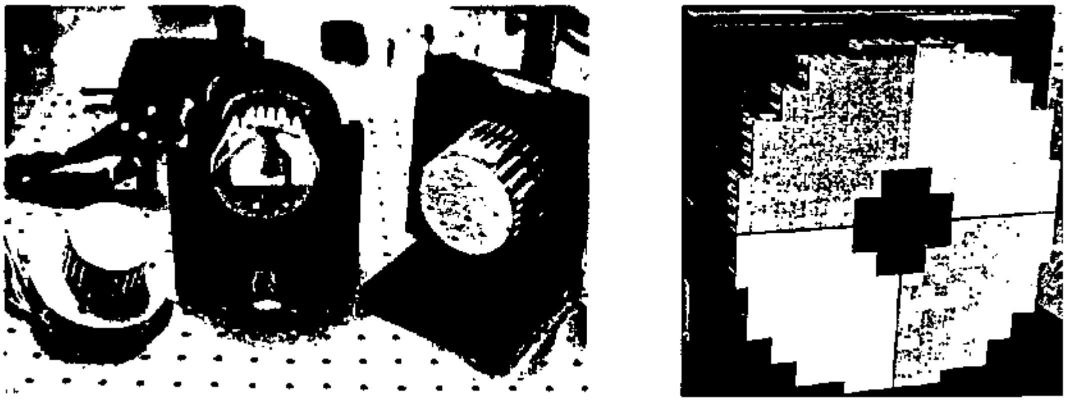

Figure 2.6: Deformable mirror with piezo actuators: (a) continuous surface (b) segmented mirror from the Thermotrex company.

The correction of wavefronts by transmission is possible with liquid crystal devices, as explained by Love [50]. With the help of a nematic liquid crystal spatial light modulator composed of 69 hexagonal pixels, he has been able to correct a wave front up to the 15th Zernike mode.

The corrector technology used during this work is a new technology, called optical micro-electro-mechanical systems (optical MEMS). This technology started to be developed at the beginning of the nineties. Our corrector is a silicon nitride membrane with a thickness of less than one micron and coated with a highly reflective material. We give a full description of this deformable membrane mirror and its properties in Chapter 3.

2.2.2 Interpretation of optical aberrations

The best way to describe the phenomena in an adaptive optics system is by the use of the wave theory of optics. This theory has been definitively settled by Fresnel at the beginning of the XIX^{th} century. In the context of adaptive optics, we have to take account of the propagation of light with aberrated wavefronts, described by the diffraction theory of aberrations. This theory has been first investigated by Rayleigh, inspired by tbe work of Huygens, Fraunhofer and Fresnel.

2.2.2.1 Propagation of aberrated wavefronts

An accurate analysis of the diffraction theory of aberrations is given in [9], we will give here only the part of this theory needed for our application. As shown in Fig. 2.7 we consider a centered optical system with a point source of monochromatic light at P0. P1 is the image of point P0.

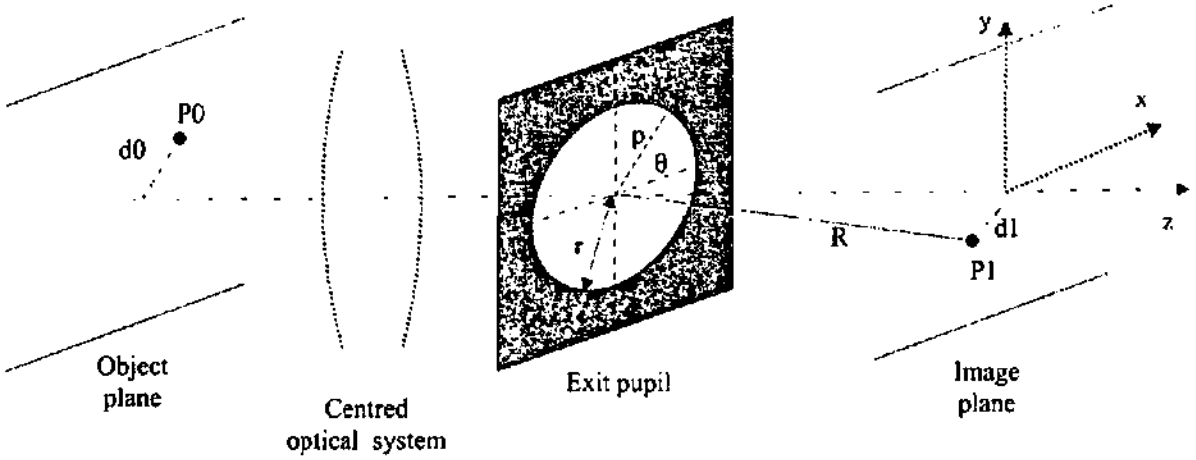

Figure 2.7: Coordinate and notation system for the diffraction calculation

The disturbance $U(P)$ from a reference sphere at an arbitrary point P in the image plane is given by the Huygens-Fresnel principle as

$$U(P) = -\frac{i}{\lambda}\frac{Ae^{-ikR}}{R}\int\int \frac{e^{ik[\Phi+s]}}{s}dS. \tag{2.6}$$

A/R is the amplitude at the exit pupil, R is the distance between the center of the exit pupil and the point P1, s is the distance between a point at the pupil and an arbitrary point in the region of the image. Φ is the aberration function of the wavefront at the exit pupil. Using normalized polar coordinates (ρ, θ) for pupil, dS is given by $dS = r^2\rho d\rho d\theta$ with r being the radius of the pupil. The coordinates in the image are x,y,z with z being normal to the pupil plane. Based in polar coordinates in the image plane with $\varphi = \arctan(y/x)$, the following reduced coordinates for P are introduced:

$$u = \frac{2\pi}{\lambda}\left(\frac{r}{R}\right)^2 z \tag{2.7}$$

and

$$v = \frac{2\pi}{\lambda}\left(\frac{r}{R}\right)\sqrt{x^2+y^2}. \tag{2.8}$$

Finally, in the image plane region we can replace s by R, hence Eq. (2.6) becomes

$$U(u,v,\varphi) = -\frac{i}{\lambda}\frac{Ar^2}{R^2}e^{iu\left(\frac{R}{r}\right)^2}\int_0^1\int_0^{2\pi} e^{i\left[k\Phi - v\rho\cos(\theta-\varphi) - \frac{1}{2}u\rho^2\right]}\rho d\rho d\theta, \tag{2.9}$$

and then the intensity at P is given by

$$I(u,v,\varphi) = \left(\frac{Ar^2}{\lambda R^2}\right)^2 \left|\int_0^1\int_0^{2\pi} e^{i\left[k\Phi - v\rho\cos(\theta-\varphi) - \frac{1}{2}u\rho^2\right]}\rho d\rho d\theta\right|^2. \tag{2.10}$$

We can introduce now an important parameter used in adaptive optics to define the quality of the correction: the Strehl ratio, also called normalized intensity. It is given by the ratio of the peak intensity of the point spread function (PSF) under perfect condition (diffraction limited) and under aberrated condition. Without aberration the peak intensity is (at $u = v = \varphi = 0$)

$$I_{\Phi=0} = \pi^2 \left(\frac{Ar^2}{\lambda R^2} \right)^2 . \tag{2.11}$$

Then the Strehl ratio, which is the ratio of the maximal intensity for the aberrated wavefront and the perfect wavefront, is given by

$$S_R = max \left\{ \frac{1}{\pi^2} \left| \int_0^1 \int_0^{2\pi} e^{i\left[k\Phi - v\rho\cos(\theta-\varphi) - \frac{1}{2}u\rho^2\right]} \rho d\rho d\theta \right|^2 \right\} . \tag{2.12}$$

When the overall aberrations are small, it can be shown that the intensity maximum is nearly on the axis ($u = v = \varphi = 0$) and the Strehl ratio is reduced to

$$S_R = \frac{1}{\pi^2} \left| \int_0^1 \int_0^{2\pi} e^{ik\Phi_P} \rho d\rho d\theta \right|^2 , \tag{2.13}$$

where Φ_P is the aberration function centered at the point P.

Gaussian optics is an approximation of the property of an optical system, called paraxial optics or first order optics, which neglects the aberrations. The investigation of aberrations started only at the middle of the XIXth century by Petzval and Seidel. Seidel took account of the third order theory of an optical system and then determined 5 aberrations, also called Seidel aberrations, which are spherical aberration, coma, astigmatism, field curvature and the distortion.

The best way to describe the aberration function is by a power series. In our context, where we have an integration over a unit circle (a plain circular membrane), it is best to use a complete set of polynomials.

2.2.2.2 Orthogonal modes and Zernike modes

In the paper written in 1934 [113], Zernike developed a complete set of orthogonal polynomials[12] over the interior of a unit circle to describe wave aberrations. Descriptions how to use these Zernike polynomials are given by Born & Wolf [9], Malacara [57], Noll [67], and Roddier [77].

---

[12] For an extensive knowledge of the mathematical properties of the polynomials see [12].

The characteristics of the Zernike polynomials are: they are orthogonal over a unit circle, they are complete in the sense that any wavefront can be described by a linear combination of Zernike polynomials, and they are invariant to rotation around the center of the circle.

For a circular aperture without obstruction[13] and using polar coordinates, the Zernike modes are defined by

$$Z_n^m = R_n^m(\rho)\, e^{im\theta}, \tag{2.14}$$

where θ and ρ are the polar coordinates.

Orthogonality and normalization are given by

$$\int_0^1 \int_0^{2\pi} Z_n^m Z_{n'}^{m'*} \rho d\rho d\theta = \frac{\pi}{n+1}\delta_{nn'}\delta_{mm'}, \tag{2.15}$$

where δ_{ij} is the Kronecker symbol and the asterisk is for the complex conjugate. As explained in [9], the radial polynomials $R_n^m(\rho)$ can be derived from the Jacobi polynomials [12] and are finally found to be

$$R_n^m(\rho) = \sum_{s=0}^{(n-m)/2} \left(\frac{(-1)^s (n-s)!}{s!\left(\frac{(n+m)}{2}-s\right)!\left(\frac{(n-m)}{2}-s\right)!} \right) \rho^{(n-2s)}. \tag{2.16}$$

Table 2.2 shows the radial polynomials $R_n^m(\rho)$ as calculated by Zernike in 1934.

m\n	0	1	2	3	4	5	6
0	1		$2\rho^2-1$		$6\rho^4-6\rho^2$ $+1$		$20\rho^6-30\rho^4$ $+12\rho^2-1$
1		ρ		$3\rho^3-2\rho$		$10\rho^5-12\rho^3$ $+3\rho$	
2			ρ^2		$4\rho^4-3\rho^2$		$15\rho^6-20\rho^4$ $+6\rho^2$
3				ρ^3		$5\rho^5-4\rho^3$	
4					ρ^4		$6\rho^6-5\rho^4$
5						ρ^5	
6							ρ^6

Table 2.2: Radial polynomials

From this table, several classifications of the Zernike polynomials have been made. The best known are the ones from Kim and Shannon in [41], Noll [67] and Malacara [57]. In

---

[13] The specific case of annular pupils has been extensively studied by Mahajan in [54].

the paper of Kim and Shannon a 3D representation of the 37 first Zernike modes is shown. The Table 2.3 presents the difference of these classifications.

In the present thesis, we will only use the classification given by Noll. The modes up to the 5th order are presented in Appendix A.

Noll	Malacara	Shannon	m	n	Zernike polynomials	definitions
1	1	1	0	0	1	piston
2	3	2	1	1	$2\rho\cos\theta$	Tip
3	2	3	1	1	$2\rho\sin\theta$	Tilt
4	5	4	0	2	$\sqrt{3}\,(2\rho^2-1)$	Defocus
5	6	5	2	2	$\sqrt{6}\rho^2\sin 2\theta$	Astigmatism(3rd order)
6	4	6	2	2	$\sqrt{6}\rho^2\cos 2\theta$	Astigmatism(3rd order)
7	9	7	1	3	$\sqrt{8}\,(3\rho^3-2\rho)\sin\theta$	Coma
8	8	8	1	3	$\sqrt{8}\,(3\rho^3-2\rho)\cos\theta$	Coma
9	10	10	3	3	$\sqrt{8}\rho^3\sin 3\theta$	Trefoil
10	7	11	3	3	$\sqrt{8}\rho^3\cos 3\theta$	Trefoil
11	13	9	0	4	$\sqrt{5}\,(6\rho^4-\rho^2+1)$	Spherical
12	14	12	2	4	$\sqrt{10}\,(10\rho^4-3\rho^2)\cos 2\theta$	Astigmatism(5th order)
13	12	13	2	4	$\sqrt{10}\,(10\rho^4-3\rho^2)\sin 2\theta$	Astigmatism(5th order)
14	15	17	4	4	$\sqrt{10}\rho^4\cos 4\theta$	Ashtray
15	11	18	4	4	$\sqrt{10}\rho^4\sin 4\theta$	Ashtray
16	19	14	1	5	$\sqrt{12}\,(10\rho^5-12\rho^3+3\rho)\cos\theta$	
17	18	15	1	5	$\sqrt{12}\,(10\rho^5-12\rho^3+3\rho)\sin\theta$	
18	20	19	3	5	$\sqrt{12}\,(5\rho^5-4\rho^3)\cos 3\theta$	
19	17	20	3	5	$\sqrt{12}\,(5\rho^5-4\rho^3)\sin 3\theta$	
20	21	26	5	5	$\sqrt{12}\rho^5\cos 5\theta$	
21	16	27	5	5	$\sqrt{12}\rho^5\sin 5\theta$	

Table 2.3: Different classifications of the Zernike polynomials.

2.3 Summary

In this chapter we gave a short overview of the history of adaptive optics; we have seen that the development of this technology took a long time due to the scientific and technological limits encountered. We also briefly described the concept of adaptive optics systems, which is a closed-loop system using a wavefront corrector and wavefront sensor to correct dynamic optical aberrations. We did not take account of air turbulence in the description, because the experiments made in this work are not based on the transmission of wavefronts through atmospheric layers. We gave a short description of the concepts of aberrations. Finally, we introduced the Zernike polynomials. We have seen that the Zernike Polynomials were ideal by their specific properties to describe the aberrations.

Chapter 3

The membrane mirrors

> "*The reason why the light reflects from a mirror at the same angle as the incident light is the following. As the light moves very quickly, when it falls on the mirror it does not penetrate the interior but it can not stop and as the force and the natural primitive movement still remains in it, it reflects off the side it cames from and follows the same inclination as the precedent.*" IBn-al-Haytham (965-1039)

The research on membrane mirrors started in the second part of the seventies [29]. The membrane mirror prototype produced by the Perkin-Elmer corporation was made of titanium, nickel, beryllium or even molybdenum by evaporation on a substrate. The membrane was positioned and tensioned between a transparent biased electrode and an electrode array. The membrane assembly was confined in a 270 Pa vacuum needed for the damping requirement of the assembly. In 1981 a membrane mirror made of polypropylene and coated with aluminum has been specifically designed for astronomical applications [61]. It was used in combination with a speckle interferometer. But it is only with the development of the Micro-Electro-Mechanical (MEM) technologies in the nineties that the fabrication of low cost membrane mirrors has been possible [97][6]. As for the standard adaptive mirrors they can be made of a continuous or segmented mirror. We have used membrane mirrors produced by the Technological University of Delft. They are continuous membrane mirrors of different size and have different coatings.

3.1 Fabrication technology of the mirror

The team led by Gleb Vdovin at T.U. Delft started to developed membrane mirrors a few years ago. Their first mirrors were rectangular with a surface of 1 cm^2, now they are able to produce membrane mirrors with a diameter of up to 5 cm and specifically designed for the astronomy. During this work, we used circular membrane mirrors with a diameter of

15 mm. Figure 3.1 shows a photograph of the membrane mounted on the chip and the interference pattern obtained from the mirror surface.

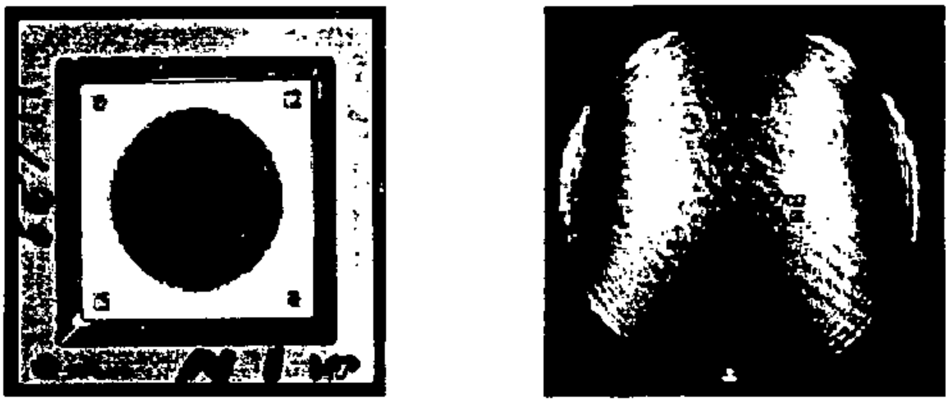

Figure 3.1: Membrane mirror: (a) photo, (b) interference pattern

The membrane mirrors are made of silicon nitride supported by a silicon chip and sustained by a PCB holder. The electrode structure, spacer and connectors are deposited on the PCB holder. An extensive description of the fabrication process is given in [97], [99] and [98]; it is summarized in the following.

Constant	Symbol	value
Young's modulus	E	$3.1e^{11}$ N/m^2
Density	ρ	3.18 g/cm^3
Poisson's ratio	σ	0.23

Table 3.1: Physical characteristics of the silicon nitride

The membrane mirror is made of silicon nitride of 0.5 μm thickness and is fabricated using KOH anisotropic etching of (100) silicon wafers. The principal physical characteristics at room temperature of the silicon-nitride are given in the Table 3.1. The membrane is then coated with different layers of metal to obtain the desired reflectivity. Aluminum can be directly deposited on silicon-nitride. The scattering from the membrane is less than 2% and is produced by the coating defects and dust on the membrane. The total reflection is between 85% and 90% for visible light. For a mirror of higher reflectivity, it is necessary to coat first the membrane with a 10 nm thick layer of chrome to improve the adhesion of the next coating, then to deposit a 100 nm thick layer of silver, and to finish with several layers of dielectric materials with a thickness specific to the laser wavelength to be reflected. A reflectivity of more than 99.9 % has been obtained. We can see in Figure 3.2 a typical coating of the membrane. The presented coating is for maximum reflection at 800 nm.

Figure 3.3 shows the cross section of the deformable membrane mirror and the hexagonal array of the 37 electrodes under the membrane, which has a diameter of 15 mm. The

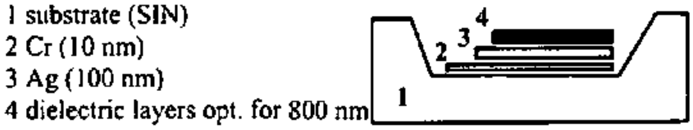

Figure 3.2: Typical mirror coating for high reflection at 800 nm

distance between the centers of the electrodes is 1.75 mm. The diameter of the hexagonal structure of the electrodes is 12 mm. Thus, the useful diameter of the membrane mirror is considered to be less than12 mm.

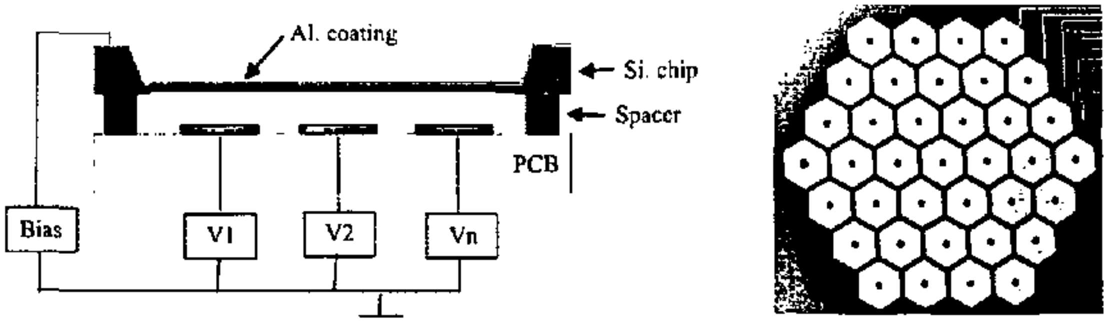

(a) (b)

Figure 3.3: Membrane mirror: (a) schematic cross-section, (b) photograph of the electrode array.

3.2 The physics of a membrane mirror

We consider the membrane as an element having a thickness very small compared to its width and length. Moreover, its deflection is very large compared to its thickness. In this case, the resistance of the element to bending is neglected [90]. The deflection of the membrane is due to the electrostatic attraction produced by the electrodes. Each electrode has a specific position to be taken into account for the overall deflection of the membrane. The behavior of the membrane has been extensively studied by Morse [64] in a general case. The equation of motion of a circular membrane without external force and viscous damping in polar coordinate is

$$\nabla^2 \eta \left(r, \varphi, t\right) = \frac{\rho}{T} \frac{\partial^2 \eta \left(r, \varphi, t\right)}{\partial t^2}, \tag{3.1}$$

where η is the the displacement of the membrane from its equilibrium position, ρ the mass density,

$$T = \frac{Eh\delta^2}{2(1-\sigma)}, \tag{3.2}$$

is the stress of the membrane with the Young's modulus E, the Poisson's ratio σ, the strain δ of the membrane due to stretching, and the membrane thickness h. For a typical thickness of $h = 0.5\ \mu$m, a strain of $\delta = 9.2 \cdot 10^{-3}$, and the values given in Table 3.1 for the Young's modulus and the Poisson's ratio, we obtain a stress of $T = 11.9$ N/m^2.

In the case of an additional external force $F\left(r, \varphi, t\right)$, the Eq. (3.1) becomes [29]

$$\frac{\partial^2 \eta\left(r, \varphi, t\right)}{\partial t^2} = \frac{T}{\rho} \nabla^2 \eta\left(r, \varphi, t\right) + \frac{F\left(r, \varphi, t\right)}{\rho}. \tag{3.3}$$

The static equation for the membrane mirror is then

$$\nabla^2 \eta\left(r, \varphi\right) = \frac{F\left(r, \varphi\right)}{T}. \tag{3.4}$$

In our case, the circular membrane is deflected by electrostatic attraction. the force from one electrode is then given by [77]

$$F = \frac{\epsilon_0 \pi s^2}{2} \left[\frac{V_0 + V_s}{d}\right]^2, \tag{3.5}$$

where V_s is the operating voltage and V_0 a bias voltage, s is the electrode pad radius, d is the distance between the electrode and the membrane and $\epsilon_0 = 8.85 \cdot 10^{-12}$ F/m is the absolute dielectric constant .

Following [65] and [64], the steady state deflection at a position r on the membrane produced by an electrostatic attraction acting at the center of the membrane is

$$\eta = \begin{cases} \frac{F}{2\pi T}\left[\ln\frac{R}{s} + \frac{1}{2s^2}\left(s^2 - r^2\right)\right] & 0 \leq r < s \\ \frac{F}{2\pi T}\ln\frac{R}{r} & s < r \leq R \end{cases} \tag{3.6}$$

R is the radius of the membrane as shown in Fig. 3.4.

At the center of the membrane mirror ($r = 0$), and implementing Eq. (3.5) in Eq. (3.6) we find

$$\eta = \frac{\epsilon_0 s^2 \left[V_0 + V_s\right]^2}{4Td^2} \left(\ln\frac{R}{s} + \frac{1}{2}\right). \tag{3.7}$$

With a voltage of $V_0 + V_s = 200$ V, an electrode radius of $s = 6$ mm, which is equivalent to the array radius of the 37 electrodes, a distance $d = 100\ \mu$m and a stress of $T = 11.9$ N/m^2, we obtain a deflection of $\eta = 9.5\ \mu$m.

The natural fundamental frequency f_{res} of the membrane mirror is given by [89]

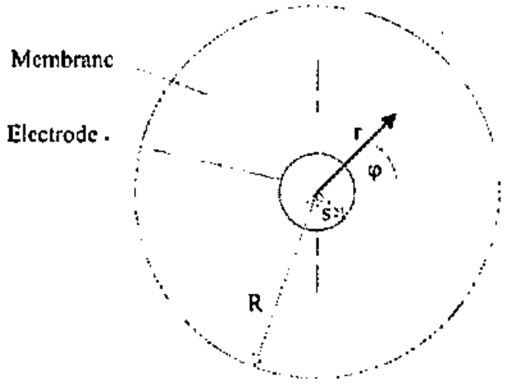

Figure 3.4: Diagram for the coordinate of the membrane with a central electrode.

$$f_{res} = \frac{10.21h}{2\pi R^2}\sqrt{\frac{E}{12\rho\left(1-\sigma^2\right)}}. \tag{3.8}$$

With values for E and σ given in Table 3.1 and the radius $R = 7.5$ mm of the mirror membrane, we obtain a fundamental resonance frequency of $f_{res} = 1340$ Hz.

3.3 Simulation

We used a computer simulation program to calculate the behavior of the membrane mirror for different distributions of the electrode voltages. We will see that the structure and the number of the electrodes to activate the membrane produce a typical set of mirror deflections, which we will call the membrane mirror modes. They can be directly used for some applications.

A program simulating the deformation of the membrane has been developed at the Imperial College of London, [70] and [71], on the basis of a finite element model of the membrane deflection with the linear approximation that the deflection is small compared to the distance between the membrane and the electrodes. It allows the simulation of the membrane deformation according to the electrode voltages and to obtain the Zernike polynomials corresponding to this deflection. The simplified Eq. (3.4) becomes then

$$\nabla^2\eta\left(r,\varphi\right) = \frac{F\left(r,\varphi\right)}{T} = -\epsilon_0\frac{V^2\left(r,\varphi\right)}{Td^2}. \tag{3.9}$$

The finite element model which has been implemented with the help of the package DIFF-PACK on C++, gives the mirror influence functions. The deformation of the membrane mirror, expressed as a vector of Zernike coefficients $\mathbf{\Phi}$, is then given by

$$\mathbf{\Phi} = \mathbf{Ae}, \tag{3.10}$$

where **A** is the influence matrix of the mirror and $\mathbf{e} \propto V^2$ is a vector representing the actuator pressures of the 37 electrodes. For our purpose, the influence matrix **A** delivered by the Imperial College has been defined as 500×37 elements and transform the actuators pressure as a 500 term Zernike expansion describing the deformation of the membrane mirror. This matrix has been exploited on MATLAB to obtain the simulated deformation of the membranes mirror. The vector of electrode voltage to the square for a particular deformation described by a vector of Zernike coefficient is given by

$$\mathbf{e} = \mathbf{A}^{-1}\Phi, \tag{3.11}$$

where $\mathbf{A}^{-1}$ is the pseudo inverse of **A**. The Eq. (3.11) represents the least square fit to determine the specific electrode set for a particular set of Zernike mode. This is applied on the overall membrane of the mirror. As the membrane is held at its rim by the Silicon chip, we understand that we can not perfectly fit the Zernike modes. To obtain them we decided to work with the central part of 12 mm of diameter of the membrane mirror. We calculated the new influence matrix by calculating the Zernike coefficients of the deformation of the central part of each electrode deflection. This new influence matrix is called **B** and has 200×37 elements, therefore the specific set of electrode for each wanted Zernike mode is given by $\mathbf{e} = \mathbf{B}^{-1}\Phi$.

The simulated Zernike deformations for each mode up to the 4^{th} mode are given in Appendix B. Figure 3.5 shows the interference pattern of the 10 first Zernike modes but the piston. We corrected most of the initial aberrations which was on the bias to well observe the modes. Then the first picture is the unbiased mirror and the second is the biased mirror, the other photograph are the modes two to ten with their maximum deflection capability.

An important work has been done by Zhu et al [114] and it has shown that the mirror considered above is not able to create the Zernike modes above the 5^{th} order (see Tab. 2.3).

3.4 Characteristics

3.4.1 Deflection

The deflection has been measured for different mirrors with the help of a Michelson interferometer. This interferometer has a reference mirror of 2 meters focal length, which corresponds more or less[1] to the bias deflection of the membrane mirrors. Compared to this reference an average of 12 interferences lines at 633 nm have been measured at maximum deflection in the central part of the membrane mirror (diameter 12 mm), which represents

---

[1] It is slightly different for each mirror.

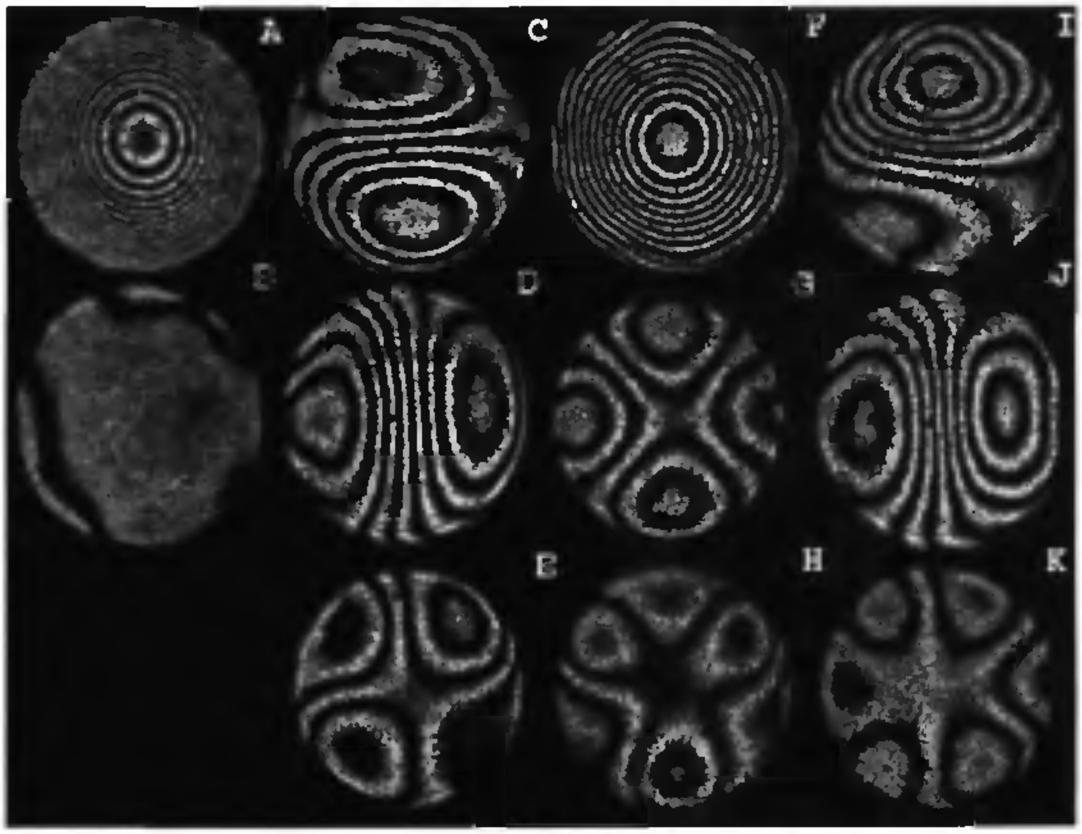

Figure 3.5: interference pattern of the first Zernike mode: (A) unbiased mirror, (B) corrected bias, (C) tilt, (D) tip, (E) astigmatism 45°, (F) defocus, (G) astigmatism 0°, (H) trefoil 0°, (I) coma 90°, (J) coma 0°, (K) trefoil 30°.

a path difference of 7.57 μm or a deflection between the bias and the maximum deflection of 3.8 μm. We then obtain a maximum relative deflection of $\pm 3.8 \cdot 10^{-6}$ m.

The membrane mirror, after fabrication, is not perfect and has many aberrations, as it can be seen in the Figs. 3.1 or 5.9. These aberrations produce a different deflection capability, depending on the position of the electrodes which are activated. We measured this deflection for different electrode configurations. At the same time we have demonstrated that the membrane deflection is proportional to the square of the electrode voltage. The experimental results shown in Fig. 3.6, are obtained with the membrane mirror shown in Fig. 3.1. The electrode configurations correspond to six clusters of four electrodes located on the rim of the membrane. We applied a voltage of up to 160V and the deflection was measured in numbers of wavelength with a Helium-Neon laser at $\lambda = 633$ nm. We observe that we have up to 3 wavelengths of difference between two different groups of electrodes. Therefore, for a good modal deflection each membrane must be carefully calibrated to compensate such differences. Different weights must be given to the electrodes.

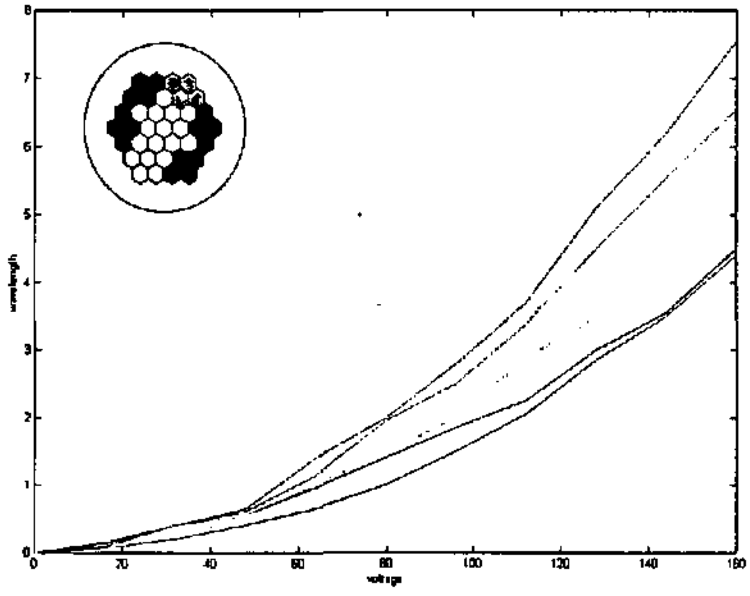

Figure 3.6: Deflection of the membrane mirror depending on the electrode groups.

As shown in section 3.2, the deflection of the membrane is proportional to the square of the voltage applied to it. The voltage applied to the electrodes is driven by a 40 channels Digital to Analog Converter (DAC) associated to a high voltage amplifier. The DAC has a resolution of 12 bit which gives a Least Significant Bit (LSB) of 1/4096. To set the membrane at mid distance of the maximum deflection, the bias is set at 2896 LSBs, which corresponds to a voltage of 141 V for a maximum voltage of 200V.

3.4.2 Initial aberration of the membrane

The initial aberrations of the membrane mirror are different for each mirror. In the case of a membrane with low aberrations (less than one wavelength), this is easy to correct by slightly different voltages on the electrodes and it is then possible to obtain the Zernike modes with good quality. In the case of an automatic search of the best correction in an optical system, we even do not need to correct aberrations, as this is automatically corrected by the search. In the case of several wavelengths of aberrations, it is no longer possible to obtain a correction of the membrane. Then it is no longer possible to obtain good quality Zernike modes and automatic optimization is limited by these aberrations.

3.4.3 Temporal response

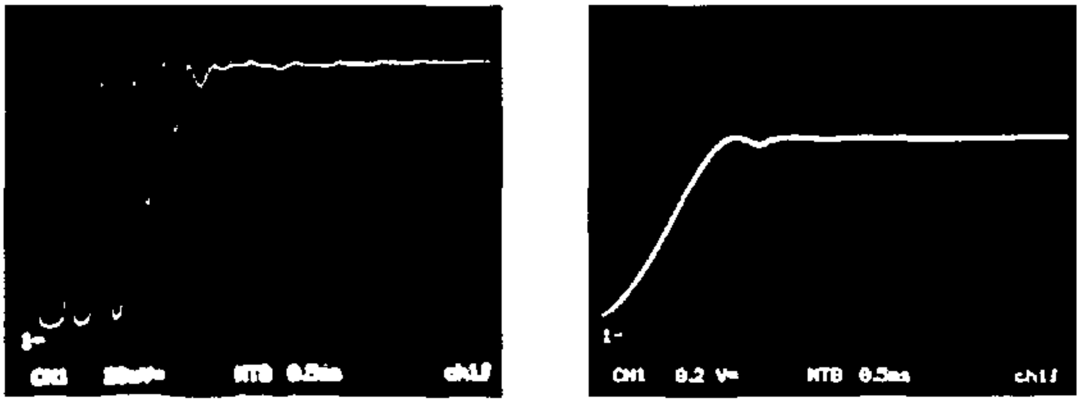

(a) (b)

Figure 3.7: Measurement of the temporal response of the membrane: (a) release time, (b) deflection time .

The maximum speed at which the membrane mirror is deflected or released has been measured. It determines the maximum working frequency of the mirror. These measurements have been made with a collimated laser beam reflected on the membrane mirror and coupled into a fiber. The deflection or release of the mirror changes the coupling into the fiber. The change in the output intensity of the fiber is detected by a photodiode and measured with an oscilloscope. Fig. 3.7(a) shows the measurement of the release time of the membrane; maximum coupling is obtained with the released membrane and reduced when the membrane is deflected. We see that the membrane is stable after 2.5 ms, which gives a frequency response of 400 Hz. In Fig. 3.7(b) the measurement of the deflection time of the membrane is shown; the maximum coupling is obtained with the deflected membrane and reduced when the membrane is released (flat). We see that the membrane is stable after 2 ms, which gives a frequency response of 500 Hz. The difference of response for these two cases is explained by the fact that during the release the membrane is not damped and has a natural vibration, as clearly shown in the measurements.

In an intermediate case, switching between two different voltages of 50V and 141V (bias voltage), the temporal response is faster. The damping behavior is also different. For small position changes, the membrane mirror can work up to 1 kHz.

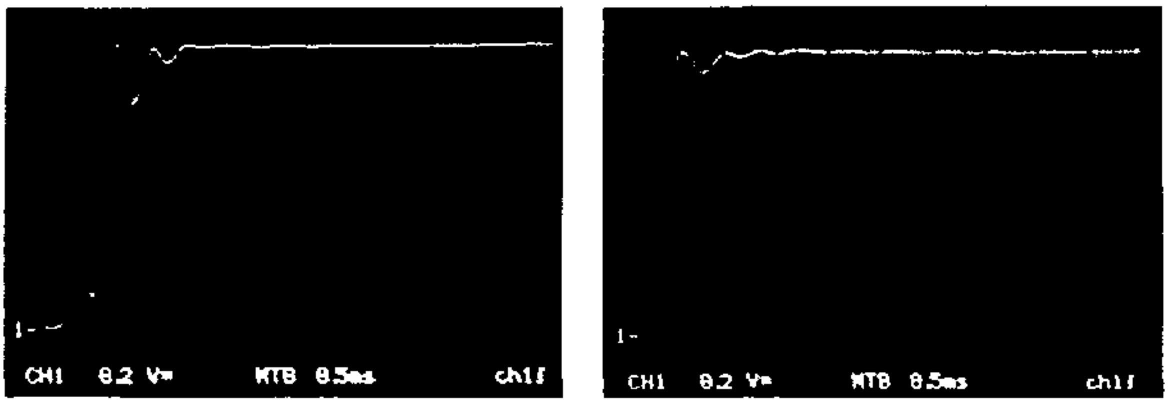

(a) (b)

Figure 3.8: 3.8Measurement of the temporal response for switching between 50 V and 141 V (bias): (a) release time, (b) deflection time.

3.4.4 Limits

The membrane mirror does not withstand electrostatic shocks. The contact of an human potential with an electrode connection can blow up the membrane.The membrane does not withstand mechanical contact, which means that it is not possible to clean it with a brush or a cloth.

We measured with the help of a high power diode laser[2] the reflectivity of the aluminum coated membrane at a wavelength of 805 nm. The initial reflectivity was 85 %. The surface of the mirror illuminated by the laser was 6 × 6 mm^2. The behavior of the membrane changes around 5 W and the membrane mirror was damaged at 8.3 W, which corresponds to a charge of 0.23 W/mm^2 and a power absorption of 34 mW/mm^2. Above this power, the PCB surface supporting the electrode structure begins to burn. In Fig. 3.9(a) we can see the membrane under laser stress and Fig. 3.9(b) shows the damaged membrane.

---

[2] The exact characteristics of this laser are given in 5.3.2.2

(a) (b)

Figure 3.9: Mirror under high power laser stress (a) and damaged mirror (b).

3.5 Summary

Membrane mirrors are the wavefront correctors used in this thesis. They have been developed by the Technical University of Delft. We first described their fabrication by anisotropic etching and their main characteristics, such as diameter and electrode array. We then explained physical behavior under electrostatic attraction. We presented a computer simulation program which allows to determine the required electrode voltages for any desired deformation. We determined the required voltage distributions to produce the Zernike modes. We finally described the measured characteristics of the membrane mirror: the quality of the deformation limited by the initial aberrations of the membrane, the temporal response limited by the release speed of the membrane and the limits of resistance to high power laser radiation.

Chapter 4

The Shack-Hartmann sensor

> "*If we had a means of continually measuring the deviation of rays from all parts of the mirror, and of amplifying and feeding back this information so as to correct locally the figure of the mirror in response to the schlieren pattern, we could expect to compensate for both the seeing and for any inherent imperfections of optical figure*" H. W. Babcock (born 1912)

In an adaptive optics system, the second most important element after the wavefront corrector is the wavefront sensor. As explained in Section 2.2.1.2, several types of wavefront sensors exist, working on different principles. We wish to use a wavefront sensor in the application described in Chapter 6. We have to analyse the wavefront used for each written hologram in one sequence of measurement. This is the reason why we have decided to build a Shack-Hartmann sensor. The great advantage compared to the lateral shearing interferometer is the simultaneous measurement of the x and y slopes produced by the wavefront change. We also preferred the wavefront sensor compared to the curvature sensor because it uses only one detector array, whereas the curvature sensor needs two of them. In fact, the Shack-Hartmann sensor is just composed of a detector array, a micro-lens array, and a telescope to reduce the size of the wavefront to the size of the detector array. We specifically developed the Shack-Hartmann sensor to analyse the wavefronts produced in the application described in Chapter 6. Its dynamic range has been calculated to cover all the possible deflections of the membrane mirror and its resolution to cover the smallest possible change. We have also chosen the spatial resolution adapted to the actuator array of the membrane mirror.

4.1 Principle

The Shack-Hartmann sensor is an evolution of the Hartmann sensor. Hartmann recognized, that the diffraction spot produced by a hole in a plate has a position which change with the angle of the incoming light beam on the plate. He deduced, that a matrix of holes in a plate could give the local tilt of the light beam at each hole and then reconstructs the wavefront [32]. His idea was used since the beginning of the 20^{th} century to test the quality of telescopes. Shack and Platt had the idea to dispose lenses on the holes to build a "Lenticular Hartmann Screen" in order to increase the displacement of the spot. This was done in 1970 for a U.S. Air Force laser project [82].

4.1.1 Design

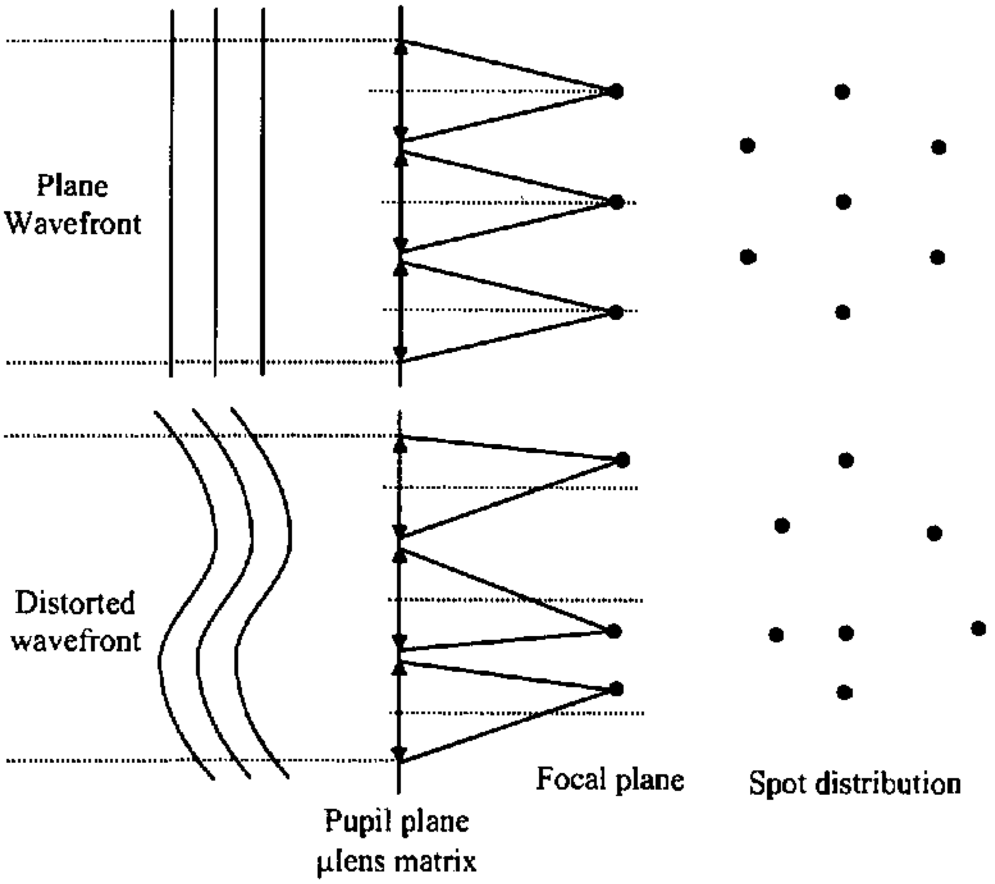

Figure 4.1: Principle of the Shack-Hartmann sensor

The Shack-Hartmann sensor is composed of an array of micro-lenses, an array of detectors, and of a telescope to reduce the size of the wavefront to the size of the detector. The type of lenses and their positions is different according to the detectors and the application of the Shack-Hartmann sensor. The type of detectors depends mainly on the required spatial resolution and the light intensity to be detected. In astronomical applications the light intensity can be as low as few photons, so that an array of photomultipliers becomes necessary. There are two main types of application for the Shack-Hartmann sensor, the first is the fine analysis of an incoming wavefront, the second is as a sensor for real-time correction of a wavefront. We will concentrate on the wavefront analysis, which is needed for our application. Since we have enough light, we will use a CCD camera as detector array. We have to determine how to measure the displacement of an Airy spot at the focus of the micro-lenses on the CCD.

4.1.2 Computation

The measurement obtained from the Shack-Hartmann sensor is the position of the spot produced by the micro-lenses. This change of position Δx and Δy in the x and y direction are measured. The Airy spot covers several pixels of the CCD camera. To find the position, we calculate the center of gravity of each spot, given by

$$c_x = \frac{\sum_{i,j} x_{i,j} I_{i,j}}{\sum_{i,j} I_{i,j}} \; and \; c_y = \frac{\sum_{i,j} y_{i,j} I_{i,j}}{\sum_{i,j} I_{i,j}}, \tag{4.1}$$

where $I_{i,j}$ is the intensity at the pixel (i,j) and $x_{i,j}$ and $y_{i,j}$ are the position coordinates. The sum is taken over all the pixels devoted to a micro-lens. The normalization by $\sum_{i,j} I_{i,j}$ reduces the sensitivity to the scintillation of the source. But we recognize also that the saturation of the pixels produces an error of measurement. The angle α_x corresponding to the average slope of the wavefront $\Phi(x,y)$ for the x axis on each subaperture (micro-lens) is given by

$$\alpha_x = \frac{\Delta x}{f \cdot M} = \frac{\lambda}{2\pi A_{sa}} \int_{subaperture} \frac{\partial \Phi}{\partial x} dx dy, \tag{4.2}$$

where Δx is the x-displacement of the spot, f is the focal length of the micro-lens, M is the magnification of the telescope, λ is the wavelength, and A_{sa} is the area of the subaperture for the micro-lens. The equation for the y-axis reads

$$\alpha_y = \frac{\Delta y}{f \cdot M} = \frac{\lambda}{2\pi A_{sa}} \int_{subaperture} \frac{\partial \Phi}{\partial y} dx dy. \tag{4.3}$$

The spatial resolution of the wavefront measurement is given by the pitch of the microlens array.

4.2 Sources of error

We can distinguish systematic and random errors. Systematic errors are mainly due to misalignment between the components of the Shack-Hartmann sensor, the telescope, the micro-lenses array and the CCD, but also due to the differences in the focal lengths of the micro-lenses and the variations of responsitivity of the pixels. Random errors are caused by the photon or shot noise and the electrical noise.

4.2.1 Spatial resolution error

We have seen than the measurement of the wavefront slope at each subaperture is an average. To resolve the wavefront shape produced by the membrane mirror, we must have a minimum spatial resolution. We have seen that our mirrors have 37 degrees of freedom in two dimensions. Following Nyquist we need a resolution of at least twice as many sample points per linear dimension, which means a minimum of 148 subapertures. We have chosen a hexagonal array of microlenses with a diameter of 256 μm over a CCD array of 4.1×4.1 mm^2. As explained in Sec. 4.4, this corresponds to 200 subapertures covering the surface of the membrane mirror with a resolution of 0.44 mm^2.

4.2.2 Misalignment error

The misalignment effects on Shack-Hartmann sensors have been studied by Pfund et al. [72]. They have divided the possible misalignments in four groups; the lateral translation, the axial translation, the rotation about the x and y axis, and the rotation about the z axis.

In case of lateral translation, all spots are displaced from their position by the same displacement vector, so that instead of Δx we obtain $\Delta x_{new} = \Delta x + \delta x$, where δx is the value of the displacement vector in the x direction, and the same for Δy. When reconstructing the wavefront from these measurements, this misalignment is considered as a tip or a tilt (as it will explained in Section 4.3). This only happens if there is a relative translation between the CCD camera and the micro-lens array between the reference measurement (or calibration) and the wavefront measurement.

An axial displacement has to be considered as a small change of the focal length of the microlens so that $f_{new} = f + \delta f$, where δf corresponds to the axial displacement. This will keep the shape of the reconstructed wavefront but the system will have to be recalibrated because it changes the amplitude of the wavefront variations.

The problem of rotation about the x- or y-axis is more difficult. In fact, the microlenses have no more the same distances from the CCD and we have a linear change of the sensitivity in the amplitude over the wavefront. The result is similar to a tilt in the wavefront. Pfund has calculated the tolerance angle for such misalignment, which is given by

$$\beta_{max} = \cos^{-1}\left(\frac{x_{max}}{\Delta x_{min} + x_{max}}\right), \tag{4.4}$$

where x_{max} is the maximum distance of a reference point to the axis of rotation and Δx_{min} is the smallest measurable displacement. In our case, the CCD bas a size of 4×4 mm^2, the maximum distance is thus 2 mm. Considering that the minimum measurable displacement is 1/100th of a pixel and that the size of the pixels are 16 μm, we obtain $\Delta x_{min} = 0.16\mu$m. Then the tolerance angle is 0.72°, which is easily obtainable.

The case of rotation around the optical axis (z axis) can be considered as a change of axis position for the interpretation of the Zernike modes, the tolerance is easily calculated by

$$\gamma_{min} = \frac{\Delta x_{min}}{x_{max}}. \tag{4.5}$$

We obtain $\gamma_{min} = 4.5 \cdot 10^{-3\circ}$. This problem of rotation is of course eliminated when a reference is taken just before the measurement.

4.2.3 Random errors or noise limitation

The error on the measurement is linked to the signal to noise ratio (SNR) of the detector. As given by [31], it is determined by the shot noise associated with the dark noise[1]. In the case of a CCD the additional source is mainly the electrons added to the charge of each pixel during the transfer to the on-chip amplifier. The signal to noise ratio for a generic CCD is given by

$$SNR = \frac{n_p}{\left[n_p + N_s\left(n_d^2 + n_e^2\right)\right]^{1/2}}, \tag{4.6}$$

where n_p is the number of detected photo-electrons per subaperture (all the pixels below one microlens), N_S is the number of pixels per subaperture, n_d is the number of dark electrons per pixel, n_e is the read noise in electron per pixel.

The standard deviation of the angular position error produced by the random noise has been found by [31] and [92] is then given by

$$\sigma = \frac{3\pi}{16}\frac{\lambda}{d}\frac{1}{SNR}, \tag{4.7}$$

where λ is the wavelength of the light and d is the diameter of the microlens. An estimation of the standard deviation is given in Section 4.4.1.

4.3 Wavefront reconstruction

The measurement of the subaperture wavefront slopes gives us only the local change of the wavefront. It is then necessary to reconstruct the overall wavefront. As explained by Southwell in [85], two methods are used to reconstruct the wavefront from the zonal slope measurements on the CCD: the zonal reconstruction and the modal reconstruction. The zonal reconstruction is generally applied to the closed-loop system [79]. It aims to minimize the error measurement or the wavefront variance. Good descriptions of this

---

[1] When used in astronomy, we have to include the background noise, which is photons not coming from the studied stellar object.

technique can be found in [68][78][85]. For our purpose we prefer the modal reconstruction to obtain the Zernike coefficients of the membrane mirror deformation. This method has been thoroughly discussed and described in [34], [13], [31] and [77].

Thus, the wavefront phase $\Phi(x, y)$ is given by

$$\Phi(x, y) = \sum_{K=1}^{M} a_K Z_K(x, y), \tag{4.8}$$

where a_K is the amplitude of the Zernike mode Z_K. The gradient α_x and α_y given by the Eqs. (4.2) and (4.3) are the partial derivatives of the wavefront :

$$\begin{aligned} \alpha_x(x, y) &= \tfrac{\partial}{\partial x}\Phi(x, y) \\ \alpha_y(x, y) &= \tfrac{\partial}{\partial y}\Phi(x, y) \end{aligned} \tag{4.9}$$

Using Eq. (4.8) and (4.9), the gradient at the specific location $n = (x_n, y_n)$ can be expressed as

$$\begin{aligned} \alpha_{xn} &= \tfrac{\partial}{\partial x}\Phi_n = \textstyle\sum_{k=1}^{M} a_K \tfrac{\partial}{\partial x} Z_{Kn}, \\ \alpha_{yn} &= \tfrac{\partial}{\partial y}\Phi_n = \textstyle\sum_{k=1}^{M} a_K \tfrac{\partial}{\partial y} Z_{Kn}. \end{aligned} \tag{4.10}$$

The Eq. (4.10) gives the relation between the gradients and the coefficients a_K and can be written in matrix form with a vector **p** containing the partial derivative α_{xn} and α_{yn} from 1 to n, a Zernike coefficient vector **a** and a matrix **D** containing the derivative of the Zernike polynomials. This matrix form is written

$$\mathbf{p} = \mathbf{Da}, \tag{4.11}$$

which is equivalent to

$$\begin{bmatrix} \alpha_{x1} \\ \vdots \\ \alpha_{xn} \\ \alpha_{y1} \\ \vdots \\ \alpha_{yn} \end{bmatrix} = \begin{bmatrix} \frac{\partial}{\partial x} Z_{1,1} & \cdots & \frac{\partial}{\partial x} Z_{K,1} & \frac{\partial}{\partial y} Z_{1,1} & \cdots & \frac{\partial}{\partial y} Z_{K,1} \\ \frac{\partial}{\partial x} Z_{1,2} & \cdots & \frac{\partial}{\partial x} Z_{k,2} & \frac{\partial}{\partial y} Z_{1,2} & \cdots & \frac{\partial}{\partial y} Z_{K,2} \\ \vdots & \vdots & \vdots & \vdots & \vdots & \vdots \\ \frac{\partial}{\partial x} Z_{1,n} & \cdots & \frac{\partial}{\partial x} Z_{K,n} & \frac{\partial}{\partial y} Z_{1,n} & \cdots & \frac{\partial}{\partial y} Z_{K,n} \end{bmatrix} \begin{bmatrix} a_1 & a_2 & \cdots & a_M \end{bmatrix}. \tag{4.12}$$

The solution of the coefficient vector a is found by taking the pseudo inverse of **D**, which becomes

$$\mathbf{a} = \left[\left(\mathbf{D}^T\mathbf{D}\right)^{-1}\mathbf{D}^T\right]\mathbf{p}. \tag{4.13}$$

4.4 The prototype

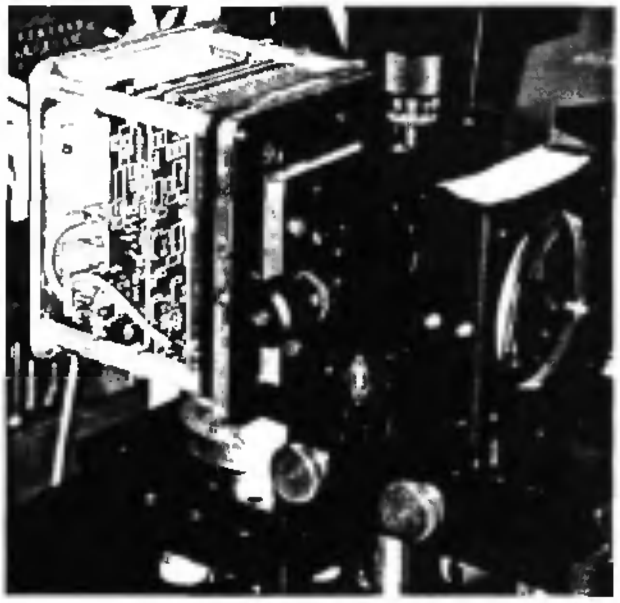

Figure 4.2: Photograph of the Shack-Hartmann sensor

Figure 4.2 shows the photograph of the Shack-Hartmann sensor. The CCD camera is mounted on a 3D stage, the array of micro lenses is supported by the 2D holder. The telescope to reduce the diameter of the optical beam to be analysed is composed of two lenses in front of the sensor. The 3D stage is used to align the CCD camera with the optical axis of the system. The 2D holder is used to position the microlens in front of the CCD camera.

4.4.1 The CCD camera

A/D converter	12 bit
Frame rate	136 Hz
Effective area	4.1×4.1 mm
Effective nbr of pixels	256×256
pixel size	16×16 μm
pixel clock rate	10 MHz/pixel
Dark noise	30 DN
Random noise	5 DN
Photoresponse non uniformity	4%
Responsitivity at 488nm	50 DN/(nJ/cm^2)

Table 4.1: Camera DALSA CA-D1 datum (DN is for digital number)

The main characteristics are given in Table 4.1. It is a DALSA CA-D1 with 12 bit of resolution and a matrix of 256×256 pixels. We have chosen it for the low random noise and high frame rate, which gives the possibility to average several images to reduce the influence of mechanical and optical noise. Typically we made an average of 10 frames for each acquisition.

We can make an estimation of the SNR and of the standard deviations with the characteristics of the CCD camera used for the prototype and given in Table 4.1. The energy for one photon at a wavelength of 488 nm is $E = \frac{hc}{\lambda} = 4.07 \cdot 10^{-19}$ J. The responsitivity at 488 nm of the CCD camera is given in Table 4.1 and is $R = 50$ DN/(nJ/cm^2). The size of each pixel is 16×16 μm^2. Therefore 50 DN on a pixel corresponds to $2.56 \cdot 10^{-15}$ J and one DN $5.12 \cdot 10^{-17}$ J, which corresponds to the energy of 126 photons. In Table 4.1, the noise is given in digit, thus we can translate it in photo-electrons. The Shack-Hartmann is designed with subaperture covering 16×16 pixels and most of the energy of the spot covers 4×4 pixels as it will be explained in Sec. 4.4.3. Let says that the 16 pixels covered by the spot are nearly saturated, this corresponds to 64000 digits. With $n_p = 64000 \times 126$ photo-electrons, $N_S = 256$ pixels, $n_d = 30 \times 126$ electrons and $n_e = 5 \times 126$ electrons, we obtain a SNR of 568. Then at a wavelength of 488 nm and with microlenses with a diameter of 256 μm. we obtain a standard deviation of 1.98 μrad.

4.4.2 Design of the microlenses

The need of a high spatial resolution and of a high angular resolution impose the use of microlenses with a low numerical aperture (NA). Different methods to manufacture the microlenses are given in [3], [111] and [69]. We have chosen a 5×5 mm^2 hexagonal matrix of microlenses with a diameter $D = 256$ μm and a focal length $f = 15$ mm. The hexagonal shape has been chosen to obtain a fill factor of 100%. This array has been manufactured at the CSEM[2] by direct laser beam writing in photoresist and then replicated on silica substrate [25].

The diffraction spot detected by the CCD pixels can be approximated as being produced by a circular aperture. The radius of the spot which corresponds to the first dark ring is

$$w = 1.22\frac{\lambda f}{D}.$$

With $\lambda = 488$ nm, $f = 15$ mm and $D = 256$ μm, we then obtain $w = 34.8$ μm. In the first dark ring is concentrated 82% of the total energy, to get more than 96% we need to take account of the second dark ring [56], which means a radius of 69.6 μm or a surface of 8×8 pixels. Considering of the second dark ring avoids also overlapping of the spots.

---

[2] Centre Suisse d'Electronique et de Microtechnique

4.4.3 Resolution

We have to reduce the optical beam of our system from the 12 mm diameter of the active mirror aperture to 4 mm the size of the CCD detector. This is done with the help of two achromatic doublet lenses of 300 mm and 100 mm of focal length forming a Keplerian telescope.

Each microlens covers a surface of 16×16 pixels and each diffraction spot covers a surface of 8×8 pixels. Therefore we have a free move on each side of 4 pixels, which is ±64 μm. From Eq. (4.2), we find a maximum angle of $1.4{\cdot}10^{-3}$ rad.

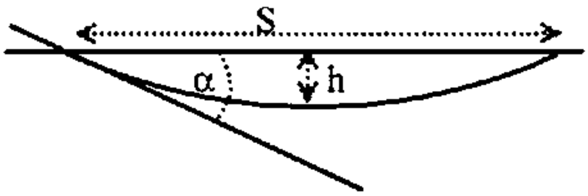

Figure 4.3: Maximum angle for a spherical membrane mirror deflection.

The maximum angle of a spherical deflection as shown in Fig. 4.3 is given by

$$\alpha = 2\tan^{-1}\left(\frac{2h}{s}\right), \tag{4.14}$$

where h is the deflection and s is the diameter of the aperture of the membrane. For $h = 4.5$ μm and $s = 12$ mm we obtain an angle of $\alpha = 1.4 \cdot 10^{-3}$ rad, which is just equal to the capability of the sensor.

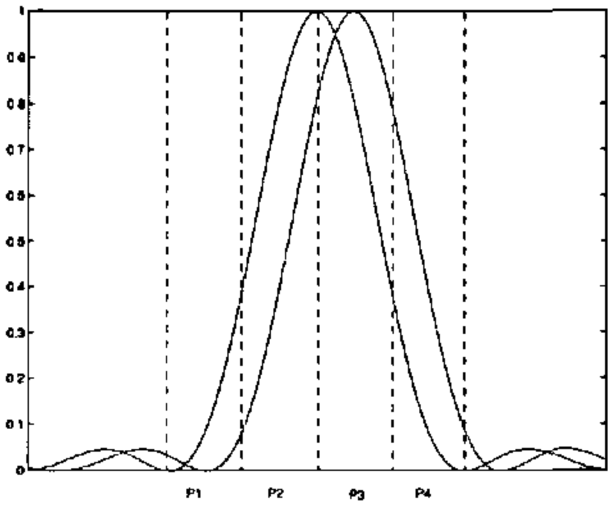

Figure 4.4: Distribution of the airy function over the pixels

The minimum measurement capability depends on the sensitivity of the CCD camera. As we have seen, the spot covers a surface of around 8×8 pixels but the airy disc is contained in a surface of 4×4 pixels. Theoretically, the minimum measurable slop is given by the change of one least significant bit (1/4096 of the maximum intensity to be measured) on at least one pixel. It is important that the pixels centered on the airy disk of the microlenses are close to the saturation. Looking at the intensity distribution of the airy disk, as shown in the Fig. (4.4), we see that the strongest intensity change is produced at the center of the airy disc. The Fig. (4.4) shows two airy functions with a shift of half a pixel. With a simulation on MATLAB, we calculated for a change of 1/4096 of intensity a shift of 1/2500 pixel lengths or 6.4 nm. Taking into account the shot noise and the dark noise, which corresponds to 35 digits, reduces greatly the theoretical limit to 1/90 pixel lengths or 0.18 μm. We know that a noise of 35 digits is the worst case and that we can average several pictures to reduce the impact of this noise, so that we can expect a sensitivity of about 1/100 pixel lengths or 0.16 μm, which correspond to a minimum measurable slope of 3.56 μrad.

The minimum deformation of the membrane is produced by one digit from its bias position, this corresponds to a deflection of 3.1 nm or an angle of 1 μrad. To obtain such resolution, we would need a sensitivity of 0.045 μm which corresponds to 1/356 pixel lengths.

4.5 Calibration and applications

Figure 4.5: Spot detected by the CCD camera.

Figure (4.5) shows a typical detection of the Airy spot. We see that we have the expected 4 × 4 illuminated pixels. We checked first the mechanical stability of the system and then the electronic noise. We measured also the minimum resolution of the prototype with the help of the membrane mirror. We have developed an acquisition procedure to measure and calculate the deformations of the membrane mirror.

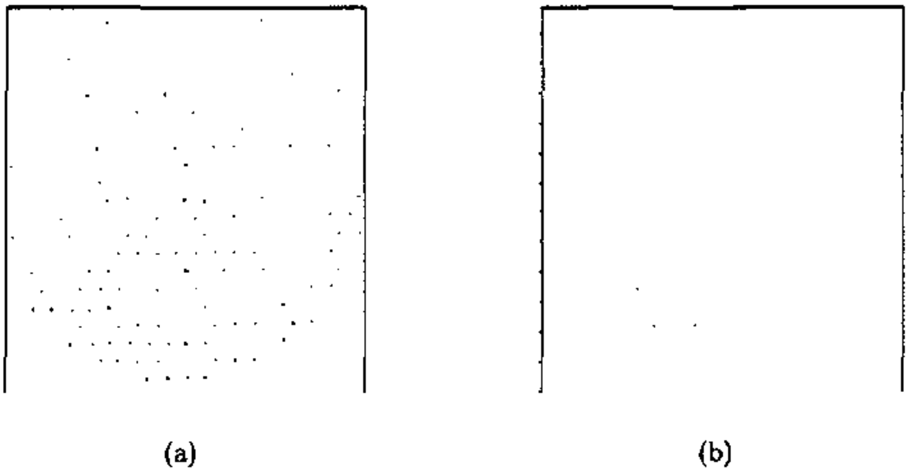

Figure 4.6: Typical distribution of noisy pixels: (a) noise below 16 digits, (b) noise between 16 and 32 digits.

4.5.1 Stability of the system

First we measured the noise of the CCD camera by comparing the acquisition of the same wavefront taken twice. Each acquisition is an average of 10 frames as explained in Sec. 4.4.1. This measurement had been made on several wavefronts. We never obtained pixels with a difference of the intensity of more than 32 digits. Typically we obtained about 100 pixels or less with a change of less than 16 digits and about 5 pixels with an average comprised between 16 and 32 digits. A typical distribution of these pixels is shown in Fig. 4.6. The measured noise is even smaller than given by the characteristics of the CCD camera in Table 4.1. It shows that the estimation of resolution made in subsection 4.4.3 is perfectly realistic and that we can even expect a better resolution.

4.5.2 Measurement of the minimum resolution

We did not have a tilt mirror with the precision required for this type of measurement. Therefore, we decided to measure the smallest possible deflection change on the membrane mirror and to compare it with the resolution given in 4.4.3. The smallest deflection change is adding or removing 1 digit of voltage to the biased mirror, which is set to 2895 digits. As we have seen in Sec. 4.4.3, this corresponds to a deflection change of 3.1 nm or a maximum change of slope of 1 μrad. Doing so, we can observe a change of the intensity distribution of pixels and after centroiding calculation, the measurement gives a change of the spot position between 0 to 0.02 pixels. But by adding or removing a second digit of the voltage, we observe a spot position change of up to 0.035 pixels, clearly showing a defocus with tilt. By increasing the deformation by a few more digits, we obtain the expected defocus. Even by taking into account that we do not know exactly the behavior of the membrane mirror under such small voltage changes, it shows that the sensitivity of the Shack-Hartmann sensor is in the limit of the minimum deformation change of the membrane mirror. From these results we believe that the estimated resolution of 1/100 pixels is a good approximation.

4.5.3 Acquisition

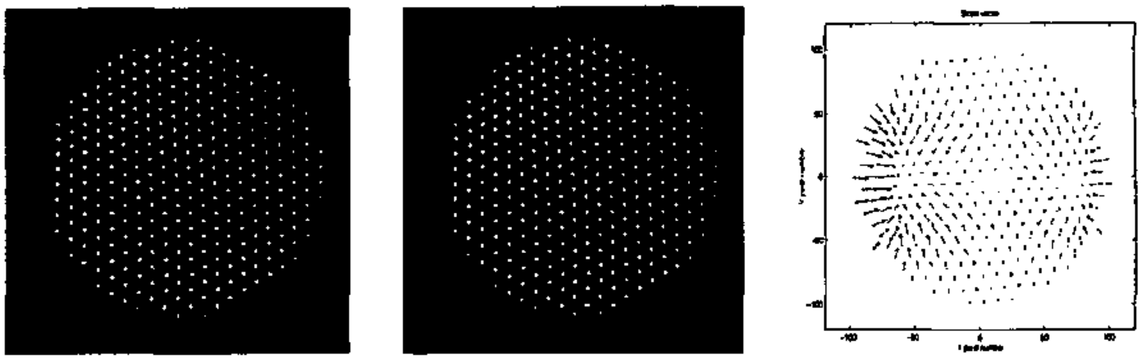

(a) (b) (c)

Figure 4.7: Acquisition of reference (biased mirror) (a), changed wavefront (b), and calculated slope (c).

The Shack-Hartmann sensor is controlled with LABVIEW. We make an average of 10 acquisitions per wavefront analysis to reduce the noise. A centroid algorithm (Eq. (4.1)) calculates the positions of the spots. The difference between the spot position of the reference wavefront and the analysed wavefront gives the slope of the wavefront. The measured slope pattern is used to calculate the Zernike coefficient with the help of an algorithm, also written on MATLAB. This algorithm follows the principle given in section 4.3. The different steps are shown in Figs 4.7 and 4.8. The spot distribution of Fig. 4.7 (a) corresponds to the reference wavefront (biased membrane mirror) and Fig. 4.7 (b) to the changed wavefront. The slope calculated from these two spot distribution is shown in Fig. 4.7 (c). The corresponding Zernike coefficients are presented in Fig. 4.8 (a). From these coefficients we restore the deformation of the membrane mirror (Fig. 4.8 (b)).

4.6 Conclusion

We have developed a wavefront sensor to specifically measure the deformation changes of the membrane mirror. We made our choice on a Shack-Hartmann sensor, because it measures simultaneously the x and y slopes with only one CCD camera. The prototype is composed of a commercially available CCD camera and of a microlens array designed

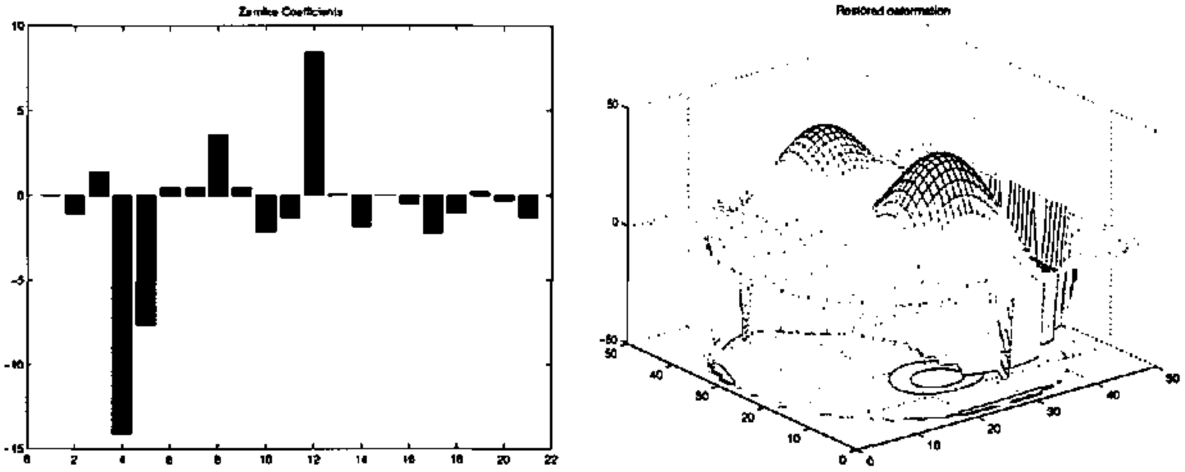

(a) (b)

Figure 4.8: Measured Zernike coefficients (Noll classification) (a) and restored deformations (b)

for this purpose and fabricated at the CSEM. The prototype with a measurement range of 1.4 mrad and a minimum resolution of at least 3.5 μrad, fully covers the maximal and minimal deflection capability of the membrane mirror. The resolution is not limited by the alignments, but by the noise of the CCD camera. From the measured slopes we calculate the in Zernike coefficients and from these coefficients we can restore the deformation of the membrane mirror.

Chapter 5

Closed-loop systems

> *"It would seem inappropriate to speak of one of these hypothetical entities as a particle of light, a light quantum, or a light quant, if we are to assume that it spends only a minute fraction of its existence as a carrier of radiant energy, while the rest of the time it remains as an important structural element within the atom. It would also cause confusion to call it merely quantum, for later it will be necessary to distinguish between the number of these entities present in an atom and the so-called quantum number. I therefore take the liberty of proposing for this hypothetical new atom, which is not light but plays an essential part in every process of radiation, the name photon."* Gilbert Newton Lewis (1875-1946).

Although the use of a water jet to guide light has been demonstrated in 1870 by J. Tyndall [93], it was not before 1954 that the transmission of information has been demonstrated through a cladded dielectric wave guide [95]. At the end of the sixties the first low absorption silica glass fibers were produced [40] and opened the path of a revolution in the communication and optical domain. If several solutions have been proposed for the coupling of the light sources into glass fibers, it remains anyway a problem. It is usually hard to obtain a good fiber coupling even in the most simple and well aligned set-up [45]. We developed a set-up which couples a plane wavefront into a single mode fiber to demonstrate the potential of a deformable membrane mirror for such purpose. Thanks to this demonstrator, we were able to investigate different algorithms to optimize the coupling efficiency. We diverged from a classical adaptive optical system, because we do not measure the wavefront of the light beam but we optimize directly the output intensity of the fiber system. We developed two applications where the use of adaptive optics brought a large advantage. The first application is a single-mode telecom fiber switch, the second is the coupling of a diode laser pump into double-clad doped fiber amplifiers.

5.1 Optimization of single-mode fiber coupling

Basically, some light source is reflected on a membrane mirror to be properly coupled into a single-mode fiber. The intensity of the light is detected at the output of the fiber. The intensity is the information used to change the deformation of the membrane mirror and to obtain a better coupling. We mounted a set-up to test this idea. This set-up produces a plane wavefront from a laser source which is reflected on the membrane mirror before it is coupled into a single-mode fiber.

Efficient coupling of light into single-mode fibers is a current problem in many optical systems. It is a time consuming task, which in general is done manually once, with the risk of subsequent drifts. Furthermore, the coupling efficiency remains low when the wavefront is not Gaussian. We propose an automatic injection method, based on the adjustment of the optical beam wavefront with an adaptive membrane mirror (see Ch. 3), which is a low cost adaptive optics corrector. For the demonstration, we generate a plane wavefront from a He-Ne laser. The beam is reflected on the membrane mirror before being coupled into a single-mode fiber. The membrane mirror has an active area of 12 mm in diameter, activated by 37 electrodes which electrostatically attract the membrane.

We decided to build a closed-loop system, which uses the efficiency of the coupling as adjustment variable. The optimization is done on the output intensity of the fiber. Four optimization programs have been tested. The first approach is to optimize the electrode voltages to obtain the best coupling. The second approach is to find the best combination of low-order Zernike modes. For both approaches, two different optimization algorithms are compared. The first one is a maximization algorithm. Electrode by electrode or mode by mode are optimized to get the best coupling. The second algorithm uses an evolutionary algorithm [20], which follows the Darwinian principle. Each membrane deformation is considered as an individual which is determined by a set of electrode voltages or by a set of Zernike polynomials. These polynomials are aberration polynomials defined by Zernike in 1934 [113]. They have the advantages to be orthonormal, complete (any wavefront can be described by a linear combination of Zernike polynomials) and invariant to rotation [9] (see Ch. 2).

5.1.1 The test set-up

The set-up is shown in Fig. 5.1. The beam from the He-Ne laser is enlarged by the telescope formed by the lenses L1 and L2, and clipped by the stop aperture S1 to generate a plane wavefront. It is then reflected on the deformable mirror M2 and injected into the single-mode fiber through the beam splitter BS2 and the injection lens L3 of 40 mm focal length. To transmit all the optical power reflected by the mirror into the the fiber, this beam splitter BS2 can be advantageously replaced by a polarized beam splitter and a quarter wave plate. A Michelson interferometer, formed by the beam splitter BS1, the reference mirror M1, and the deformable mirror M2, is added to the set-up to image the

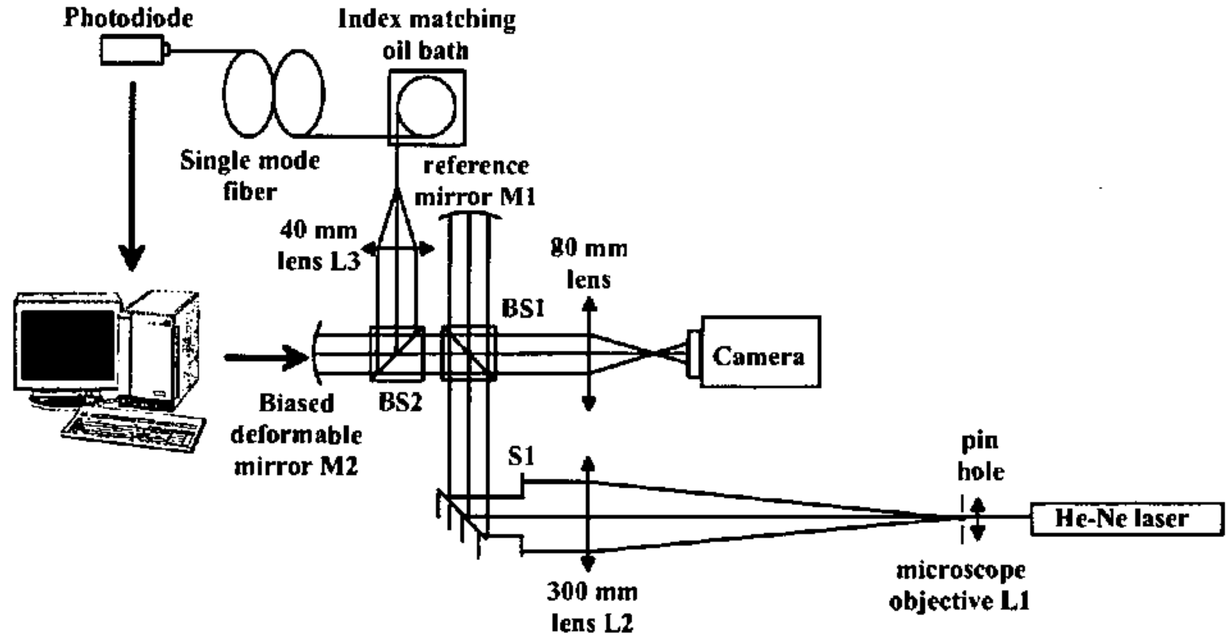

Figure 5.1: Breadboard to test fiber coupling

deformation of the membrane mirror on the camera. The mirror M1 has a focal length of 2 m, corresponding to the focal length of the deformable mirror M2 when the bias voltage is applied.

The deformable mirror is an adaptive membrane mirror produced by the Technical University of Delft [99], as described in Chapter 3. The maximum operating frequency of the mirror is 1 kHz, but to obtain a good stabilization of the membrane, we preferred to work at 330 Hz. The mirror is activated with 37 hexagonally disposed electrodes, which attract electrostatically the membrane. With this principle only deflections in one direction can be produced. Therefore, a bias voltage is applied to allow deflections in both directions. The maximum voltage that can be applied to the electrodes is 200 V. The deflection is proportional to the square of the voltage. We apply a bias of 141 V, which gives a spherical surface to the mirror with a focal length of 2 m. This membrane mirror can produce the low-order Zernike modes [9]. The optimization of the deformation of the membrane mirror can be made directly by changing the voltage of the electrodes or applying a set of different Zernike polynomials to create a specific deformation. The order of the modes which can be produced by the mirror is limited by its spatial resolution (only 37 electrodes activate the membrane) and by the deflection range for each mode. The electrodes of the membrane mirror are controlled with a 12 bit DAC card giving a resolution of 4096 least significant bit (LSB), which means a potential of $4.53 \cdot 10^{133}$ deformations.

We used a single-mode fiber optimized for the wavelength of 633 nm with a core diameter of 4 μm and a numerical aperture of $NA = 0.13$. The radius of the diffraction limited spot produced by the lens L3 is

$$w = 1.22\frac{\lambda f}{D}, \tag{5.1}$$

where λ is the wavelength, f is the focal length of the lens L3, and D is the diameter of the diaphragm, which corresponds to the diameter of the active area of the mirror. We obtain w =2.57 μm for D = 12 mm and f = 40 mm. The radius is larger than the radius of the core of the fiber. For a perfect fit, we would need of focal length of $f = D/(2NA) = 46$ mm. This incompatibility produces an injection loss of around 50 %. To eliminate the light coupled into the cladding and to ensure that we really optimize the coupling into the core of the fiber, the protective coating of the fiber is removed on a length of 10 cm and the fiber is immersed in a bath of index matching oil.

A closed-loop system controlled by a computer adjusts the shape of the adaptive mirror to optimize the efficiency of the coupling. The output intensity of the fiber is detected by a photodiode and fed to the computer via a 16 bit analog to digital card. The 37 electrodes of the mirror are controlled through a 40 channels, 12 bit digital to analog card.

Before starting the optimization with the bias voltage of 141 V applied to the mirror electrodes, the coupling of the light into the fiber is manually optimized by adjusting the fiber holder on its 3 axes.

5.1.2 Optimization program

In classical adaptive optics system, a wavefront sensor determines the aberrations from which the command control determines the best corrector shape. However, in our case the important matter is the amount of light coupled into the fiber, which can be directly measured at the output of the fiber with a photodiode. From this information we can program a command control to change the shape of the mirror until the best coupling is obtained. The measurement with a wavefront sensor is no more needed. We have investigated different optimization programs and compared the obtained results.

5.1.2.1 Maximization algorithms

The first algorithm optimizes the membrane deformation, electrode by electrode or Zernike coefficient by Zernike coefficient. It scans the voltage of each electrode or the coefficient of each mode to find the best value. Then, it classifies the electrodes or modes by the gain in intensity obtained for the coupling and starts a new iteration. In the case of optimizing the electrode voltages, as shown in Fig. 5.2, the voltage is first scanned by steps of 400 LSBs. The final voltage for each electrode will be between the two values which gave the best output efficiencies. These two values are recorded and a finer scan with steps of 40 LSBs is performed between the two values; once again the two best values are recorded and again a new scan with steps of 10 LSBs is performed, followed by a last scan with steps of 1 LSB. By doing so, we obtain the best voltage for each electrode with a maximum

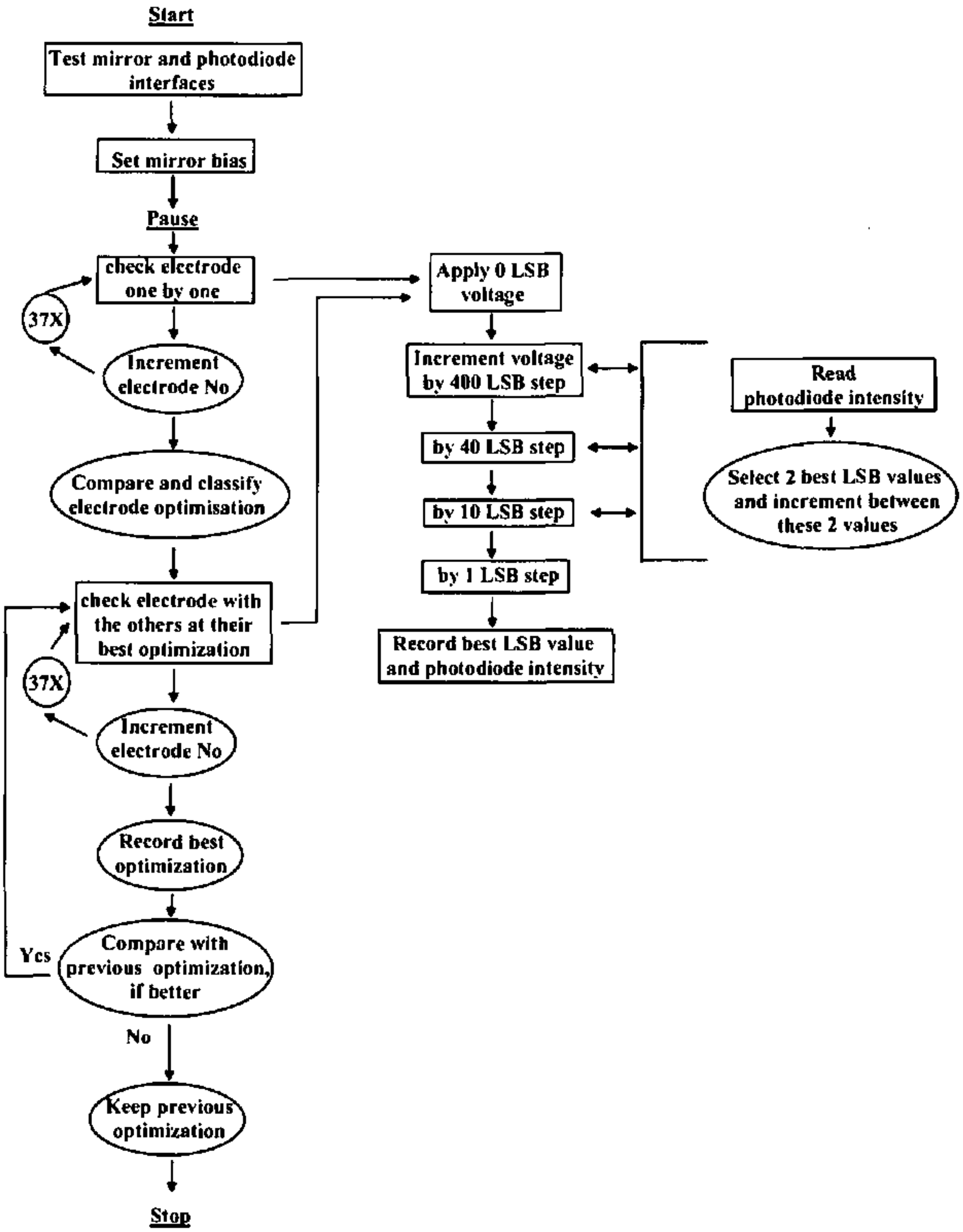

Figure 5.2: Algorithm for the direct optimization of the electrode voltages.

of 34 measurements, which yields for the scanning of the 37 electrodes a maximum of 1258 measurements per iteration. In the case of the Zernike coefficients, we use the same principle and produce around 600 deflections per iteration. The program stops when a local maximum is reached, which happens usually within less than 10 iterations. With this algorithm, the number of deformations checked to reach the maximum is small compared with the number of possible deformations.

5.1.2.2 Evolutionary algorithm

Turing [91] asked the following question in 1950 : "Can machines think?" Rather than answering, he proposed the now famous Turing test known essentially by its use in Science-fiction[1]. He also compared the human process of learning with the evolution. Since this date a specific domain in computing has been created and called Artificial Intelligence. The first step has been to look for a learning process and the proposed solutions of evolution have been deeply studied. The evolutionary programming is now a specific branch of programming.

The second algorithm follows the principle of the evolutionary theory of the neo-Darwinian paradigm. The different steps describing the algorithm are the following: reproduction, mutation, competition, selection. In our model we consider each possible shape of the mirror as an individual. Each individual can be described by either a set of electrode voltages or a set of Zernike polynomials, which are called the genetic code. A random population is designed and tested. The best individuals of this population are selected for reproduction (they become parents). The reproduction is made by mixing the genetic code of the parents to create a progeny. During the mixing a small part of the genetic codes undergo a mutation (as it happens in a natural evolution), which is a random change of some codes. The obtained progeny is tested and compared to its parents. The best individuals from the comparison are selected to become the new parents. After several iterations the best optimization is obtained.

The Fig. 5.3 shows the block diagram of the algorithm with the parameters used during the process. The mirror bias is set after the check of the electronic interfaces of the experiment. A population of 500 individuals is randomly chosen and tested. We keep the 100 best individuals of this population. The first 10 individuals are kept unchanged, while the 90 others are mutated to a level of 10%. This population of 100 individuals is the starting population for the evolution process. We keep the first 10 individuals as reference and we start the progeny creation. The 3 first individuals will create 20 children. 50% of these children will undergo a mutation of 1% of their genetic code. We also create 70 children with the 10 parents. These 70 children undergo a mutation of 10%. By adding all the children and the reference population we obtain a new population of 100 individual. We can test them and start again the progeny creation until the best individual is obtained.

---

[1] For e.g. "2001 the Space Odyssey" in which HAL, the computer which controls the spacecraft, passed successfully the Turing test.

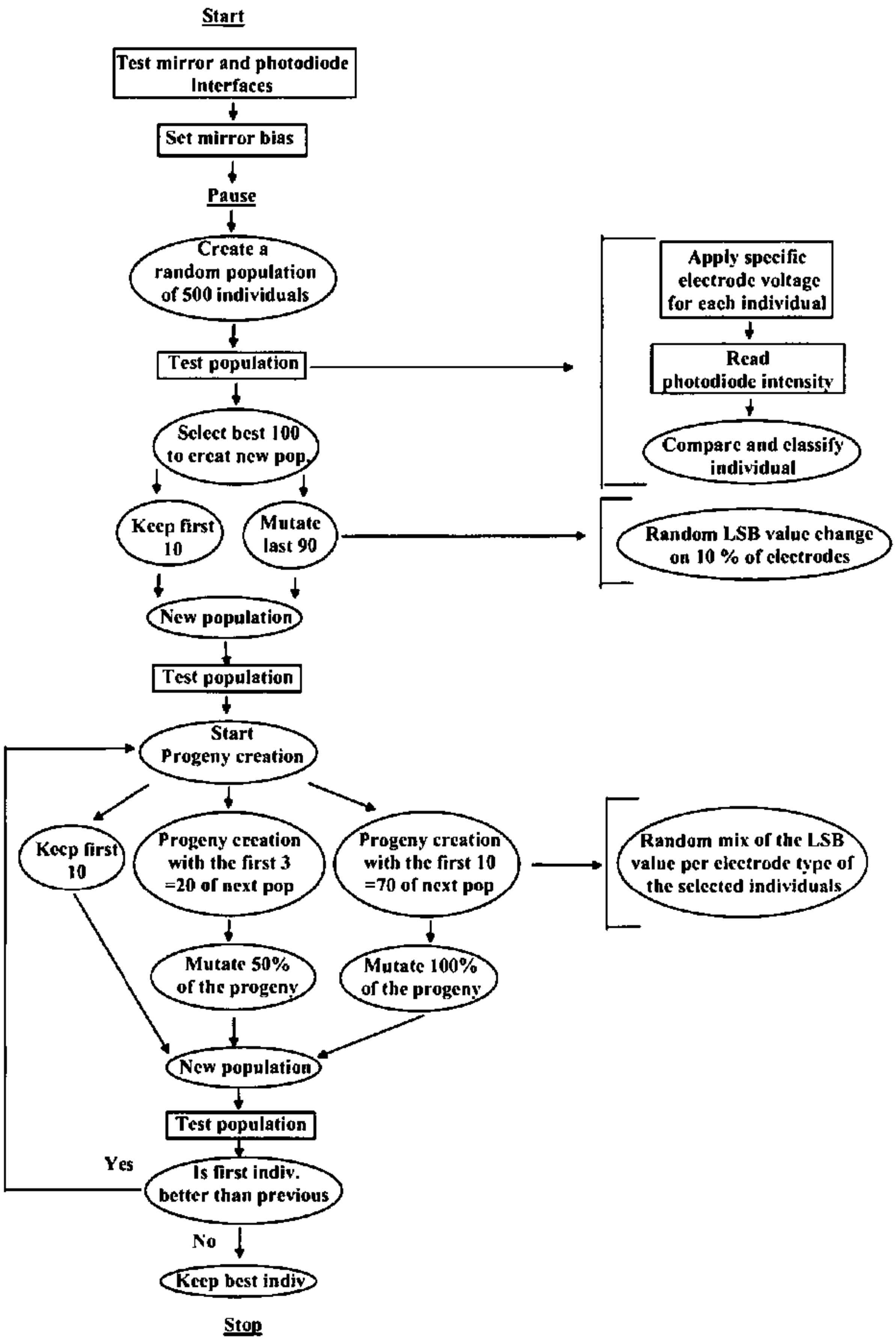

Figure 5.3: Diagram of the evolutionary algorithm

5.1.2.3 Optimization test and results

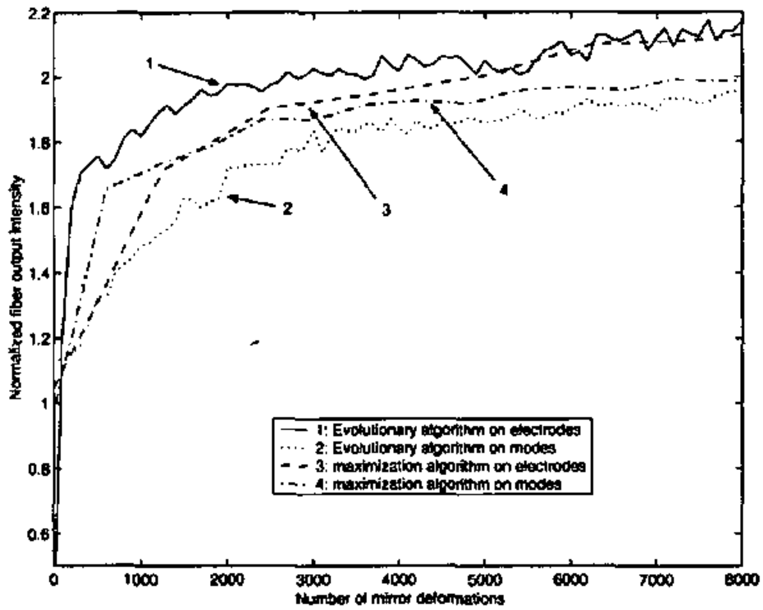

Figure 5.4: Intensity optimization with different algorithms

Figure 5.4 shows typical results of the improvement of the coupling efficiency obtained with the four programs, plotted as a function of the number of tested mirror deformations. The coupling efficiency is normalized with respect to the best value obtained manually. For all four curves, the maximum is obtained after less than 8000 deformations, which has to be compared with the total number of $4.53 \cdot 10^{133}$ possible deformations.

The optimization made on the Zernike polynomials with the two algorithms lead to an increase of the efficiency by a factor of at least 1.9. With the two algorithms working on the electrodes, the increase of efficiency goes up to a factor of 2.2. We notice also that the evolutionary algorithm applied to the electrodes improves the coupling faster than the others.

5.1.3 Conclusion

We have demonstrated the use of a membrane mirror to improve the efficiency of the injection of a beam with a plane wavefront into a singlemode fiber. With an appropriate algorithm, we have obtained a gain in efficiency of more than a factor of 2 compared to the best value obtained by manual optimization. We have tested two optimization algorithms, a simple maximization algorithm and an evolutionary algorithm, and we have applied both to optimize either the electrode voltages or a set of Zernike modes of the mirror. We have obtained better results working on the electrode voltages than with the Zernike modes. This is due to the fact that in theory any deformation can be reproduced with an infinite set of Zernike modes, but in practice we can only use a finite number of Zernike modes. This limits the spatial resolution of the possible deformations. The two algorithms gave similar results in both cases but in general the evolutionary algorithm converges faster.

We will demonstrate the use of this concept in two different applications, the fiber switch and the dynamic coupling of the optical pump for double clad fiber amplifiers.

5.2 Massive telecom fiber switch

During the past few years, the demand for optical telecommunications has boomed [7]. In order to satisfy this demand, new optical switches are required to replace the electrical switches used until now. Optical switches with few interconnects (1×2, 2×2) have been published for a couple of years [59]. Nevertheless, optical telecommunication networks need optical switches with large number of interconnects. Alignment tolerance, diffraction of the Gaussian beams and aberrations are parameters which are more critical for optical switches with large number of interconnects than for optical switches with a few interconnects. Most of the published optical switches with large number of interconnects are using micro-mirrors with sizes in the range of 100 μm to 500 μm [30], [48] and [66]. These switches have relatively small collimated beams which limit their expandability due to diffraction [47]. Another approach (without micro-mirrors) is to use a macro lens and have larger collimated beams. With this approach, the diffraction of the Gaussian beam is less critical, but aberrations become significant. To overcome this drawback, there are two possible ways. One is to use a diffraction limited designed lens as proposed by Ford and DiGiovanni [21]. The other way, which has been chosen here, is to use a conventional lens and correct for the aberrations using an adaptive mirror. In this work, a 1×N optical fiber switch is studied. Investigations are conducted to describe the physical properties of the switch and to determine the limitations. The merit function of the optical switches is their coupling efficiency. The limitations, mainly due to the aberrations and misalignments of the optical components, are overcome using the micromachined membrane deformable mirror developed at T.U. Delft and described in Ch. 3. A prototype with 32 fibers has been developed.

5.2.1 Concept

We have developed a 1×N switch for monomode fiber optical communication systems, which is composed of an array of fibers, an achromatic lens and an adaptive membrane mirror. The optical system has two functions. First, it images a single-mode source fiber onto another single-mode receiver fiber. Second, it deflects the beam to address one of the receiver fibers (switching function). Fig. 5.5 shows the system composed of a fiber bundle, a lens and a mirror. The source fiber is imaged (4-f system) onto one of the receiver fibers by moving the lens laterally. However, using the achromatic lens under off-axis conditions

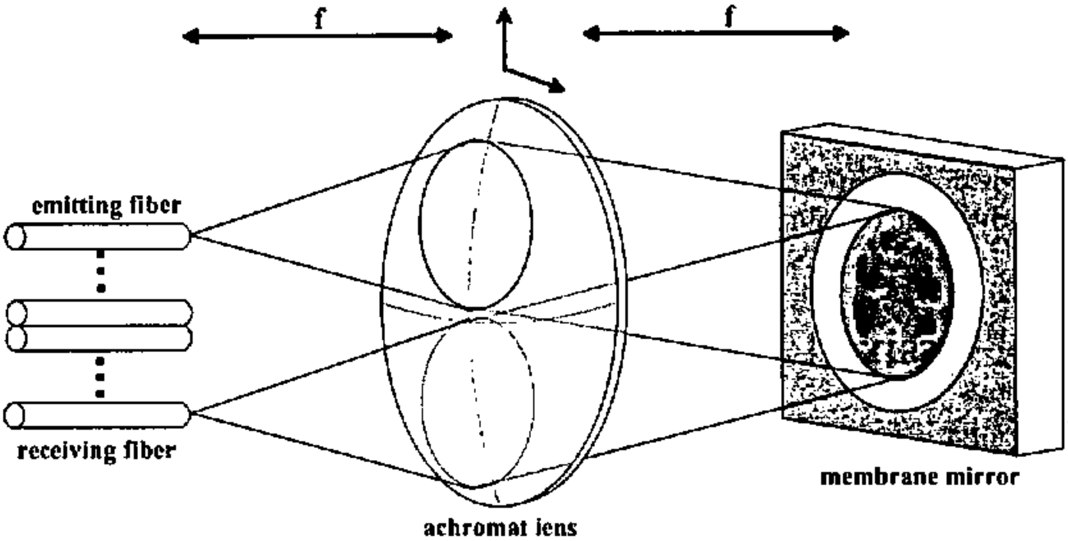

Figure 5.5: The fiber switch principle

introduces aberrations, which cause coupling losses to the receiving single-mode fibers. The deformable mirror is used to adaptively correct these aberrations. The optimization of the coupling efficiency is made with the help of an evolutionary algorithm as explained in section 5.1.2.2. For each position of the lens, the optimized voltages on the electrodes of the membrane mirror can be stored during the calibration procedure and afterward recalled during operation of the switch. A demonstrator has been set up with an array of 32 fibers.

5.2.2 Breadboard

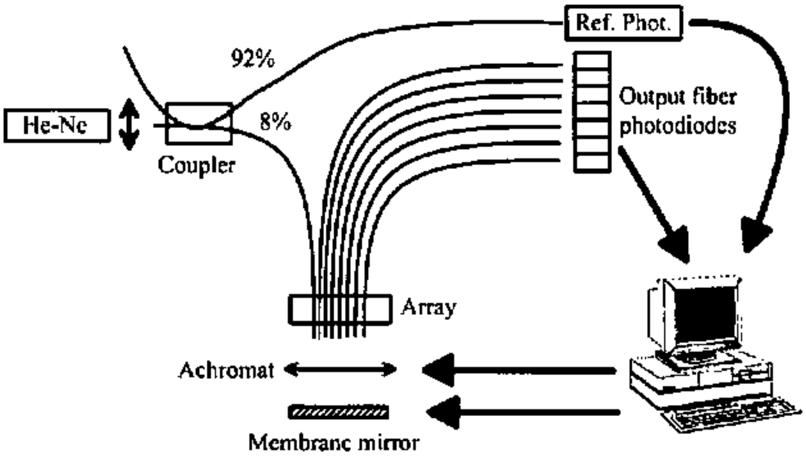

Figure 5.6: Experimental set-up of the switching system

The experimental set-up is schematically shown in Fig. 5.6. The light emitted from an He-Ne laser (λ = 633 nm) is coupled into a single-mode fiber using an aspheric lens. A

92%/8% coupler splits the signal into a reference fiber and a source fiber. The source fiber is part of a linear array of 32 single-mode fibers. The 32 fibers are held in a commercially available silicon V-groove array. The distance between adjacent fiber cores is 250 μm ± 0.5μm. The single-mode fibers have a cut-off wavelength of 590 nm. The mode field diameter is $2w_s = 4.5$ μm, corresponding to a core diameter of 3.8 μm and a numerical aperture of $NA_{fiber} = 0.11$. The cladding diameter is 125 μm. The fiber array is then 8 mm long. The fibers are parallel within $\pm 0.1°$. The linear array of fibers is placed in the front focal plane of the lens, whereas the membrane mirror is placed in the back focal plane. The lens is a commercially available doublet achromat of focal length $f = 40$ mm with an anti reflective coating (reflectivity $< 0.3\%$). Switching from the the source fiber to any of the 31 receiver fibers is possible by moving the achromat laterally using a precision x-y stage with a resolution of about 0.14 μm. The signals from the receiver fiber and the reference fiber are detected with calibrated silicon photodiodes. The ratio of the receiver and reference signal gives the coupling efficiency. We use the linear array of fibers with the source fiber at one end. It demonstrates the feasibility of a system which is twice as large with symmetric displacement of the achromat. The array of 32 fibers can therefore demonstrate the feasibility of a 1 ×62 one dimensional system. Moreover, a two dimensional array of fibers can be switched if the achromat is displaced in both x and y directions. The linear array of 32 fibers can thus demonstrate the feasibility of a 1 × 3019 two dimensional system.

Figure 5.7: Photograph of the breadboard of the free space optical fiber switch.

A photograph of the main part of the breadboard is shown in Fig. 5.7. We see the deformable membrane mirror the achromat lens moved by its 2 step motors and the array of fibers. The membrane mirror is aluminum coated and has an active diameter of 12 mm. A detailed description of the mirror is given in chapter 3. The membrane mirror used in the experiment had a substantial initial astigmatism, as shown in Figure 5.9. The reflectivity at 633 nm is 87%. The total loss due to the optical elements is estimated to be 22% by considering two interfaces between the receiver fiber and air, with 4% Fresnel losses each, 1% transmission loss inside the achromat and 0.3% of reflectivity at both surface and the reflectivity of the membrane mirror.

5.2.3 Results

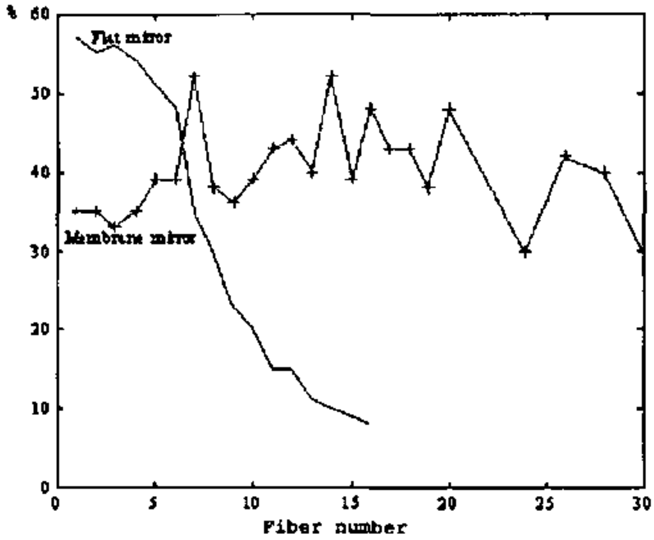

Figure 5.8: Measured coupling efficiencies vs. fiber number (input fiber number 1).

For the optimization of the shape of the membrane mirror for maximum power coupling of each connection we used the evolutionary algorithm based on the Zernike modes as described in Sec. 5.1.2.2. In general after 10 iterations the optimization has converged (see Fig. 5.4). The important parameters to get good convergence are the amount of mutations, as well as the number of modes used. 15 to 20 modes are enough for the optimization. If less than 15 modes are used, the optimization is not optimal. With more than 20 modes, the algorithm gets slower without a significant improvement of the result. It is not astonishing that the number of useful modes is in 15-20 range, as it corresponds to the aberrations up to the fifth order (secondary aberrations). Each connection has its own optimized deformation which can be memorized, storing the voltage applied on each electrode and the position of the lens. With these preset values the optimized membrane mirror deformation can be recalled for later connection to the same receiver fiber. Figure 5.8 shows the coupling efficiency of our system using the deformable mirror, compared to the same system with a conventional flat mirror. The experimental results for the flat mirror follow quite well the theoretical curve obtained by simulation with a ray tracing program (ZEMAX), taking into account the estimated 14% loss due to the optical elements. The coupling efficiency is less than 40% beyond number 7. For comparison, the optimized power coupling efficiency using the deformable mirror is between 29% and 52 % and the average coupling efficiency over all fibers is 39%. The coupling efficiency shows no fading with increasing fiber number.

Figure 5.9: Interference pattern of the membrane mirror at rest

The difference between the maximum theoretical coupling efficiency (78%) and the measured ones (52%) can be explained with the large initial astigmatism at rest, shown in Fig. 5.9 due to residual stress in the membrane. Simulations show that an astigmatism of $\lambda/5$ leads to a decrease of the coupling efficiency by 50%. The measured deviation of the membrane mirror from the perfect plane at rest is about 3 to 4 wavelengths. 4 wavelengths correspond to a quarter of the membrane deflection capability. Although the membrane mirror has the potential to correct its own imperfections, this limits the ability to further correct the system aberrations.

We verified also the calibration concept for the system. We optimized the coupling efficiency for fiber number 15 and stored the corresponding electrode voltages of the membrane mirror. Coming back to the same position after addressing other fibers, we got with the stored values for the electrode voltages the same coupling efficiency as before, which proves the reproductibility of the membrane mirror.

5.2.4 Conclusion

We have shown that a deformable membrane mirror can correct the aberrations of an optical switching system. The average measured coupling efficiencies for the connections up to the 31^{th} receiver fiber of a one dimensional system is 39% (including the 22% losses due to the optical components). Compared to an optical system without correction of the aberrations, the system with the deformable membrane mirror is better for connections beyond fiber number 7 (see Fig. 5.8). We have demonstrated the feasibility of a one dimensional 1×31 optical fiber switch, which corresponds to a two dimensional 1×3019 fiber system. The limit is given by the size of the achromat and its lateral displacement required for the switching. A larger achromat (with a larger focal length) and a larger deformable membrane mirror should be able to address more fibers. The correction of the aberrations was limited in our experiments by the residual stress of the membrane. In Ch.

3, we have seen that membrane mirrors with less than one wavelength of aberrations can be obtained.

5.3 Pumping of double clad fiber amplifiers

The first fiber amplifiers have been developed in the mid eighties and were doped with Erbium to amplify the optical communication wavelength of 1.5 μm. The only way to get high power after the amplification is by the use of double clad fiber, first presented in 1988 [84]. They are now used on many applications such as high power laser amplifiers, ultrafast lasers, laser guide stars or free space communications. The main difference between a monomode fiber and a double clad fiber is the refractive index of the coating of the fiber, as shown in Fig. 5.10. If the refractive index of the outer coating is lower than the cladding, this cladding can act as a multi-mode guide for the pump power.

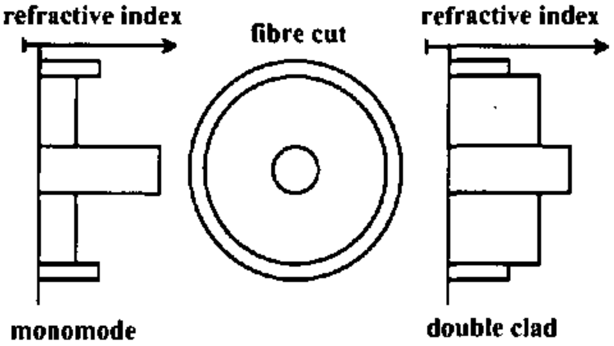

Figure 5.10: Difference of refractive index between a classical and a double clad fiber.

The monomode core of the fiber is doped with a rare earth element. In our experiments we have chosen Neodymium and Ytterbium. We demonstrate the optimization of the coupling of diode pump lasers into double clad fiber amplifiers. We first started with a medium power diode laser pumping an Ytterbium doped fiber before coupling a high power diode laser into a Neodymium doped fiber.

5.3.1 Pump coupling into Ytterbium doped fiber

We demonstrate the increase of efficiency in the coupling of the diode pump laser into an Ytterbium doped fiber. We propose two types of coupling, side coupling and front coupling. For the front coupling we were able to demonstrate that the optimization for a maximum of coupled pump light and the optimization for a maximum of fluorescence are different. We developed a breadboard for both types of coupling.

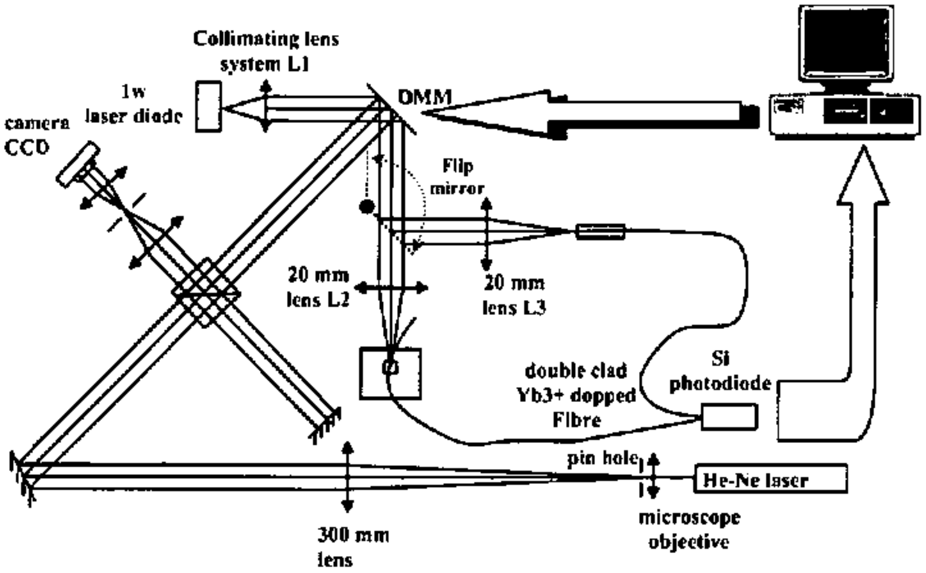

Figure 5.11: Diagram of the breadboard for the Ytterbium fiber coupling

5.3.1.1 The breadboard

The diagram shown in the Fig. 5.11 shows the breadboard for the Ytterbium fiber. The doped fiber has a cladding diameter of 125 μm and a core diameter of 4 μm. The length of the fiber was 4 m for the front coupling and 20 cm for the side coupling. The fiber was doped at 1%. We developed a breadboard to demonstrate the capability to increase the coupling of a diode laser with a highly divergent beam into a double clad fiber doped with Ytterbium. The diode laser emits 1 W at a wavelength of 980 nm. The beam has a divergence of ±30 degrees and ±5 degrees in two orthogonal directions. The laser is roughly collimated with an optical system L1 composed of a cylindrical lens and an aspheric lens. The laser is reflected at 90° by an aluminum coated membrane mirror. Depending on the position of the flip mirror, the laser is directed to the front coupling set-up or to the side coupling set-up. For the front coupling set-up an achromat lens L2 with a focal length of 20 mm is used to couple the light into the double clad Ytterbium fiber. A spectrometer at the output of the fiber filters the fluorescence of the Yb^{+3} at 1064 nm ±3 nm. The side coupling set-up is composed of the achromat lens L3 of focal length 20 mm to focus the light on the prism. The doped fiber is positioned under the prism with a few millimeter of coating removed as shown in Fig. 5.12. An index matching oil is used to obtain the contact between the prism and the fiber. The prism is a right angle silica prism and the laser beam has an angle of incidence of 24 degrees with respect to the surface normal of the prism.

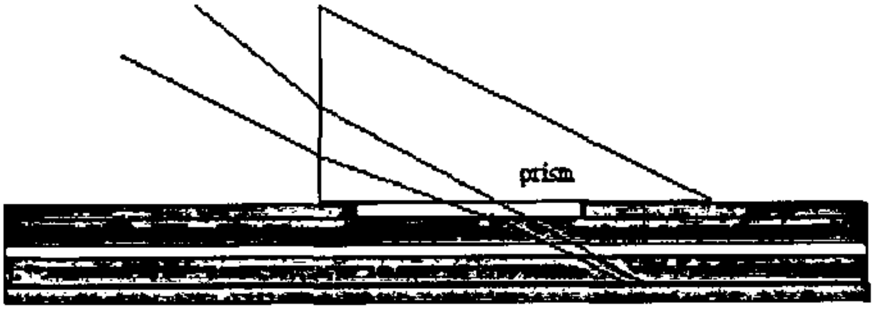

Figure 5.12: Cross-section diagram of the side coupling

5.3.1.2 Results

Side coupling: The coupling was low. It was not possible to measure the fluorescence reasonably well. Therefore we only concentrated on the optimization of the coupling efficiency. The best coupling efficiency obtained before the optimization was 12%. We were able to obtain after optimization a coupling efficiency of 17%, which represents a relative improvement of 42%.

Front coupling: We first investigated the fluorescence. We obtained an optimization of the fluorescence intensity of 48% comparing the intensity before and after optimization. In Fig. 5.13, we show the deformation of the membrane mirror calculated from the electrode voltages and the Zernike coefficients describing this deformation.

Once the above measurement made, we did cut the fiber to a length of 20 cm, which limits the absorption of the laser pump into the fiber. Before optimization we obtained a coupling efficiency of 39%, after the modulation we obtained 54%, which represents a relative increase of 38%. The deformation of the membrane for this optimization and the corresponding Zernike coefficients are shown in Fig. 5.14.

Comparing Figs. 5.13(a) and 5.14(a) we see that the deformations are significantly different for the two types of optimization. We can explain it by the followings considerations: to obtain a maximum of fluorescence the pump needs to cross as often as possible the core of the fiber, which is not necessarily the same condition as for maximum pump light coupling into the outer cladding.

5.3.2 Pump coupling into Neodymium doped fiber

A space borne fiber amplifier for coherent inter-satellite communication using Neodymium doped fiber has been designed by Rochat [75][74]. An important problem of this system is the efficient coupling of the light from the high power diode pump laser module into the double-clad doped fiber. This kind of fiber, which can be used as an amplifier or a laser,

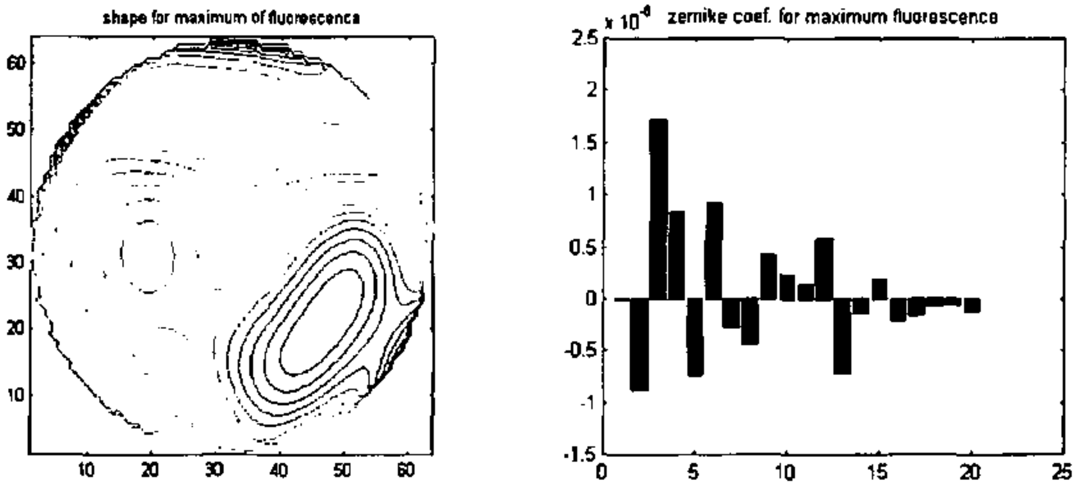

(a)

(b)

Figure 5.13: Membrane mirror shape for maximum fluorescence: (a) contour plot of the deformation, (b) Zernike coefficients.

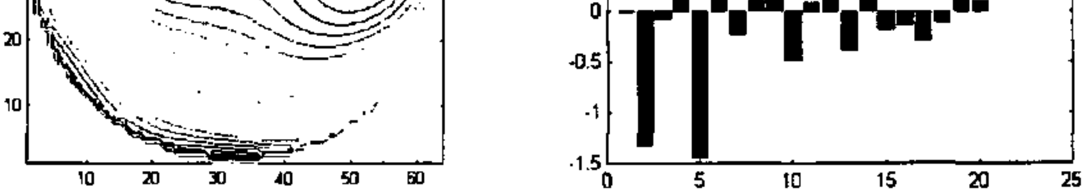

(a) 2D view

(b) Zernike coefficients

Figure 5.14: Membrane mirror shape for maximum pump light coupling: (a) contour plot, (b) Zernike coefficients.

is well explained in [51] and [62]. We propose to correct the shape of the focal point from the diode laser to increase the coupling efficiency by the use of adaptive optics.

5.3.2.1 Concept

An optical power of at least 1W is needed for an optical satellite to satellite coherent communication. A master oscillator power amplifier (MOPA) structure has been chosen to reduce the size of the optical system[2]. The master oscillator is a Nd:YAG laser from Lightwave Technology with a maximum power of 100 mW at a wavelength of 1064 nm and the amplifier is a double clad Nd-doped fiber. A diode laser module of 23 W is used to pump the fiber. The maximum coupling efficiency of the laser pump module into the double clad fiber is 29% with a classical front coupling. Under these conditions, a saturated output power of 1.3 W was obtained with an input power of at least 10 mW [75]. Any improvement of the pump coupling would increase the output power. We propose to use a membrane mirror to improve the pump coupling efficiency.

5.3.2.2 Breadboard

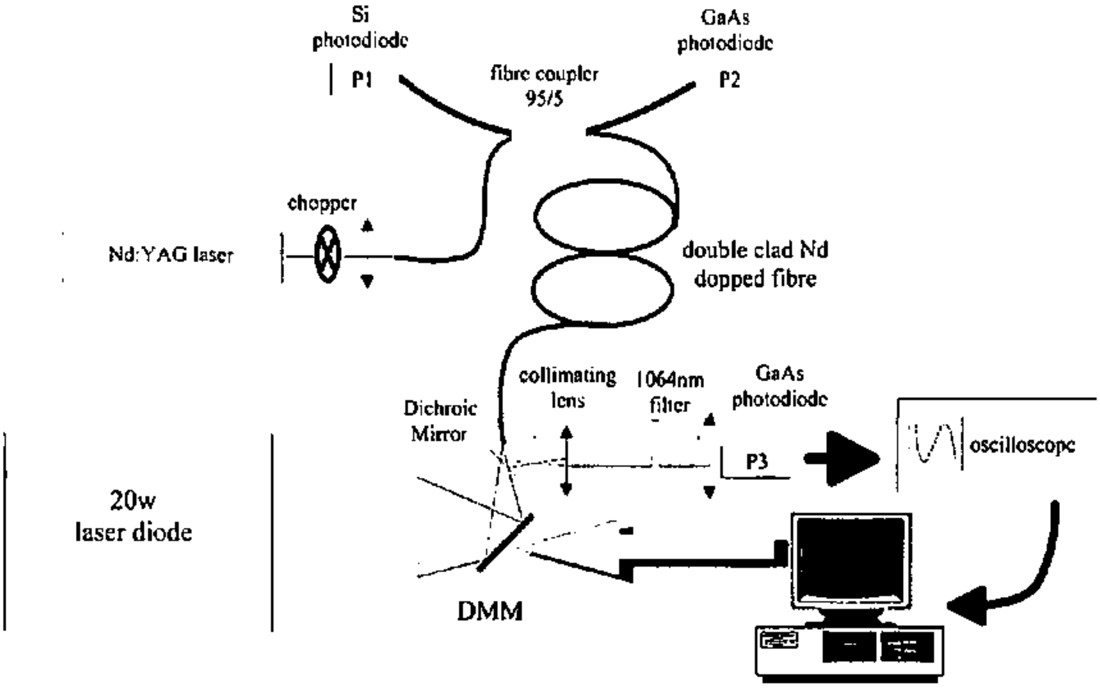

Figure 5.15: Design of the breadboard for the dynamic pump coupling into the Nd-doped fiber amplifier.

The design of the breadboard is given in Fig. 5.15. The double-clad Nd-doped fiber is the central part of the breadboard. It is backward pumped. The signal to be amplified is

---

[2] In space, the size, weight and consumption is of main importance.

coupled into the monomode core of the doped fiber from one side of the fiber by the use of a 95/5 fiber coupler. The pump light is coupled with the help of the deformable mirror into the multimode core of the doped fiber from the other side of the fiber. The pump is counter propagating the signal in the doped fiber. The pump and the signal are separated with a dichroic mirror.

The pump absorption band of Neodymium doped fiber is around 805 nm. We are concerned with the laser transition at 1.06 μm. The fiber is 12 m long in a rolled kidney shape. The fiber was produced by the Institut für Physikalische Hochtechnologie at Jena. Its characteristics are given in Table 5.1.

	IPHT 45 SK 3
core ⌀	4 μm
Cladding ⌀	200 μm
NA core	0.19
NA cladding	0.4
Pump attenuation (800 nm)	750 dB/m
Signal loss (1064 nm)	0.58 dB/m
Nd (weight)	1.7%
Lifetime	270 ms

Table 5.1: Characteristics of the Nd doped double clad fiber

The diode pump laser module is a DL-20 produced by FISBA OPTIK. Its characteristics are given in the Table 5.2. The multi-mode diode pump laser is coupled into the multimode core of the double-clad fiber. The diode laser module output is used with a lens system of 55 mm of focal length. Its spot size is 200 μm×300 μm oval shaped.

type	GaAlAs
Max. power output	23 W
Wavelength	805.4 nm
mode	multimode
output	CW

Table 5.2: Characteristics of the diode pump laser

The characteristics of the Nd:YAG master laser are given in Table 5.3.

The membrane mirror was the one shown in Fig. 3.2 with a silver coated membrane. It has 37 hexagonally disposed electrodes and a diameter of 15 mm. It is disposed at 45 degrees in the path of the pump beam. The dichroic mirror separates the pump from the amplified signal. The 95%/5% fiber coupler is used to transmit the signal into the doped fiber and to monitor the remaining output power of the pump at the far end of the doped fiber.

Type	Nd:YAG
wavelength	1064 nm
Linewidth	5 kHz
power	100 mW
mode	TEM_{00}

Table 5.3: Characteristics of the Nd-YAG master laser

5.3.2.3 Experiments

(a) (b)

Figure 5.16: (a) Pump coupling part of the optical system. (b) Reflection of the laser pump light on the membrane mirror.

Figure 5.16 shows the main parts of the adaptive optical system, which is the coupling of the pump into the doped fiber and the intensity pattern of the diode pump light reflected on the membrane mirror. The membrane mirror was specially made for very high reflection (more than 99.9%) at the wavelength of the diode pump laser to support the 25 W of pump power, but had a very small deflection capability of only 3 μm. This deflection was sufficient to demonstrate a change on intensity of the fluorescence when the mirror is modulated, but did not allow to optimize the coupling. Thus, to prove the optimization capability of the system, we decided to use a classical membrane mirror with a small output power of the diode pump (less than 1 W) and with a short length (1 m) of double clad fiber. This experiment gave us the ability to demonstrate the optimization of coupling of the FISBA diode laser module into the double clad doped fiber, but the fluorescence output was to small to allow optimization of the gain.

The genetic algorithm working on the electrodes (see Section 5.1.2.2) had been used for this purpose. The 15 mm diameter membrane mirror coated with aluminum has a deflection capability of 9 μm. After optimization, we only obtained an increase of the coupling efficiency of around 7%, which means a coupling efficiency of 37%. This proves that we have a possibility to optimize the coupling but that we need a mirror with larger capability for correction. We think that the newly made mirrors of 25 mm diameter and a deflection capability of 20 to 30 μm could give the expected results. The deflection produced by the mirror is shown in Fig. 5.17. The Zernike coefficients of the deflection show that the coefficients of main importance are the defocus, the spherical aberration and astigmatism. The main aberration is the defocus and we tried to correct it with a better alignment, but without success.

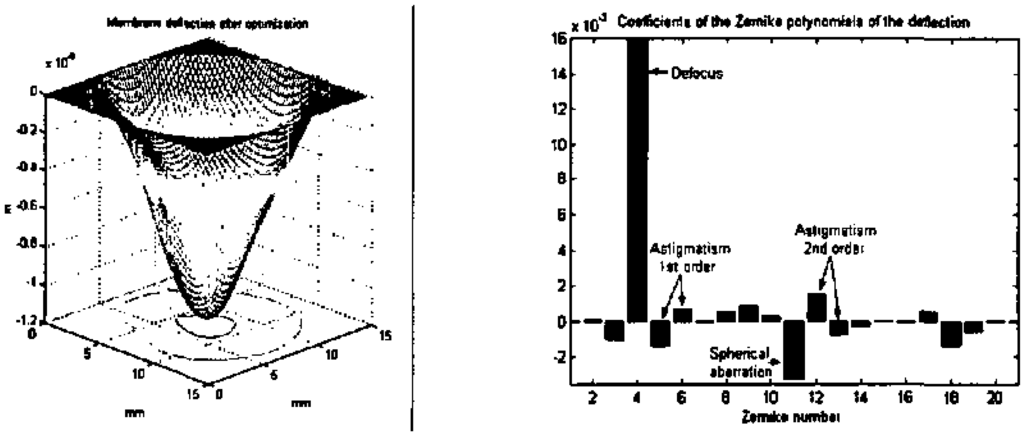

(a) (b)

Figure 5.17: Deflection of the membrane mirror from its bias position(a) and the corresponding Zernike coefficients (b).

5.4 Conclusion

We investigated the use of the membrane mirror in a closed-loop system to optimize the coupling of light into different kinds of fibers. We first started with the coupling of a laser beam into a single-mode fiber to determine the efficiency of the two optimization algorithms used in the closed loop system. The first kind of algorithm scans the voltage on the electrodes to determine the best optimization. The second is an evolutionary algorithm following the neo-Darwinian paradigm, which is reproduction, mutation, competition, selection. Each membrane deformation is considered as an individual and the corresponding set of electrode voltages is the genetic code. We have demonstrated, that we can obtain an improvement of the coupling by a factor of 2.2.

The first application in which we applied this optimization system is a telecom fiber switch. Its is composed of an array of fibers, a lens and the membrane mirror. One fiber of the array is used as the input fiber, the light is collimated by the lens, reflected by the membrane mirror and then refocused into an other fiber, depending on the off-axis position of the lens. We successfully developed a 1D array fiber switch of 32 fibers, which is equivalent to a 2D fiber switch of more than 3000 fibers.

The second application is the optimization of the pumping of fiber amplifiers. For the demonstration of this application, we used two types of double clad doped fiber amplifiers, The first one was an Ytterbium doped fiber and the second one was a Neodymium doped fiber. We tried to optimize the coupling of a diode laser of 1 W for the Ytterbium doped fiber and in the case of front coupling and side coupling. We obtained optimization for both types of coupling. We demonstrated, using the front coupling, that the result is different for the optimization of the fluorescence and for the maximum coupling of pump power into the cladding. We also tried to optimize the coupling of a diode laser array of 23 W into a Neodymium doped double-clad fiber amplifier. We have demonstrated for this case, that an optimization was achievable but we could not obtain an improvement of more than a few per cent, because of the limits of the membrane mirror. With a larger membrane mirror, having a greater deflection capability, we can expect better results.

Chapter 6

Phase multiplexing of volume holograms

"If a diffraction diagram of an object is taken with coherent illumination, and a coherent background is added to the diffracted wave, the photograph will contain the full information on the modifications which the illuminating wave has suffered in traversing the object. Moreover, the object can be reconstructed from this diagram without calculation. One has only to remove the object, and to illuminate the photograph by the coherent background alone. The wave emerging from the photograph will contain as a component a reconstruction of the original wave, which appears to issue from the object." Dennis Gabor (1900-1979).

The discovery of the hologram[1] principle by Gabor in 1948 [23], by trying to improve electron microscopy, gave the capability to record both phase and intensity of an optical wave. The availability of monochromatic light with the development of the laser in Ruby by Maiman in 1960 [55] and the He-Ne laser by Javan and Bennet the same year gave a boost to this research. The first volume holograms have been written in 1963 in alkali halides [96]. The photorefractive effect has been discovered by considering the optical damage in $LiNbO_3$ and $LiTaO_3$ under laser radiation of 515 nm and 633 nm in 1966 [4]. It gave tbe possibility to demonstrate the holographic storage in photorefractive crystals two years later [11]. The first multiplexing technique has been demonstrated in 1974 [15] and in 1975 [86] by choosing different angles of recording for each hologram. We had to wait fifteen more years for the demonstration of orthogonal phase-coded multiplexing [16][17]. Three main techniques have been developed to record several holograms in the same volume: wavelength multiplexing [110], angle multiplexing [2][63], and phase-coded multiplexing [18][102]. We propose to record data by holographic writing in a photorefractive crystal with a new phase multiplexing technique. The deformable membrane mirror is used to produce Zernike mode deformations with each deformation being the address of one specific

---

[1] Hologram means "total recording".

hologram. We have chosen an Iron-doped Lithium Niobate crystal as recording element for its highly valuable photorefractive property. A review of the theory concerning the optical wave transmission in Lithium Niobate crystal and the recording of multiplexed Fourier holograms will be presented. The set-up will be detailed and the results with the Zernike phase multiplexing presented.

6.1 Volume holograms

The idea and the theory of storing optical information in a three-dimensional media has been first proposed by P.J. van Herdeen [96]. The proposed solid are alkali halide crystal and the information was recorded by optical bleaching[2]. He demonstrated the capability of multiplexing holograms, calculated the maximum information storage capability of such system and found $\frac{V}{\lambda^3}$,which means using visible light between 1 to 10 terabits/cm^3. In our context the holograms are recorded in Iron doped Lithium Niobate. First we will give the main characteristics of the Iron doped Lithium Niobate crystal, then we will explain the propagation of optical wave in this media. Next we will explain the transfer of electrons under illumination producing the photorefractive effect inside the crystal, and the creation of the grating in the crystal with the help of the two-wave mixing theory.

6.1.1 Iron doped Lithium Niobate crystal

The characteristics of the Iron-doped Lithium Niobate crystal used for this experiment are given in the Table 6.1. A more detailed description of $LiNbO_3$ crystals is given in [44]. This crystal is a ferroelectric material. It has the advantage that the recorded information (holograms) can be read without processing. The Fe creates photosensitive electron traps. The change of refractive index comes from the spatial redistribution of electrons in the traps:

$$Fe^{2+} \underset{h\nu}{\rightarrow} Fe^{3+} + e^- \tag{6.1}$$

The occupied traps are Fe^{2+}, and the $Fe^{3+}$are the empty traps. The absorption band in the visible region of Fe^{2+}corresponds to the excitation of the trapped electrons in the conduction band. Under non-uniform illumination, a corresponding pattern of free electrons is generated, which induces a pattern of modified refractive index.

The theoretical limit of the storage capacity of $LiNbO_3$ is given in [109] and is

---

[2] The effect of optical bleaching is to bring sufficient energy in a crystal to free an electron from its trap produced by a missing ion. The release of the electron to the valence band produces a change of color in the crystal which is called bleaching.

Crystal structure	Trigonal, space group R3C (uniaxial)
Cell parameters	a = 0.5148, c = 13.863, Z = 6
Refractive index (at 633 nm)	$n_0 = 2.286$ $n_e = 2.200$
Melting point	1526 Kelvin
Curie point	1411 Kelvin
Mosh Hardness	5
Density	4.64g/cm^3
Solubility	insoluble in H_2O
Composition	Congruent or stoichiometric
Iron level	0.015 mol%
Orientation	C-cut
Size	10×10×7 mm^3

Table 6.1: Characteristics of the Fe:LiNbO$_3$

$$C = \frac{16\pi}{3} n_e^2 n_0 \frac{V_{crystal}}{\lambda^3}, \tag{6.2}$$

where λ is the wavelength, n_e is the extraordinary refractive index ,n_0 is the ordinary refractive index, and $V_{crystal}$ is the volume. With $n_e = 2.29$, $n_0 = 2.2$, $V_{crystal} = 10 \times 10 \times 7$ mm^3, and $\lambda = 488$ nm we get $C = 1.16 \cdot 10^{15}$ bit.

6.1.2 Photorefractive effect

The photorefractive effect is a change in the index of refraction of a medium proportional to the light intensity. The display of an intensity pattern in a photorefractive material will produce an equivalent refractive index pattern. The interference of two optical beams create an intensity pattern, which is a hologram if recorded in adequate materials and conditions. The evidence of the photorefractive effect in crystals has been discovered in 1966 by Ashkin et al. [4] and presented as an optical damage to the crystal. In 1968 Chen et al. [11] demonstrated the first holographic recording in such a crystal. The photorefractive effect is a linear electro-optic effect, also called Pockels effect after its discoverer[3]. The Pockels coefficients form a tensor of third rank. This tensor has several symmetries, so that it can be reduce to a 6×3 matrix as explained in [106]. For LiNbO$_3$, the representation is:

---

[3] Friedrich Pockels (1865-1913) demonstrated this effect in 1893.

$$r_{ij} = \begin{bmatrix} 0 & -r_{22} & r_{13} \\ 0 & r_{22} & r_{13} \\ 0 & 0 & r_{33} \\ 0 & r_{51} & 0 \\ r_{51} & 0 & 0 \\ -r_{22} & 0 & 0 \end{bmatrix} \tag{6.3}$$

We consider that the electric field created by the transfer of charge is quasi-static (for more precision see [105]). The values of the coefficients given in $10^{-12}m/V$ are $r_{13} = 9.6$, $r_{22} = 6.8$, $r_{33} = 30.9$ and $r_{51} = 32.6$.

Considering a sinusoidal grating, the index variation for the extraordinary wave is given by [37]

$$\Delta n = -\frac{1}{2} n_e^3 r_{33} E_{sc} cos(Kz) \tag{6.4}$$

where E_{sc} is the space charge field and $K/2\pi$ is the spatial frequency of the grating. It depends on the intensity of the two beams, of the density of the donor and acceptor impurities, and of the temperature of the crystal [107][37]. Typically in Lithium Niobate crystal the space charge field has a value of around $E_{sc} = 1 \cdot 10^5$ V/m. Witb $r_{33} = 30.9 \cdot 10^{-12}m/V$ and $n_e = 2.2$, we obtain a maximum refractive index variation of $\Delta n = -1.65 \cdot 10^{-5}$.

6.1.3 Recording and reading out volume holograms

We have now to explain the grating formation in Lithium Niobate crystal due to the interference of two optical waves and the reading of this hologram due to the diffraction of the reference beam on the grating. The behavior of the optical wave propagation in the Iron doped Lithium Niobate crystal is described by the Maxwell's equations. They are given in [8]. The Iron doped Lithium Niobate crystal is a uniaxial crystal, therefore the wave propagation is given by two indices of refraction, related to the extraordinary and ordinary polarization of the wave. A good description of the transmission of an optical wave in such media is given in [106]. As we will only use the extraordinary polarization in our experiment, we will only consider the transmission of a plane wave with the refractive index of the extraordinary polarization. The hologram read out can been described by the coupled wave theories for volume holograms ([96], [42] ,[24], [46]).

We will describe here the theory which corresponds best to the conditions of our experiment explained in Section 6.3. This theory is based on 2-wave mixing in anisotropic media and is explained in detail in [108]. but we take only account of the extraordinary polarization. With this simplification the electric filed can be written as

$$\mathbf{E} = A\mathbf{p} \cdot \exp\left(-i\mathbf{k}_a \cdot \mathbf{r}\right) + B\mathbf{p} \cdot \exp\left(-i\mathbf{k}_b \cdot \mathbf{r}\right) \tag{6.5}$$

where A and B are the complex amplitudes of the two waves, $\mathbf{p}$ is the polarization, and $\mathbf{k}_a$ and $\mathbf{k}_b$ are the wave vector of the two beams, As shown in Fig. 6.1(a) two beams create by interference the index grating

$$\Delta n = a \cdot AB^{\star} \exp\left(-i\mathbf{K} \cdot \mathbf{r}\right) / I_0, \tag{6.6}$$

where a is a constant containing several factors, such as the refractive index and the electro-optic coefficients implied in the grating. I_0 is the total intensity and $\mathbf{K} = \mathbf{k}_a - \mathbf{k}_b$ is the grating vector. The period of the fringe pattern is

$$\Lambda = \frac{2\pi}{|\mathbf{K}|}. \tag{6.7}$$

In our experiment the plane of incidence of the two beams is parallel to the c-axis of the crystal, therefore the extraordinary mode is parallel to the plane of incidence.

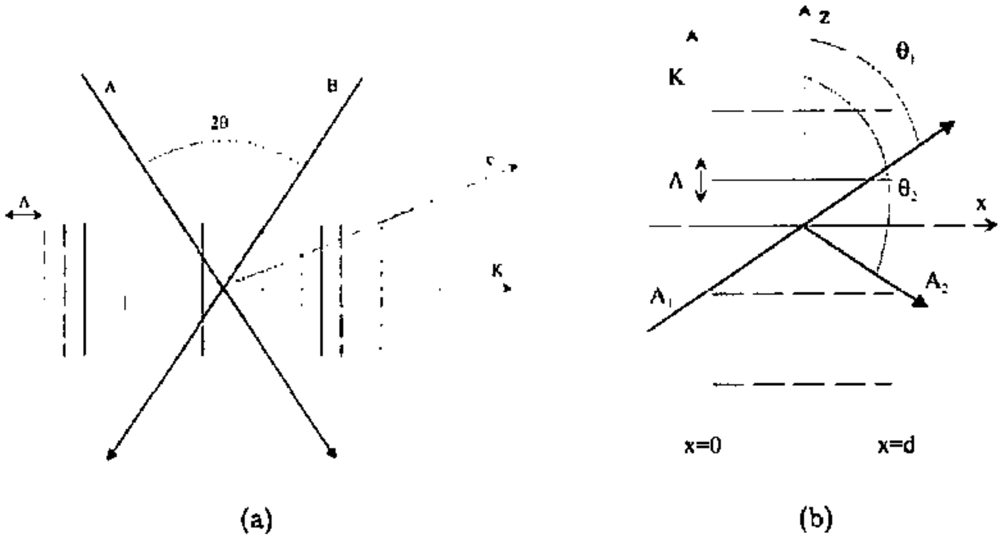

(a) (b)

Figure 6.1: (a) Volume grating produced by two plane wave A and B in Fe:LiNbO$_3$, (b) read-out of the hologram.

To read-out the hologram, the beam A will be used and will diffract on the volume grating produced by the interference. To create a new beam as shown in the Fig. 6.1(b). A_1 is the reference beam. A_2 is the diffracted beam and is equivalent to B as long as we are in the Bragg conditions. The behavior of these two beams has been described precisely in 1969 by Kogelnik [42].

6.2 Phase multiplexing

Up to now we have explained how to write one hologram in a photorefractive crystal, but we are interested in writing several independent holograms. To do so it is necessary to give a specific address to each recorded hologram. This can be done by several techniques known as angular, wavelength and phase multiplexing. A good overview of these techniques is given in [35] and [1].

The angular multiplexing technique was the first which had been explored to multiplex volume holograms. The principle is to write each hologram with a different angle by slightly rotating the recording media or changing the angle of the reference beam. The angles are the addresses of the recorded pictures and each picture can be read-out with its corresponding angle. In the mid seventies it was already possible to write more than an hundred holograms by reference beam deflection[15] or by recording media rotation[86].

Wavelength multiplexing uses slightly different wavelengths to record the hologram. This technique has been applied to a photorefractive crystal for the first time in 1991 by [112]. Typically a tunable diode laser is used to get the different wavelengths [110]. A hybrid system using both wavelength and angular multiplexing has also been proposed [10].

6.2.1 Phase-coded multiplexing

Phase-coded multiplexing system is used since ten years to record holograms in photorefractive material. This technique is based on the fact that, when reading a hologram with a particular address, the reconstructions of the other holograms interfere destructively to produce zero intensity. The theory concerning the phase-encoding technique is well explained by Denz et al. in [17]. We will only give a summary of the theory to be able to understand the proposed Zernike mode encoding technique. In [17], we find the following description.

"In this technique, each image is stored with N pure and deterministic binary reference beams. Each set of adjustable phases for these reference beams represents the address of one of the N stored images and is orthogonal with all other phase addresses. All reference beams overlap the image in the recording volume and interact independently with this image. Noiseless reconstruction appears because the reconstructions of the undesired images interfere destructively to produce zero intensity."

They consider that the references beams and the images are plane waves. The mth image beam is described by the complex amplitude

$$A_m = \frac{1}{2}\left[A_m \exp\left(i\mathbf{k} \times \mathbf{r}\right) + c.c\right], \tag{6.8}$$

where **k** and **r** are the wave vector and the position vector respectively. For the recording each image beam interferes with a set of N phase-modulated reference beams described by the complex amplitude

$$P_m = \frac{1}{2}\sum_{n=1}^{N}\left[P_0\exp\left(i\Phi_n^m\right)\exp\left(i\mathbf{k}_n\cdot\mathbf{r}\right) + c.c\right], \tag{6.9}$$

where the set of the phases $(\Phi_1^m, \Phi_2^m, \ldots.., \Phi_n^m)$ represents the address of the mth image. The corresponding refractive index variation of the recorded hologram is given by

$$\Delta n_m = \frac{N\cdot A_m P_0^*}{2\left(I_m + I_R\right)}\cdot\left\{\sum_{n=1}^{N}\delta n_n\exp\left[-i\left(\Phi_n^m + \Psi\right)\right]\cdot\exp\left[-i\left(\mathbf{k}-\mathbf{k}_n\right)\cdot\mathbf{r}\right] + c.c.\right\}, \tag{6.10}$$

where Ψ is the phase shift between the interference pattern and the refractive index grating, $I_m = \frac{A_m A_m^*}{2}$, $I_R = \frac{|P_0|^2}{2}$ and δn_n is the index modulation amplitude of the nth grating. Using the coupled-wave theory described by Kogelnik[42] we get for the amplitude R_m of the reconstruction from the multiplexed hologram with the reference P_m the differential equation

$$\frac{dR_m}{dz} = i\exp\left(i\Psi\right)\frac{\pi}{\lambda}\delta n P_0\sum_{m=1}^{M}\frac{A_m P_0^*}{\left(I_m + NI_0\right)}\cdot\sum_{n=1}^{N}\exp\left[i\left(\Phi_n^p - \Phi_n^m\right)\right]. \tag{6.11}$$

Therefore, to read-out a particular image m without cross-talk from the other images the the following condition have to be fulfilled:

$$\begin{aligned} &\textstyle\sum_{n=1}^{N}\exp\left[i\left(\Phi_n^p - \Phi_n^m\right)\right] = 0 \qquad p \neq m \\ &\textstyle\sum_{n=1}^{N}\exp\left[i\left(\Phi_n^p - \Phi_n^m\right)\right] = N \qquad p = m. \end{aligned} \tag{6.12}$$

These particular conditions can be obtained using the Walsh-Hadamard matrices as an orthonormal basis [38][33]. The reference is a set of beams with mutual phase difference of π corresponding to the Walsh-Hadamard matrices. A computer generated hologram is used to create the different reference beams and which encoded with the help of a transmissive liquid crystal display.

6.2.2 Zernike mode encoding

Our approach is to use a reference beam encoded with phase distributions corresponding to Zernike polynomials. As we have seen in Chapter 2, the Zernike polynomials are mutually orthogonal. We expect that the reconstructions of the holograms with different phase addresses will interfere destructively. In fact, for continuous phase distributions rather than discrete phase coding the conditions given by conditions (6.12) have to be rewritten as

$$\begin{aligned} &\textstyle\int_0^1\int_0^{2\pi}\exp\left[i\left(\Phi_p\left(\rho,\theta\right) - \Phi_m\left(\rho,\theta\right)\right)\right]\rho d\rho d\theta = 0 \qquad p \neq m \\ &\textstyle\int_0^1\int_0^{2\pi}\exp\left[i\left(\Phi_p\left(\rho,\theta\right) - \Phi_m\left(\rho,\theta\right)\right)\right]\rho d\rho d\theta = 1 \qquad p = m, \end{aligned} \tag{6.13}$$

where Φ_p and Φ_m are the wavefronts of the Zernike polynomials used to encode the different images. If we use single Zernike modes for the encoding , the integral in conditions (6.13) becomes

$$C_{pm} = \frac{1}{2\pi} \int_0^1 \int_0^{2\pi} \exp i \left[a_p Z_p(\rho, \theta) - a_m Z_m(\rho, \theta) \right] \rho d\rho d\theta. \tag{6.14}$$

where a_p and a_m are the amplitudes of the corresponding Zernike modes. The value of $|C_{pm}|^2$ can be considered as the coefficient of correlation , or cross-talk between different phase codings. We understand that there is no general solution to solve these integrals, but we will discuss some particular cases.

6.2.2.1 Encoding with defocus of different amplitudes

We first consider the case of encoding with defocus of different amplitudes, The corresponding Zernike polynomial $Z(\rho, \theta)$ is found from Table 2.3. From Eq. 6.14 we get

$$\int_0^1 \int_0^{2\pi} \exp\left(i \left[a_p \sqrt{3} \left(2\rho^2 - 1 \right) - a_m \sqrt{3} \left(2\rho^2 - 1 \right) \right] \right) \rho d\rho d\theta. \tag{6.15}$$

The integral can be separated in ρ and θ, and the integration ρ can be solved using the substitution $u = i \left[(a_p - a_m) \sqrt{3} \left(2\rho^2 - 1 \right) \right]$. The final result is

$$C_{pm} = \frac{\sin \left[4\sqrt{3} \left(a_p - a_m \right) \right]}{\left[4\sqrt{3} \left(a_p - a_m \right) \right]}, \tag{6.16}$$

Which is known as the sinc function. The value of the cross-talk coefficient $|C_{pm}|^2$ as a function of difference $(a_p - a_m)$ is shown in Fig. 6.2.

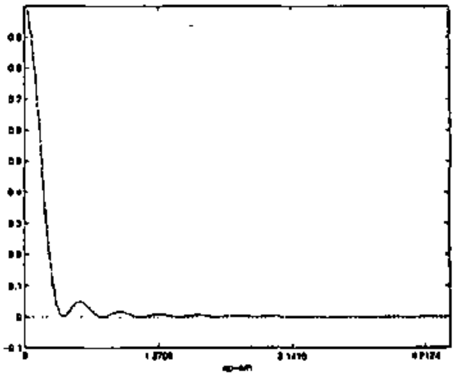

Figure 6.2: Value of $|C_{pm}|^2$ for the defocus case.

6.2.2.2 Encoding with tilt

We will check the case of a coupling with a difference of amplitude between a tilt and the reference phase. It is given by

$$C_{pm} = \frac{1}{2\pi}\int_0^1\int_0^{2\pi} \exp\left(i\left[a_p\rho\cos\theta\right]\right)\rho d\rho d\theta \tag{6.17}$$

It is better to rewrite the Eq. (6.17) in Cartesian coordinate with the integration over a pupil where $x = \rho\cos\theta$ and $y = \rho\sin\theta$, we then obtain

$$C_{pm} = \int_{-1}^{1} dy \int_{-\sqrt{1-y^2}}^{\sqrt{1-y^2}} \exp\left(i\left[a_p x\right]\right) dx. \tag{6.18}$$

From Eq. (6.18) We can simplify to obtain

$$C_{pm} = \int_{-1}^{1} dy \frac{\sin\left[a_p\sqrt{1-y^2}\right]}{a_p}. \tag{6.19}$$

The result of Eq. (6.19) can be obtained numerically and is given in Fig. 6.3

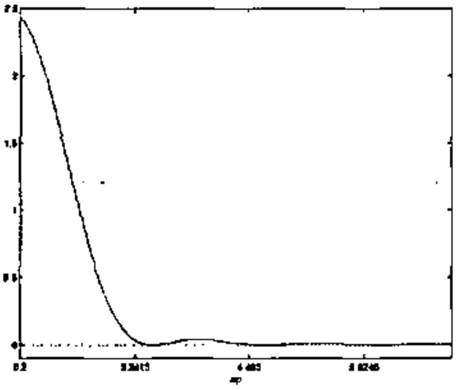

Figure 6.3: Value of $|C_{pm}|^2$ for the tilt case.

6.2.2.3 Coupling between tip and tilt

We will check now the case of a coupling between tip and tilt given in Eq. (6.20).

$$C_{pm} = \frac{1}{2\pi}\int_0^1\int_0^{2\pi} \exp\left(i\left[a_p\rho\cos\theta - a_m\rho\sin\theta\right]\right)\rho d\rho d\theta, \tag{6.20}$$

where a_p is the amplitude of the tip and a_m is the amplitude for the tilt. It is better to rewrite the Eq. (6.20) in Cartesian coordinate and to make an estimation over a quadratic aperture we then obtain

$$C_{pm} = \frac{1}{4}\int_{-1}^{1}\int_{-1}^{1} \exp\left(i\left[a_p x - a_m y\right]\right) dxdy.$$

Once solved

$$C_{pm} = \frac{1}{4}\frac{\sin(a_p)}{a_p}\frac{\sin(a_m)}{a_m}.$$

We recognize that the value of $|C_{pm}|^2$ goes toward zero as soon as a_p and a_m increase.

6.3 Breadboard demonstrator

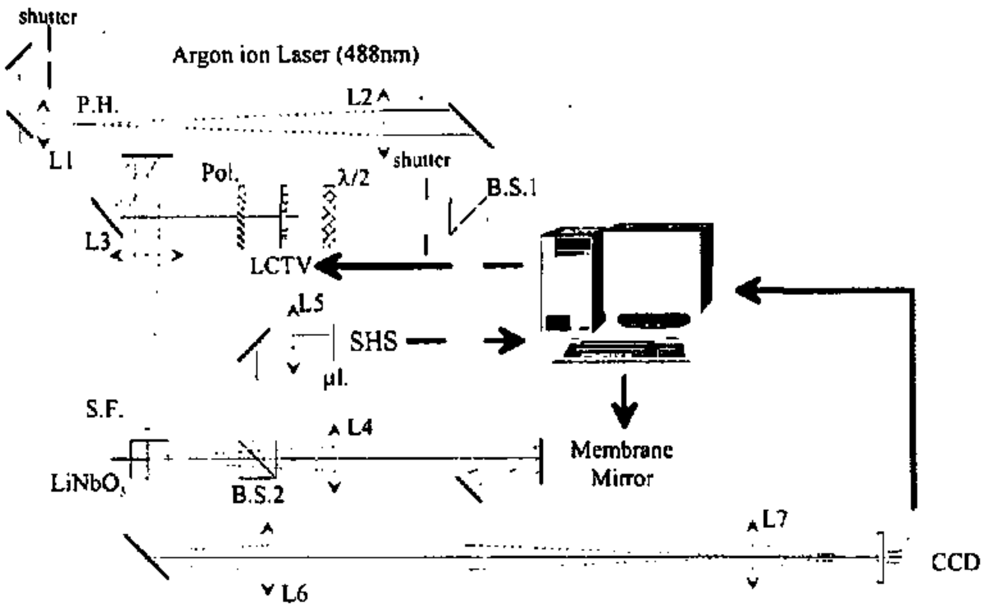

Figure 6.4: Diagram of the phase multiplexing breadboard

The diagram of the phase multiplexing breadboard is shown in Fig. 6.4. The principle of the set up is as follows: an argon ion laser produces a linear polarized beam at 488nm, which is expanded by the microscope objective L1 of magnitude 15 and filtered with a pinhole of 15 μm diameter and collimated by the achromat lens L2 of 300 mm focal length. The beam is split in two identical parts by the beam splitter B.S.1 to obtain the signal arm and the reference arm of the hologram recording set-up. The polarization in the signal arm is rotated by 90° with a $\lambda/2$ plate and encoded with a liquid crystal display. The signal is filtered with a polarizer to transmit only the extraordinary polarization. The lens L3 of 200 mm focal length is used to obtain the Fourier transform of the signal. A spatial filter is set just in front of the Lithium Niobate crystal to keep only the zero order of the signal. The reference arm is first reflected on the membrane mirror, then it is focused by the lens L4 of 300 mm focal length in the direction of the photorefractive crystal. The beam splitter B.S.2 sends 4% of the reference beam to the Shack-Hartmann sensor. The lenses L4 and L5 of 100 mm focal length form a Keplerian telescope [101] to reduce the diameter of the reference beam to the size of the CCD of the Shack-Hartmann sensor (see Ch. 4). The Lithium Niobate crystal is installed at the intersection of the signal and reference beam to record the holograms. The lens L6 of 200 mm focal length produces the inverse Fourier transform of the hologram read-out and finally the lens L7 of 120 mm focal length images the read-out hologram on the high resolution CCD camera. A neutral density filter is placed in front of the camera to adjust the power below saturations.

6.3.1 The optical components of the breadboard

The Argon Ion laser is a Spectra-Physics model 165-08 Argon ion laser. The wavelength is 488 nm and the characteristics at this wavelength are given in Table 6.2.

wavelength	488 nm
mode	TEM_{00}
$\Delta\nu$	143 MHz
max output	1.3 Watt
polarization	linear

Table 6.2: Argon ion laser data

Although the maximum output power is 1.3 W, we have chosen to work at a power of around 150 mW, which is sufficient for the experiment. Assuming a Gaussian lineshape, the coherence length of the laser is given by

$$l_c = c \cdot \frac{\left(\frac{2 \cdot \ln 2}{\pi}\right)^{1/2}}{\Delta\nu}, \tag{6.21}$$

where $\Delta\nu$ is the spectral width of the laser and c is the speed of the light. For $\Delta\nu = 143$ MHz we obtain a coherence length of 1.4 m. Therefore a few centimeters of path difference between the two arms does not cause a problem.

All lenses are doublet achromats of 50 mm diameter. The deformable mirror used as a phase addressor for multiplexing the holograms is an aluminum coated membrane mirror with 37 electrodes produced by T.U. Delft, as described in Chapter 3. The Shack-Hartmann sensor described in Chapter 4 measures the wavefront of the reference beam produced by the membrane mirror.

Resolution	640 × 480 pixel
Display size	26.88 × 20.16 mm
Pixel pitch	42 × 42 μm
Pixel size	21.5 × 31.5 μm
Thickness	4.3 μm
Twist angle	G: -90°, R: 90°, B: 90°
Mode	Normally White
Δn	0.117
Response time	40 ms

Table 6.3: LCTV Data

The liquid crystal display and the driving electronics are from CRL OPTO[4]. The characteristics are given in the Table 6.3. A photograph of the liquid crystal display is shown in Fig. (6.5).

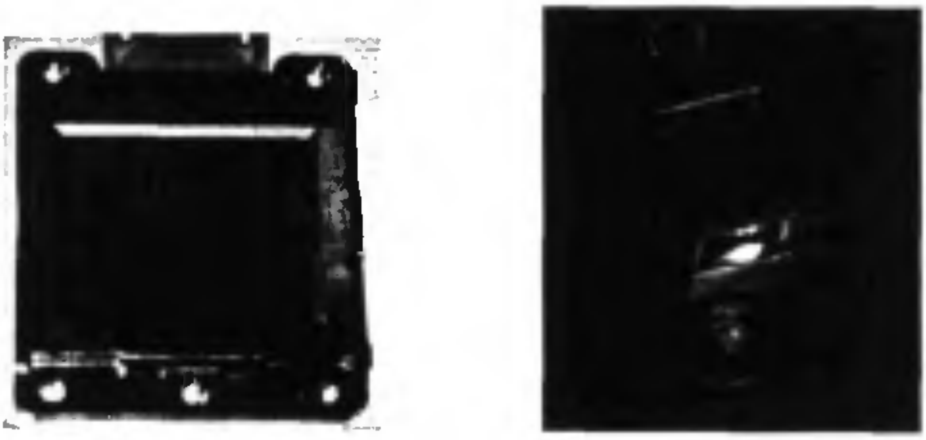
(a) LCTV

(b) Photorefractive crystal

Figure 6.5: Photographs of the LCTV (a) and the photorefractive crystal (b).

The recording material is a crystal of Iron doped Lithium Niobate, described in Section 6.1.1. A photograph of the crystal illuminated by the reference beam is shown in Fig. 6.5(b). The zero order spatial optical filter is a mask with a 2 mm hole centered on the zero order of the Fourier transform. It is used to eliminate the higher order diffraction from the LCTV pixel array. The CCD camera is a Hamamatsu C4742-95-12NRB. The Table 6.4 gives its main characteristics. The choice of a camera with a high spatial resolution has been made to simplify the detection of each pixel of the liquid crystal display. Each pixel of the liquid crystal display is imaged on 4 pixels of the CCD camera.

---

[4] www.crlopto.com

A/D converter	12 bit
Frame rate	8.3 Hz
Effective area	8.58 × 6.46 mm
Effective number of pixels	1280 × 1024
pixel size	6.45 × 6.45 μm
pixel clock rate	14.75 MHz/pixel
full well capacity	18,000 electrons
readout noise (r.m.s)	8 electrons
Dark current	0.1 electron/pixel/second

Table 6.4: Data of the Hamamatsu camera

6.3.2 Acquisition procedure

The computer is used to control the membrane mirror and the liquid crystal display, to record and treat the information from the Shack-Hartmann sensor, and to record the images captured by the CCD camera.

6.3.2.1 Recording Procedure

To record a hologram, we first start by closing both shutters, then a picture or an array of data is sent to the LCD and a specific deformation is applied to the membrane mirror. We open both shutters during a specific time, which allows the two beams to interfere in the photorefractive crystal. During that period we can also capture the signal picture with the CCD camera and analyse the deformation of the membrane mirror with the help of the Shack-Hartmann sensor. To end the recording we close both shutters.

To avoid a loss of diffraction efficiency of the recorded holograms and to obtain the same grating amplitude for multiplexed holograms, two techniques have been proposed: the sequential recording [87] and the incremental recording [88]. The incremental recording repeats several times the recording of all holograms with an exposure time which is much smaller than the time for maximum amplitude. In the sequential recording, each hologram is written once. In this case a specific recording time has to be used for each hologram. We have chosen the sequential recording for ease of use.

The recording time T_n for the hologram number n is given by

$$T_n = -\tau \ln\left(1 - \frac{1}{n+1}\right), \tag{6.22}$$

where τ is the time for writing a hologram with maximum amplitude. The times calculated for the 15 first holograms for τ=120 s are given in Tab. 6.5.

Hologram number	1	2	3	4	5	6	7	8	9	10	11	12	13	14	15
Writing time (s)	83	49	36	27	22	19	16	14	13	11	10	9	9	8	8

Table 6.5: Exposure time for recording 15 holograms

6.3.2.2 Read-out procedure

To read out a specific hologram we close the signal shutter and apply the corresponding deformation to the membrane mirror; the CCD camera captures the picture. To limit the erasure of the hologram during read-out, it is necessary to limit read-out time to less than one minute . With a frame rate of 8.3 Hz for the camera the read-out time for one image is 0.125 s.

6.4 Results

Or goal was to multiplex several holograms using the deformation capability of the membrane mirror to create different phase addresses for each hologram. Each phase address is determined by a specific Zernike mode as we believe that the orthogonality of these deformations will allow to make recording without cross-talk. We will first measure the quality of these Zernike mode deformations and select the ones which can be best used for multiplexing holograms.

6.4.1 Zernike mode deformations

In Chapter 3 we have determined by simulation the set of electrode voltages necessary to obtain the low order Zernike modes. The different deformations obtained with this simulations are shown in Appendix B. We produced each deformation up to the 15th mode at maximum amplitude and then measured the corresponding deformations with the Shack-Hartmann sensor. The complete set of results is shown in Appendix C. As examples are shown here in Figs. (6.6) to (6.8), defocus, tilt, coma first and second order astigmatism. As seen from Fig. 6.6, the defocus mode is nearly perfect, whereas tilt and coma (Fig. 6.7), and also first and second order astigmatism, have strong mutual interactions.

As a consequence, we have selected for the recording of the holograms, only modes which have a minimum of interactions namely; tip, tilt, defocus, 1^{st} order astigmatism, and trefoil.

6.4.2 Necessary minimum amplitudes

To determine the minimum necessary amplitudes for each Zernike mode to write holograms without crosstalk, we used two binary pictures shown in Fig. (6.9), the first contains a

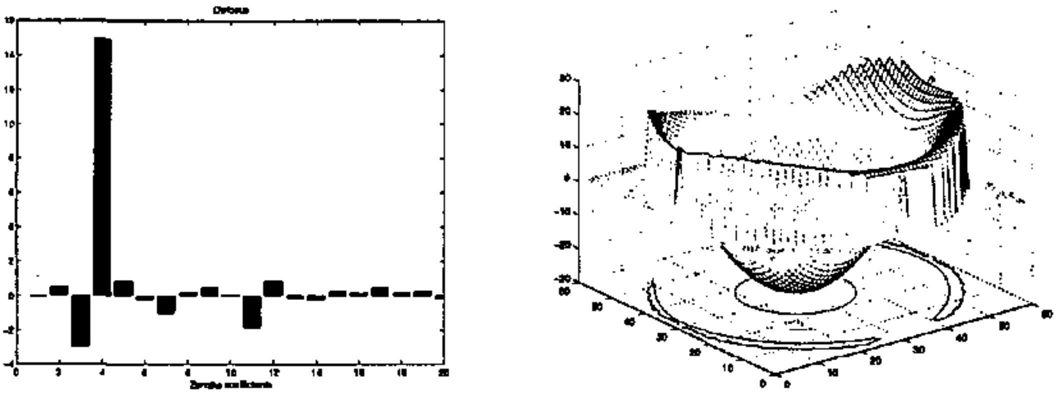

Figure 6.6: Measured defocus deformation and its restored shape

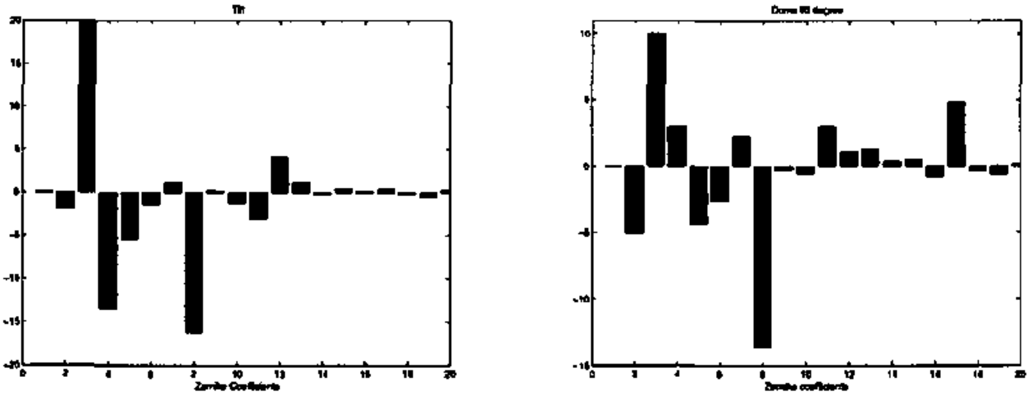

(a)

(b)

Figure 6.7: Measured tilt (a) and coma (b).

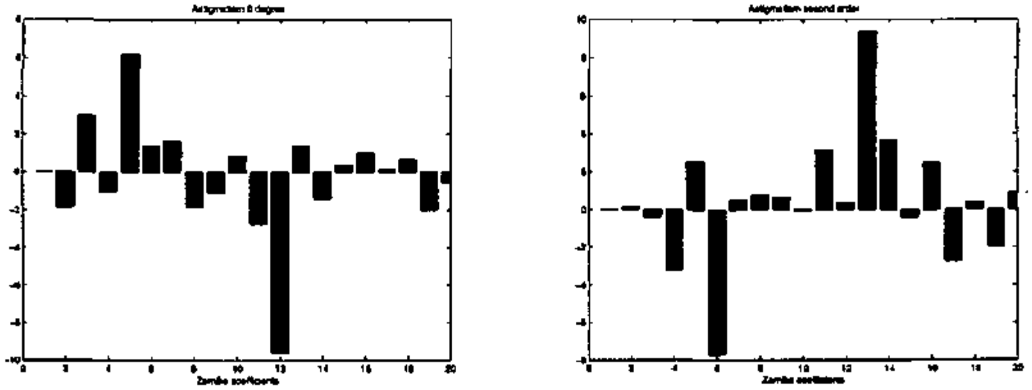

(a)

(b)

Figure 6.8: Measured astigmatism 1^{st} order (a) and astigmatism 2^{nd} order (b)

square on the left side and the second on the right side.

Figure 6.9: Original binary picture to measure cross-talk

To measure the cross-talk quantitatively, a first hologram is recorded with the first picture (left square) and the undiformed (biased) membrane mirror for the reference phase. Then, a second hologram is recorded with the second picture (right square) and a Zernike mode with a certain amplitude. Examples for read-out with and without cross-talk are shown in Fig. 6.10.

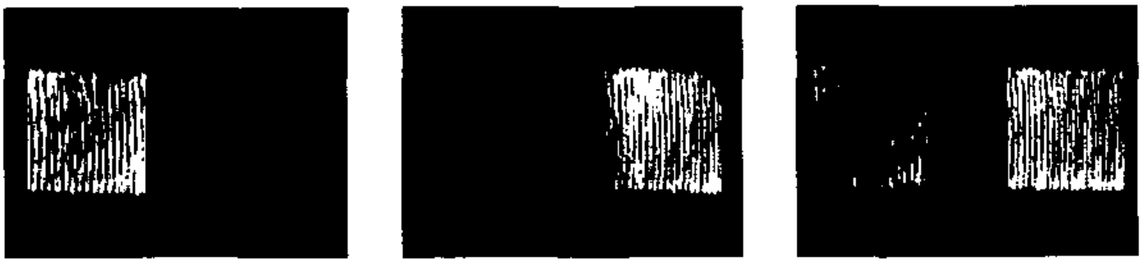

(a) (b) (c)

Figure 6.10: Read-out of the binary pictures: (a) and (b) without cross-talk, (c) with cross-talk.

The cross-talk is measured by taking the ratio of the intensity of the two squares in the reconstruction. The results of theses measurements for the low order modes, tilt, defocus, astigmatism, coma, trefoil, spherical aberration and quadrifoil are presented in Fig. (6.11). As we can see in Fig. (6.11), for all the modes, a cross-talk of less than 0.2 can be obtained, except for the quadrifoil. We see that each mode needs a different minimum amplitude to get a cross-talk below 0.2.

The phase distributions (wavefronts) corresponding to this minimal amplitudes have been investigated with the Michelson interferometer described in Chapter 3 (reference mirror of 2 m of focal length and He-Ne laser at 633 nm). The interferograms of the six good Zernike modes are shown in Fig. 6.12. The quadrifoil with full amplitude is shown in Appendix D (Fig. 1, picture 14 and 15). We observe on the interferograms that each mode has phase

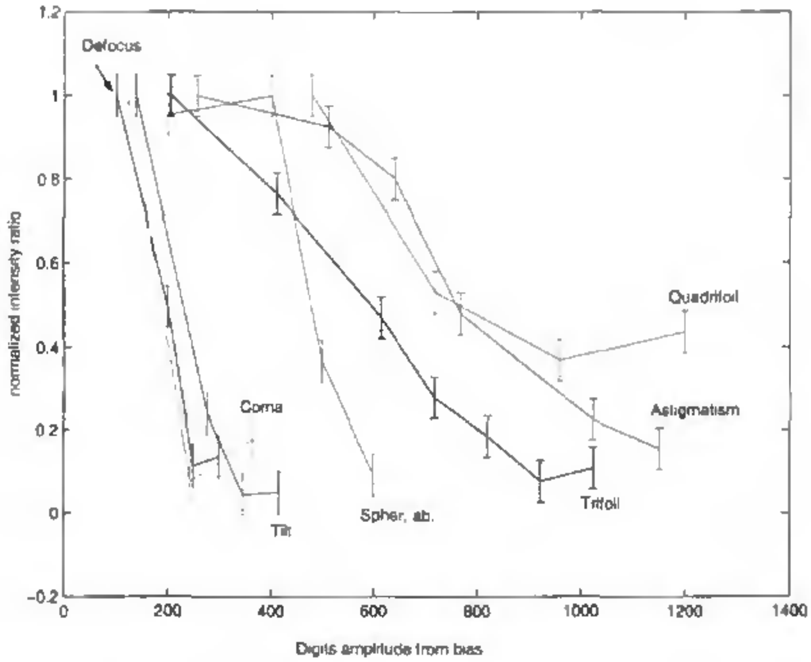

Figure 6.11: Cross-talk for different Zernike modes vs amplitude of the deformation (see Ch. 3)

variation between 2 and 3 wavelengths ($\lambda = 633$ nm). We see also that the undiformed (biased) mirror used for the reference recording has still some aberrations. This has not been corrected, because it is the same reference for all the encoding holograms.

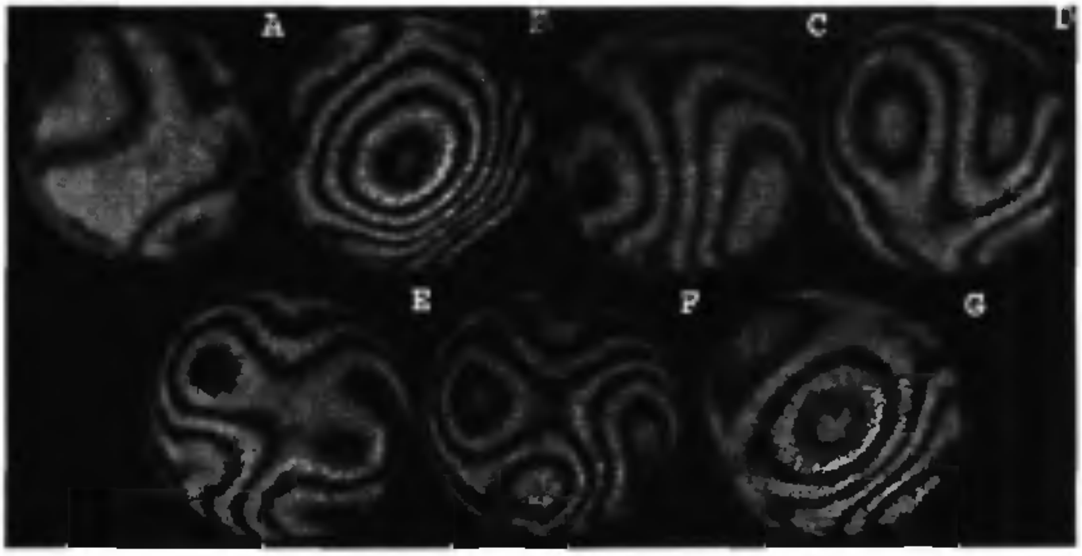

Figure 6.12: Interferograms of the Zernike modes with their minimal amplitude to record holograms without cross-talk: bias(A), defocus(B), tilt(C), coma(D), trefoil(E), astigmatism (F), spherical aberration(G).

6.4.3 Interactions of the modes

We have defined the necessary minimal amplitudes for the Zernike modes to obtain no cross-talk with respect to holograms recorded with the reference phase (bias). We now consider the cross-talk between holograms recorded with different Zernike modes at these minimal amplitudes. To measure the cross-talk we followed the same procedure as for the previous measurements (Sec. 6.4.2). We always measured the interaction between 2 holograms and we did it with the modes measured in Sec. 6.4.2, except the quadrifoil because we always obtained cross-talk with it. The employed modes are defocus, tilt, coma, spherical aberrations, trifoil, and astigmatism. On these 15 interactions, we noticed only one with cross-talk. This is the interaction between the tilt and the coma. The coupling expected from the measurements with the Shack-Hartmann sensor (Fig. 6.7) is confirmed here. We measured a cross-talk with an intensity ratio of around 0.5. The corresponding cross-talk observed in the reconstruction is shown in Fig. 6.13.

Figure 6.13: Cross-talk between tilt and coma

6.4.4 Zernike mode hologram multiplexing

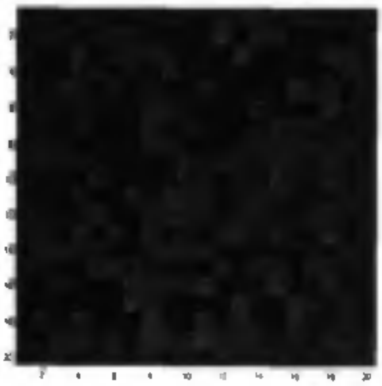

Figure 6.14: Typical binary matrix used for recording data

We attempted to multiplex several holograms with different Zernike modes. For this purpose we produced random binary matrices of 20×20 data, as shown in Fig. 6.14. We have been able to write up to 10 holograms without cross-talk by using for each hologram a different low order Zernike mode of the membrane mirror. The selected modes are: negative and positive tip, negative and positive tilt, negative and positive defocus, positive astigmatism at 0°, positive astigmatism at 45°, positive trefoil at 0°, positive trefoil at 30°. We have not used the coma, because of the observed cross-talk between coma and tilt. The Fig. (6.15) and (6.16) show the input patterns compared with the read-out of the corresponding holograms recorded with different modes as detected by the CCD camera. The reconstructed images have not been treated to improve the contrast.

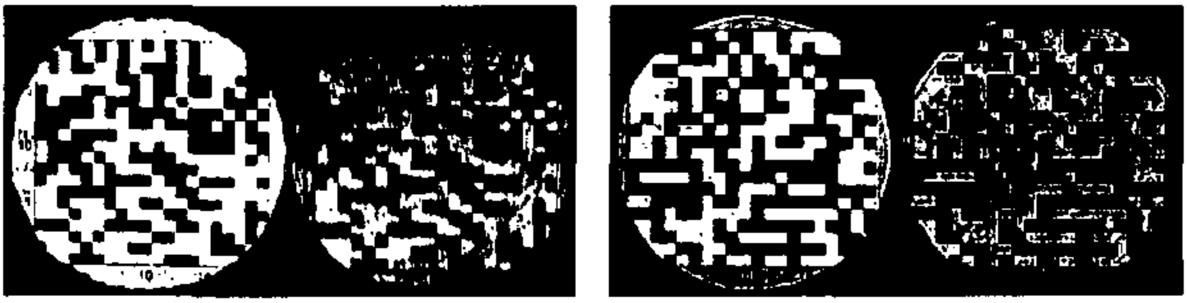

(a) (b)

Figure 6.15: Recording and reading-out of the data: (a) positive tilt, (b) negative defocus.

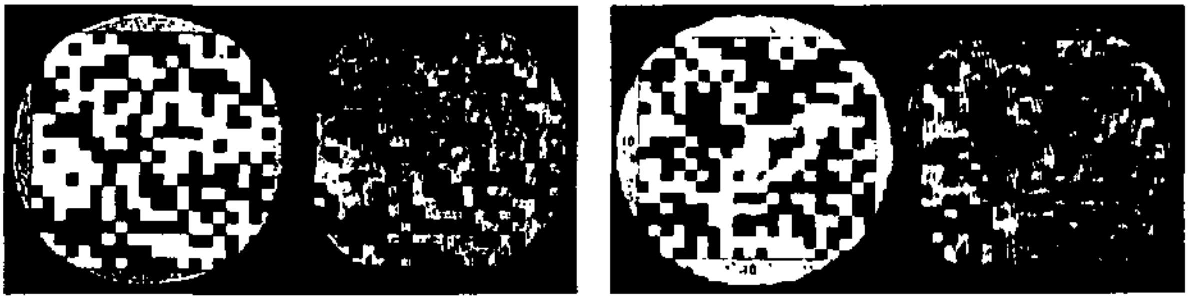

(a) (b)

Figure 6.16: Recording and reading-out of the data: (a) positive astigmatism 0°, (b) positive trefoil 30°.

6.4.5 Writing holograms with the same Zernike mode at different amplitudes

As we have seen that with the defocus only a small amplitude was needed to write holograms without cross-talk, we have decided to attempt to write several holograms with a different defocus amplitude. The membrane mirror has a maximum deflection capability of $\pm 3.8 \cdot 10^{-6}$ m with this mode as explained in Section 3.4.1. We have been able to write efficiently 8 holograms without cross-talk by changing the amplitude of the defocus from -2.85 μm to 3.8 μm by steps of 0.95 μm with the bias set at 0 μm.

6.5 Conclusion

A full phase multiplexing system has been set. The signal beam is encoded with the help of a liquid crystal display. The phase change of the reference beam to address each recorded hologram is made with the help of a deformable membrane mirror (see Chapter 3). A Shack-Hartmann sensor described in Chapter 4 has been added to the system to analyse the deformation of the membrane mirror. We have measured that only the defocus has a near perfect shape, when the other modes have strong interactions with at least on other mode.

We demonstrated the use of the membrane mirror to phase multiplex holograms in photorefractive crystal. We measured the minimum necessary amplitude for each low order mode to record holograms without crosstalk. We showed that it is possible to record several holograms with different Zernike modes produced by the membrane mirror and we have been able to record up to 10 holograms using low order Zernike modes. We have seen that the number of hologram to be recorded is limited by the deformation quality of the membrane mirror.

Chapter 7

Conclusion

> "*In the new setting of ideas the distinction [between particle and waves] has vanished, because it was discovered that all particles have also wave properties, and vice versa. Neither of the two concepts must be discarded, they must be amalgamated. Which aspect obstrudes itself depends not on the physical objects, but on the experimental device set up to examine it*" Erwin C. Schrödinger (1887-1961)

The objective of this work was to find and demonstrate new applications of optical wavefront modulation with micromachined deformable membrane mirrors. The membrane mirrors used for this purpose are fabricated at the Technical University of Delft. They are electrostatically activated by 37 electrodes and have an active diameter of less than 12 mm. We proposed 3 different applications, the two first are closed-loop systems and the last one is a novel holograms recording technique.

For both closed-loop systems we developed two optimization algorithms, The first algorithm is a classical maximization algorithm, the second is an evolutionary algorithm. They have been tested by trying to increase the coupling efficiency of a plane optical wavefront in a monomode fiber.

The first closed-loop system on which we applied these algorithms is a massive 1×N telecom fiber switch. This switch is composed of an array of fiber disposed in front of a lens and a deformable membrane mirror. The output signal of a fiber is collimated by the lens reflected by the membrane mirror and focalized by the same lens into an other fiber. This is the slight off-axis position of the lens which allows to couple into an other fiber. By changing the position of the lens, we couple the signal into the wanted fiber. The aberrations produced by the off-axis lens are corrected by the membrane mirror.

The second closed-loop system is dedicated to the optimization of laser pump coupling into double clad doped fibers. These types of fibers are used as laser amplifier. We developed two breadboards, the first one with an Ytterbium doped fiber and the second with a Neodymium doped fiber. With the first breadboard we demonstrated a strong increase of the pump coupling efficiency. We also demonstrated that the optimization of the fluorescence output and the pump coupling was different. With the second breadboard, where the Neodymium doped fiber is used in a MOPA system, the results have been limited by the deformation capability of the membrane mirror.

The third application is a novel phase multiplexing technique. Up to now to multiplex several holograms by phase change, the principal solution is by phase encoding technique. Each hologram is record with a specific superposed set of orthogonal reference phases produced by a liquid crystal display. Instead of the set of reference phases, we propose the use of a single reference beam, on which we apply a different phase for each hologram to be recorded. Each phase is a specific Zernike mode. The membrane mirror is used to produce these Zernike modes. With the help of a Shack-Hartmann sensor specifically designed for this purpose, we measured the quality of the Zernike modes which can be produced by the membrane mirror. After the selection of the best modes for the multiplexing, we measured the minimum necessary amplitude to do not obtain some cross-talk. We have been able to multiplex up to ten holograms with different modes, but we also multiplexed 8 holograms with the defocus mode and by changing its amplitude. The number of holograms to be multiplexed is limited by the deformation capability of the membrane mirror.

As we have seen the two last applications are limited by the capability of the deformable membrane mirror. T.U. Delft developed recently micromachined membrane deformable mirror with a diameter up to 50 mm and activated by 119 electrodes. A membrane mirror of 50 mm and activated by 39 electrodes has been recently tested to be used as a wavefront corrector for a large space telescope[58]. It would be interesting to test this type of mirror on the two last applications to observe the improvements.

About the Zernike mode multiplexing, we have seen that the number of holograms which can be recorded is highly dependent of the deformation quality of the mirror. A mirror with natural mode very close to the Zernike modes would be very useful. Also, it would be interesting to mix it with an other technique as the wavelength multiplexing or the angle multiplexing.

Chapter 8

Appendix

In the appendix are presented respectively the deformations for the twenty first Zernike modes, then in appendix B are shown the simulated deformations of the membrane mirror to reproduce the Zernike modes up to the fifteenth mode, and finally in appendix C is shown the measurement made with the Shack-Hartmann sensor of these deformations.

All the classifications are given following the Noll's classification.

8.1 Appendix A

The aberrations shape of the Zernike mode.

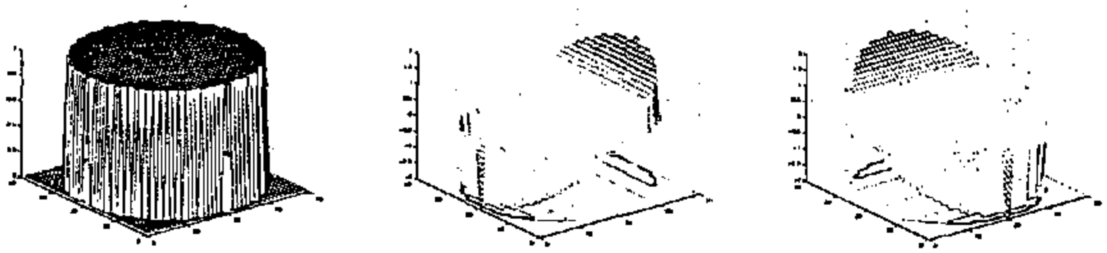

(a) mode 1 (b) mode 2 (c) mode 3

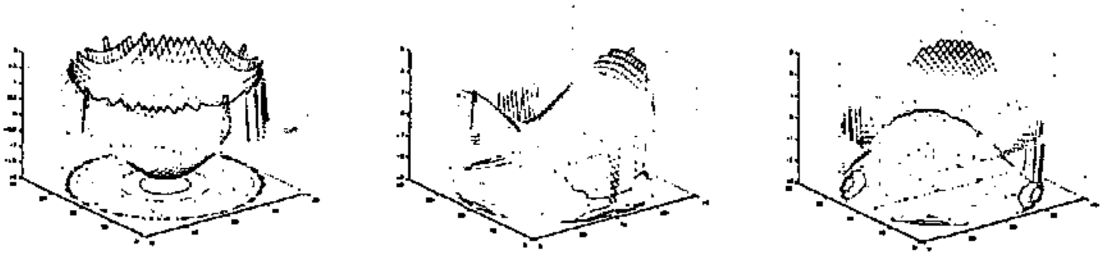

(d) mode 4 (e) mode 5 (f) mode 6

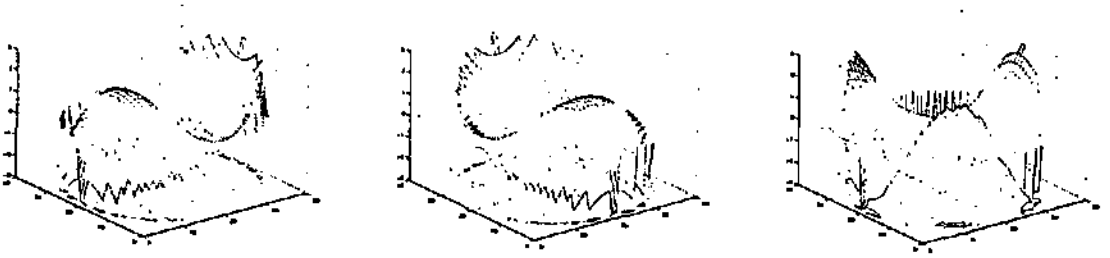

(g) mode 7 (h) mode 9 (i) mode 9

Figure 8.1: Zernike mode 1 to 9

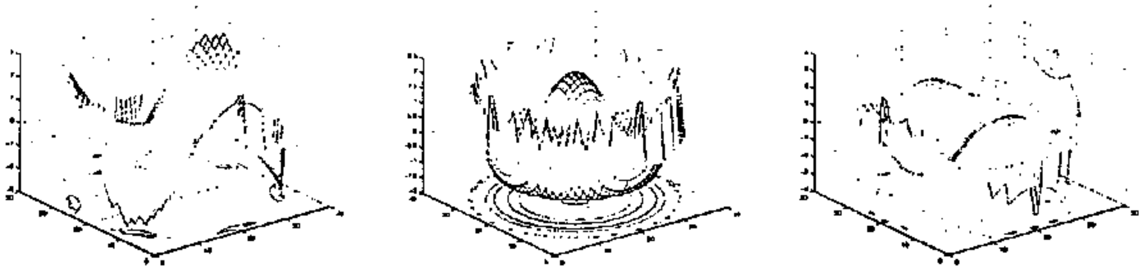

(a) mode 10 (b) mode 11 (c) mode 12

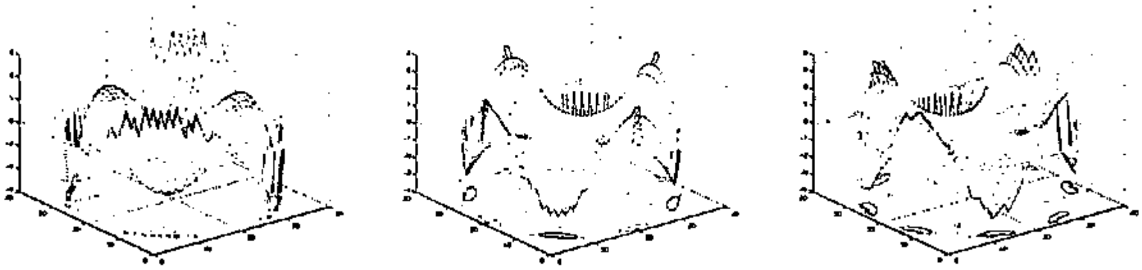

(d) mode 13 (e) mode 14 (f) mode 15

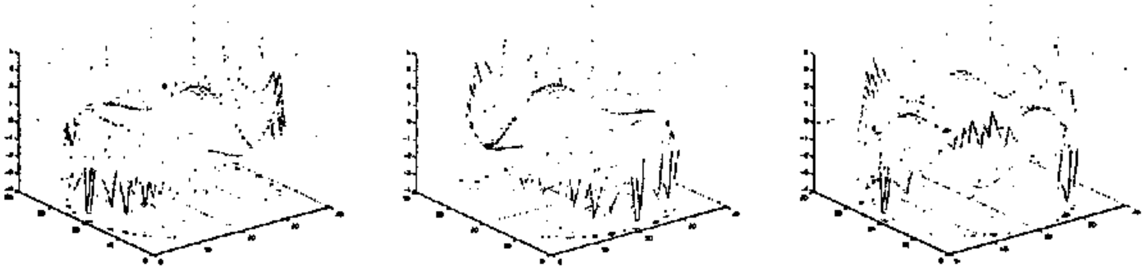

(g) mode 16 (h) mode 17 (i) mode 18

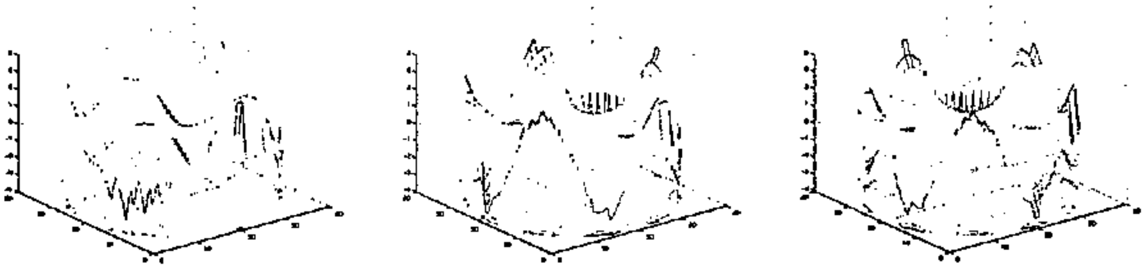

(j) mode 19 (k) mode 20 (l) mode 21

Figure 8.2: Zernike mode 10 to 21

8.2 Appendix B

We present in this appendix the simulated deformation to obtain the Zernike modes.

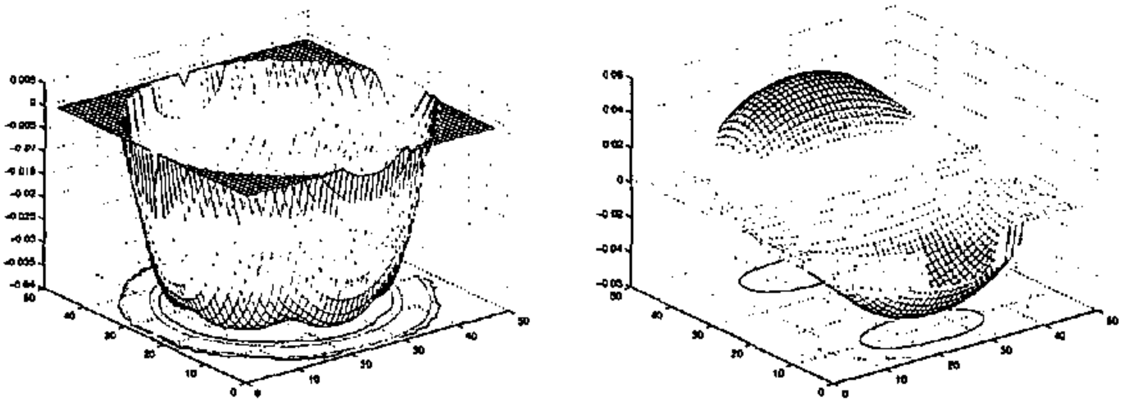

(a) mode 1

(b) mode 2

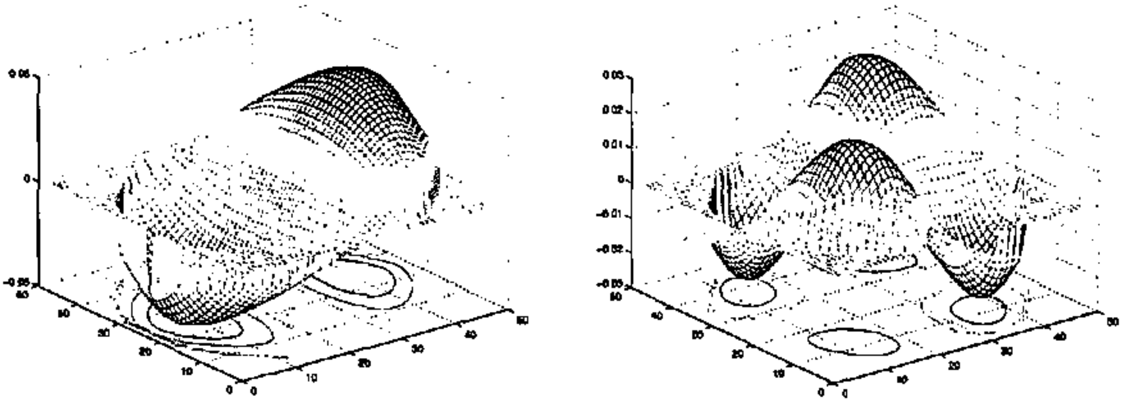

(c) mode 3

(d) mode 4

Figure 8.3: Zernike mode 1 to 4

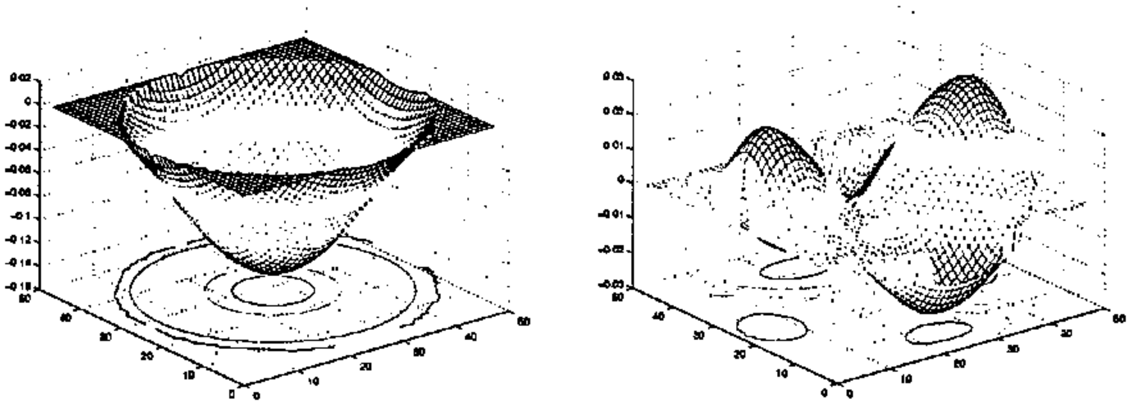

(a) mode 5

(b) mode 6

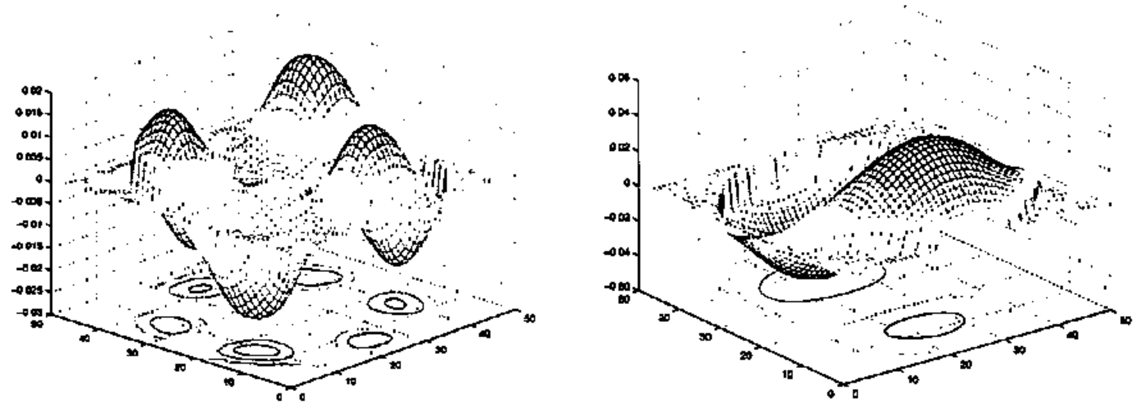

(c) mode 7

(d) mode 9

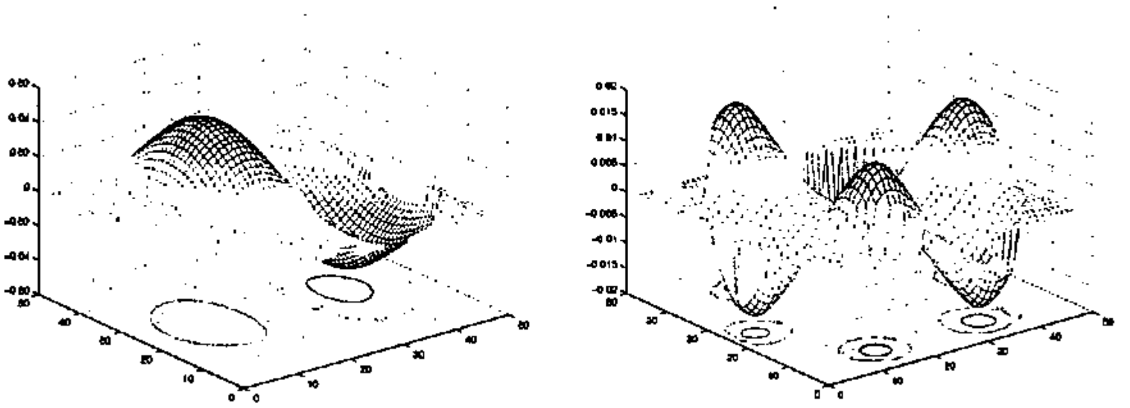

(e) mode 9

(f) mode 10

Figure 8.4: simulated Zernike mode 5 to 10

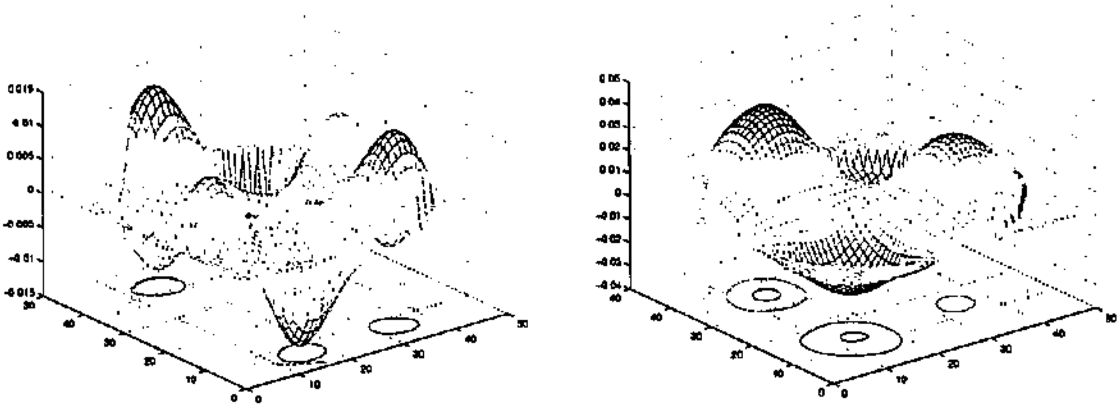

(a) mode 11

(b) mode 12

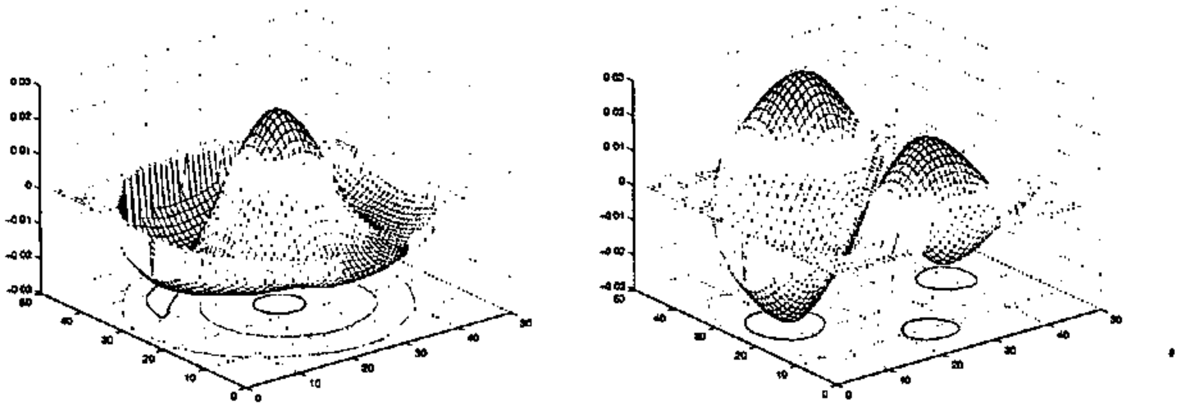

(c) mode 13

(d) mode 14

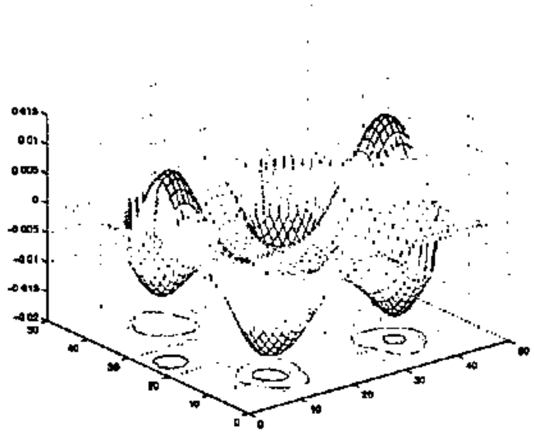

(e) mode 15

Figure 8.5: Zernike mode 11 to 15

8.3 Appendix C

We present in this appendix the measured deformations to obtain the Zernike modes up to the 4^{th} order.

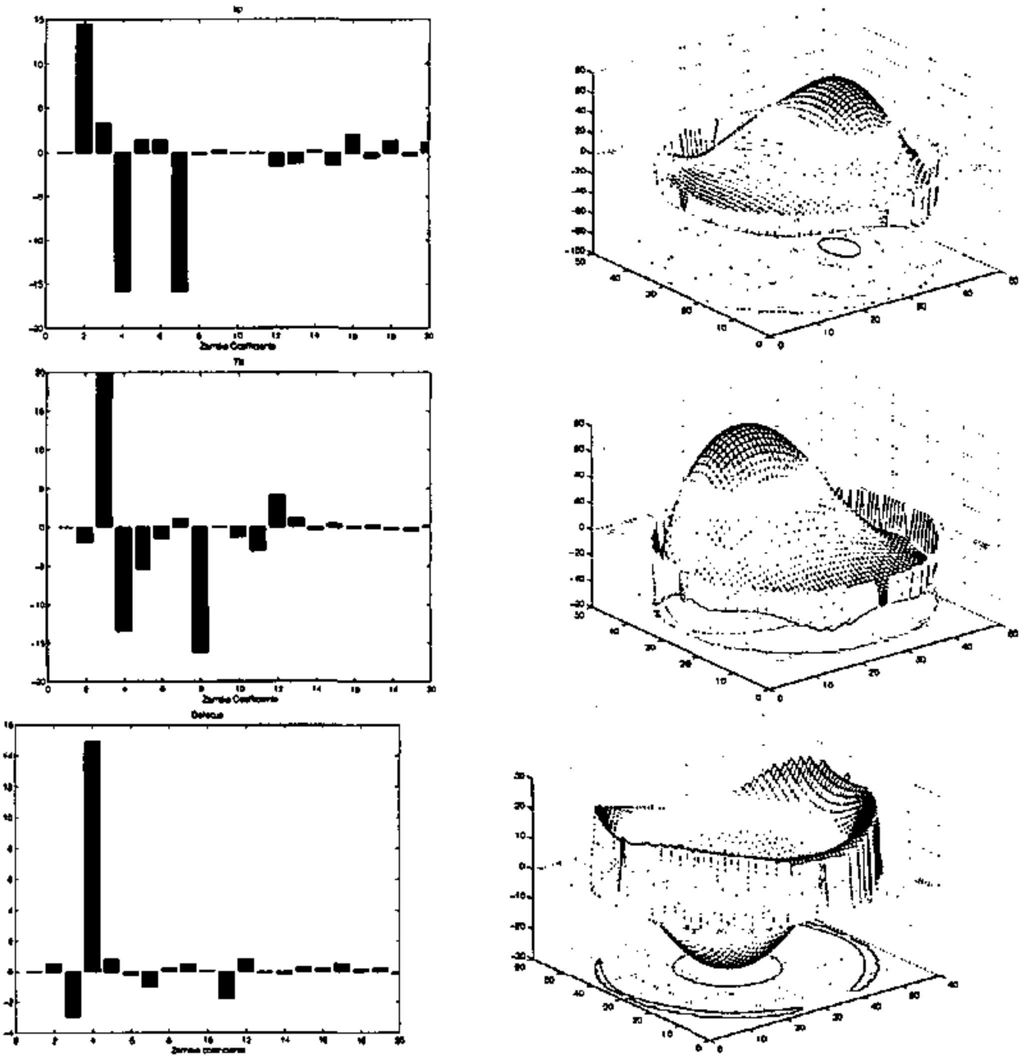

Figure 8.6: Zernike mode 2 to 4

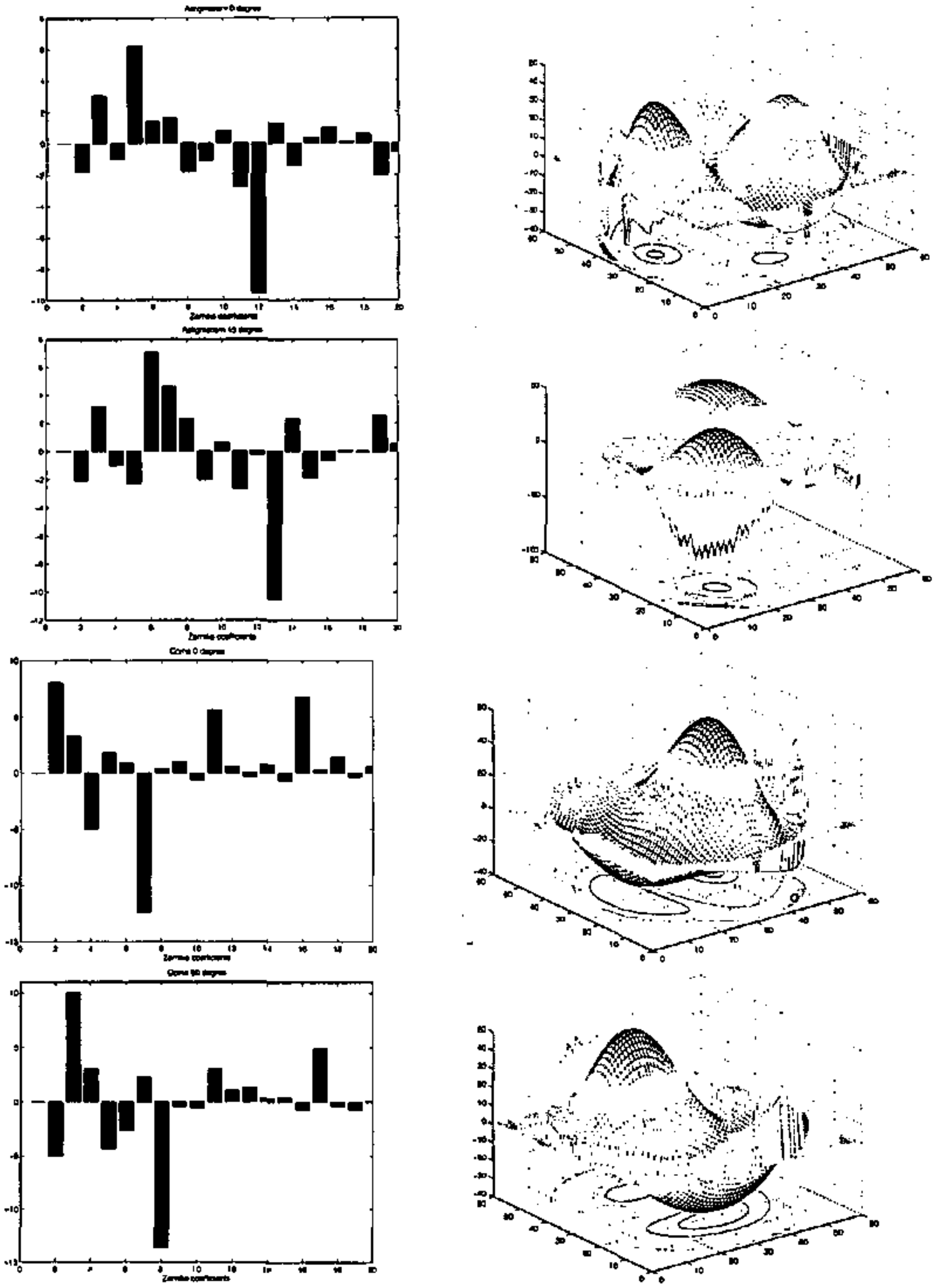

Figure 8.7: simulated Zernike mode 5 to 8

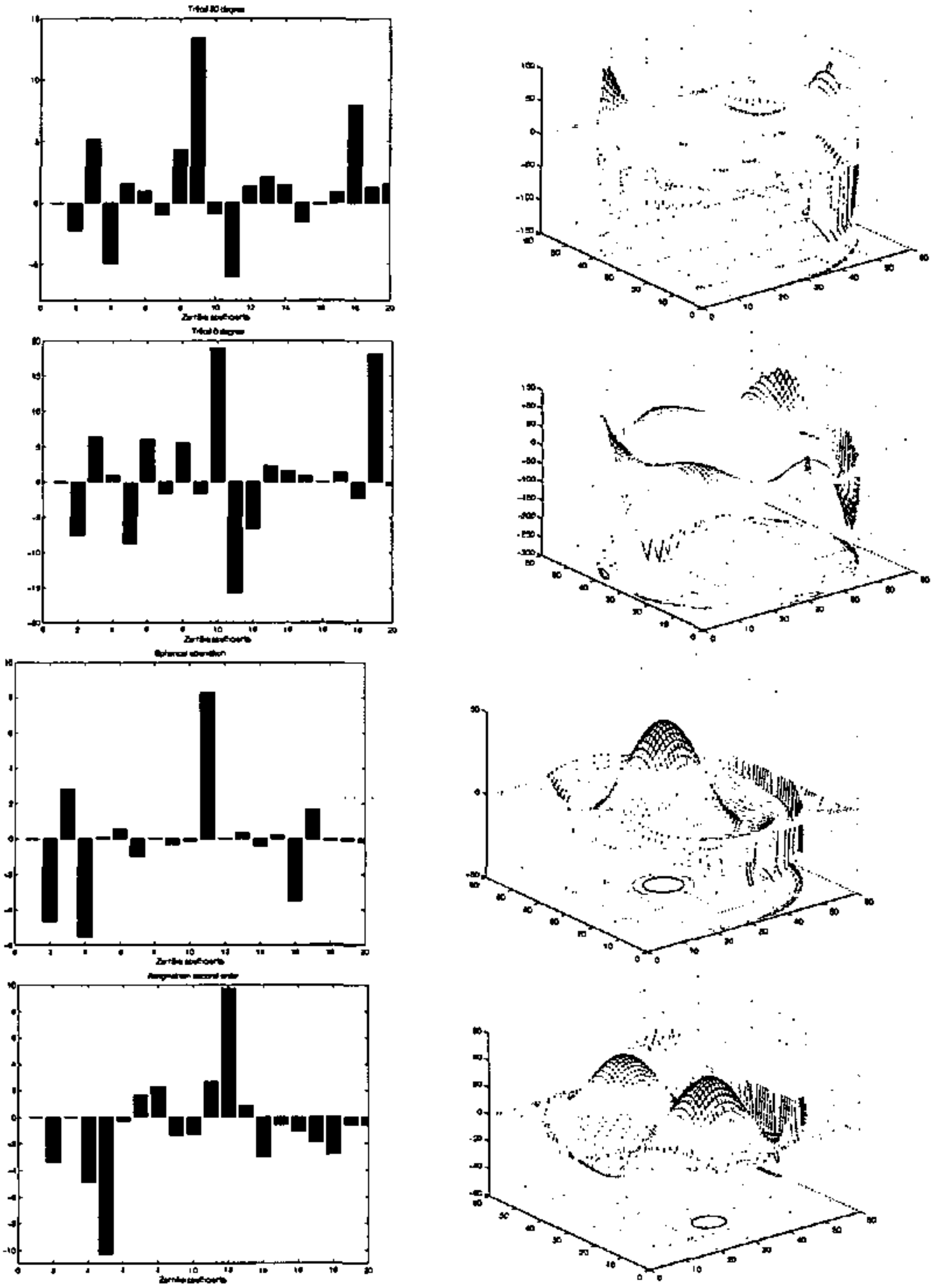

Figure 8.8: Zernike mode 9 to 12

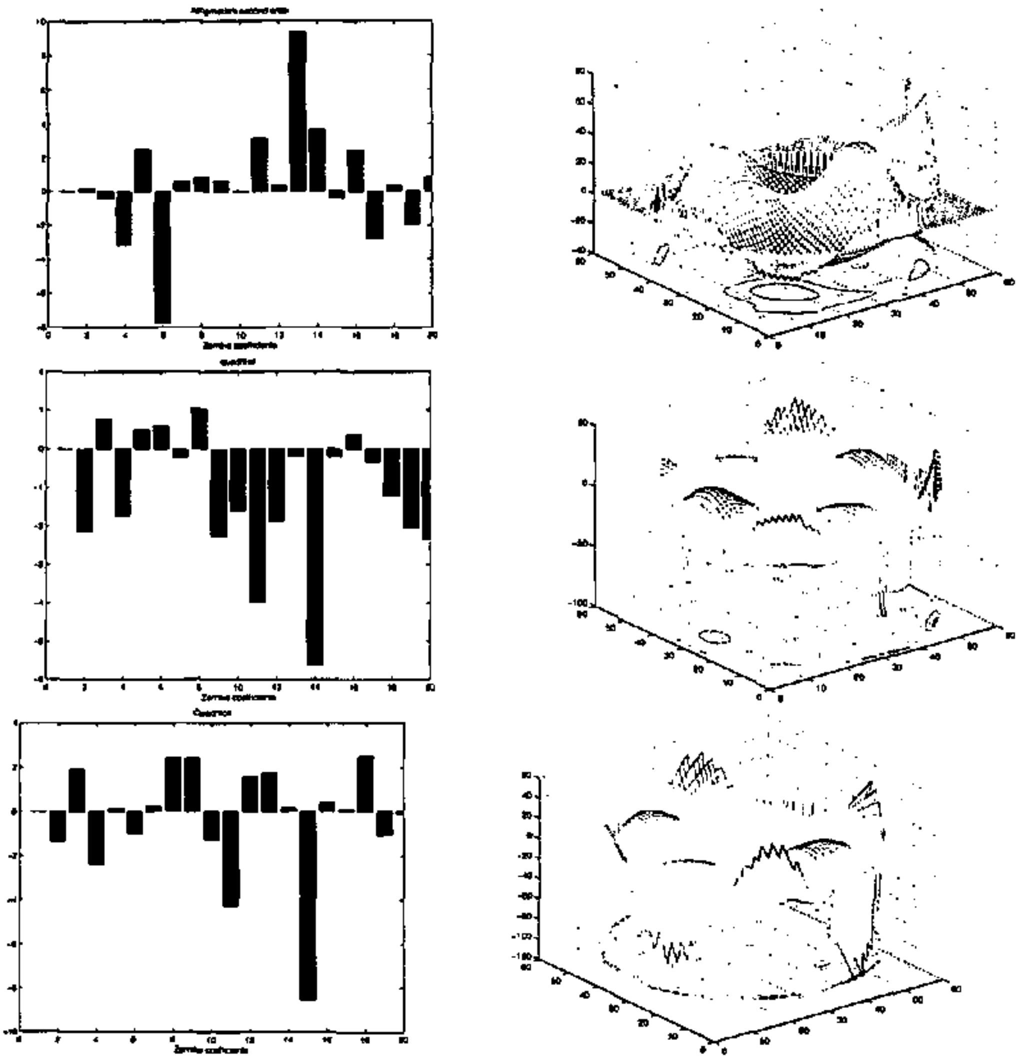

Figure 8.9: Zernike mode 13 to 15

Chapter 9

Acknowledgments

I would like to thanks people, which helped me or supported me in the achievement of this work.

- Professor Dändliker, which proposed me a Ph.D. assistant position for the accomplishment of the MOSIS project and also for the fruitful informations he gave me being my thesis adviser.
- Professor Herzig, which accepted to be part of the jury and for all the discussions we had especially about fiber switch and micro-optics.
- Professor Dainty, as a member of the jury but before all, for all the explanations he gave me about the adaptive optics systems.
- Professor Fainman, which accepted to be part of the jury.
- Dr. Vdovin, which developed the membrane mirrors and helped me to understand their behavior.
- Dr. Rochat and Dr. Haroud with who I had an important collaboration for the development of the dynamic coupling doped fiber systems.
- Dr. Courteville, which introduced me to the C and C++ programming, for its help about the concepts of the algorithms and for all the professional and friendly discussions.
- Dr. Paterson which explained me the behavior of the Shack-Hartmann sensor and how to program them.
- Dr. Peter for our collaboration on the fiber switch.
- The people who worked on the MOSIS project and with who I had an important collaboration

- Dr. Salvade and Dr. Bouvier, as being my office-mates and therefore which supported all my slang words against my P.C., but also for all the helpful solutions you gave me and for your friendship.
- Mme Philipoussis, M. Nussbaum, M. Groccia, which helped me on the technical problem as the micro-lenses fabrications or electronics connections.
- M. Manzardo, Mlle Clement, and other colleagues with who I got many fruitful discussions.
- All my colleagues of the Applied optics group and all the IMT administrative staff, which helped me so well.
- Dr. Collings, which selected me for this Ph.D. position and introduced me to the world of adaptive optics.
- and Finally to all my friends and my family which supported me and helped me.

To all, Thanks a lot.

Bibliography

[1] Alves C., Aing P., Pauliat G., Roosen G., "Prospects of photorefractive memories for optical processing" Optical Memory and Neural Networks 3, 167-189, 1994.

[2] An X., Psaltis D., "Experimental characterization of an angle-multiplexed holographic memory" Opt. Lett. **20**, 1913-1915, 1995.

[3] Artzner G., "Microlens array for Shack-Hartmann wavefront sensors" Opt. Eng. **31**, 1311-1321, 1992.

[4] Ashkin A., Boyd D. D., Dziedzic J. M., Smith R. G., Ballman A. A., Levinstein H. J., Nassau K., "Optically-induced refractive index inhomogeneities in $LiNbO_3$ and $LiTaO_3$" Appl. Phys. Lett. **9**, 72, 1966.

[5] Babcock H. W., "The possibility of compensating astronomical seeing" Pub. Astron. Soc. Pac. **65**, 229, 1953.

[6] Bifano T.G., Mali R. K., Dorton J.K., Perreault J., Vandelli N., Horenstein M.N., Castanon D.A., "Continuous-membrane mirror surface-micromachined silicon deformable mirror" Opt. Eng. **36**, 1354-1360, 1997.

[7] Bishop D. J., Giles C. R., Das S. R., "The rise of optical switching" Scientific American **284**, 88-94, 2001.

[8] Born M., Wolf E., "Principle of Optics" Ch. 1, Cambridge university Press 6th edition, 1997.

[9] Born M., Wolf E., "Principle of Optics" Ch. 9, Cambridge university Press 6th edition, 1997.

[10] Campbell S., Yeh P., "Sparse-wavelength angle-multiplexed volume holographic memory system: analysis and advances" Appl. Opt. **35**, 2380-2387, 1996.

[11] Chen F. S., LaMacchia J. T., Frazer D. B., "Holographic storage in Lithium Niobate" Appl. Phys. Lett. **13**, 223-225, 1968.

[12] Courant R., Hilbert D., "Methods of mathematical physics" Vol.1, Interscience Publishers, 1953.

[13] Cubalchini R., "Modal wavefront estimation from phase derivative measurements" J. Opt. Soc. Am. **69**, 972-977, 1979.

[14] Dai G. M., "Modal wave-front reconstruction with Zernike polynomials and Karhunen-Loeve functions" J. Opt. Soc. Am. A **13**, 1218-1225, 1996.

[15] d'Auria L., Huignard J. P., Slezak C., Spitz E., "Experimental holographic read-write memory using 3-D storage" Appl. Opt. **13**, 808-818, 1974.

[16] Denz C., Pauliat G., Roosen G., Tschudi T., "Volume hologram multiplexing using deterministic phase encoding method", Opt. Com. **85**, 171-176, 1991.

[17] Denz C., Pauliat G., Roosen G., Tschudi T., "Potentialities and limitations of hologram multiplexing by using the phase coding technique" Appl. Opt. **31**, 5700-5705, 1992.

[18] Denz C., Muller K.-O., Heimann T., Tschudi T., "Volume holographic storage demonstrator based on phase coded multiplexing" IEEE Jour. Selec. Top. in Quant. Elec. **4**, 832-839, 1998.

[19] Demerle M., Madec P.-Y., Rousset G., "Servo-loop analysis for adaptive optics" Adaptive Optics for Astronomy, Ed. Alloin & Mariotti, NATO ASI Series C vol. 423, Kluwer Academic publishers, 73-88, 1994.

[20] Fogel D. B., "An introduction to simulated evolutionary optimization", IEEE Trans. on Neural Networks **5**(1) 3-13 ,1994.

[21] Ford J. E., DiGiovanni D. J., "1×N fiber bundle scanning switch" IEEE Phot. Tech. Lett. **10**, 967-969, 1998.

[22] Fujita H., Toshiyoshi H., "Micro-optical devices" handbook of microlithography, micromachining and microfabrication, Rai-Choudhury Edition, SPIE, 435-516, 1997.

[23] Gabor D., "A new microscope principle" Nature **161**, 777, 1948 .

[24] Gabor D., Stroke G. W., "The theory of deep holograms" Proc. Royal Soc. London A, **304**, 275-289, 1968.

[25] Gale M. T., Rossi M., "Continuous relief diffractive lens and microlens array", Ch. 4, Diffractive optics for industrial and commercial applications, Turenen J. and Wyroswski (Eds.), Akademie Verlag Berlin, 1997.

[26] Gilmozzi R., Dierickx P., "OWL concept study" ESO Messenger **100**, 1-10, June 2000.

[27] Goodman J. W., "Introduction to Fourier optics" Ch. 9, McGraw-Hill ed., 1996.

[28] Gradshteyn I. S., Ryzhik I. M., "Tables of integrals, series, and products" Ch. 3, Academic press, 1980.

[29] Grosso R. P., Yellin M. J., "The membrane mirror as an adaptive optical element" J. Opt. Soc. Am. **67**, 399-406, 1977.

[30] Hagelin P. M., Krishnamoorthy U., Heritage J. P., Solgaard O., "Scalable optical cross-connect switch using micromachined mirrors" IEEE Phot. Tech. Lett. **12**, 882-884, 2000.

[31] Hardy J. W., "Adaptive Optics for astronomical telescope" Ch. 5, Oxford University Press, 1998.

[32] Hartmann J., Z. Instrumentenkd. **20**, 47, 1900.

[33] Harwit M., Sloane N. J. A., "Hadamard transform optics" Ch. 1, Academic Press, 1979.

[34] Herrmann J., "Cross coupling and aliasing in modal wave-front estimation" J. Opt. Soc. Am. **71**, 989-992, 1981.

[35] Hong J. H., McMichael I., Chang T. Y., Christian W., Paek E. A., "Volume holographic memory systems: techniques ans architectures" Opt. Eng. **34**, 2193-2203, 1995.

[36] Hubin N., Le Louarn M., Sarazin M., Tokovinin A., Viard E., " New challenges for adaptive optics: the OWL 100 m telescope" SPIE **4007**, 1100-1107, 2000.

[37] Huignard J.-P., Gunter P., "Optical processing using wave mixing in photorefractive crystals", Photorefractive Material and their application II, ed. P. Gunter and J.-P. Huignard, Springer-Verlag, 205-273, 1988.

[38] Jain K. A., "Fundamentals of digital signal processing" p.155, Prentice-Hall, 1988.

[39] Johaness H., "The history of the EIDOPHOR large screen television projector" Gretag Aktiengesellschaft, 1989.

[40] Kapron F. P., Keck D. B., Maurer R. D., "Radiation losses in glass optical waveguides" Appl. Phys. Lett. **17**, 423, 1970.

[41] Kim C. J., Shannon R. R., "Catalog of Zernike polynomials" Applied Optics and Optical Engineering Vol. X , Academic press, 1987.

[42] Kogelnik H., "Couple wave theory for thick hologram gratings" Bell Sys. Tech. J. **48**, 2909-2947, 1969.

[43] Kurz H., "Photorefractive recording dynamics and multiple storage of volume holograms in photorefractive $LiNbO_3$" Opto. Acta **24**, 463-473, 1977.

[44] Kuz'minov Y. S., "Lithium Niobate crystal" Cambridge International Science Publishing, 1999.

[45] Ladany I., "Laser to single-mode fiber coupling in the laboratory" Appl. Opt. **32**, 3233-3236, 1993.

[46] Leith E. N., Kozma A., Upatnieks J., Marks J., Massey N., "Holographic data storage in three-dimensional media" Appl. Opt. **5**, 1303-1311, 1966.

[47] Lin L. Y., Goldstein E. L., Tkach R. W., "On the expandability of free-space micromachined optical cross connects" J. Light Wave Tech. **18**, 482-489, 2000.

[48] Lin L. Y., Goldstein E. L., Tkach R. W., "Free-space micromachined optical switches for optical networking" IEEE J. Select. Topics Quantum Electron. **5**, 4-9, 1999.

[49] Linnick, "On the possibility of reducing the influence of atmospheric seeing on the image quality of stars" Optika i Spectroskopija, **3**, 401, 1957.

[50] Love G.D., "Wavefront correction and production of Zernike modes with a liquid crystal spatial light modulator" Appl. Opt. **36**, 1517-1524, 1997.

[51] Luthy W., Weber H. P., "High-power monomode fibre lasers" Opt. Eng. **34**, 2361-2364, 1995.

[52] Lyon R. G., Hollis J. M., Dorband J. E., Murphy T. P., "Extrapolating HST lessons to NGST" Opt. & Phot. News 35-39, 07/1998.

[53] Madec P.-Y., "Control technics" Adaptive Optics in Astronomy ed. Roddier F., Cambridge U. Press, 131-154, 1999.

[54] Mahajan V. N., "Zernike annular polynomials for imaging systems with annular pupils" J. Opt. Soc. Am. **71**, 75-85, 1981.

[55] Maiman, T.H., "Optical and microwave-optical experiments in Ruby" Phys. Rev. Lett. **4**, 564-,1960.

[56] Malacara D., Malacara Z., "Handbook of lens design" Ch. 9, Marcel Dekker, Inc, 1994.

[57] Malacara D., "Optical Shop testing" John Wiley & Sons, Inc 2nd edition, 1992.

[58] Manhart S., Vdovin G., Collings N., Sodnik Z., Nikolov S., Hupper W., "MEMs deformable mirror for wavefront correction of large telescopes" Proc. ICSO 2000, 407-415, 2000.

[59] Marxer C., de Rooij N. F., "Micro-opto-mechanical 2X2 switch for single mode fibers based on plasma etched silicon mirror and electrostatic actuations" IEEE Jour. Light. Tech. **17**, 2-6,1999.

[60] McMichael I., Christian W., Pletcher D., Chang T. Y., Hong J. H., "Compact holographic storage demonstrator with rapid access" Appl. Opt. **35**, 2375-2379, 1996.

[61] Merkle F., Freischlad K., Bille J., "Development of an optical mirror for astronomical applications" Proc. ESO Conf. Garching, 41-52, 03/1981.

[62] Miyazaki T., Inagaki K., Karasawa Y., Yoshida M., "A high power Nd-doped double-clad fibre a 1.06 μm" SPIE **2699**, 254-265, 1996.

[63] Mok F.H., "Angle-multiplexed storage of 5000 holograms in lithium Niobate" Opt. Lett. **18**, 915-917, 1993.

[64] Morse P. M., "Vibration and sound" American Institute of Physics reprint from 1936, 1983.

[65] Morse P.M., Ingard K.U., "Theoretical acoustics" Princeton University Press, 1968.

[66] Neilson D. T. et al., "Fully provisioned 112×112 micro-mechanical optical crossconnect with 35.8 Tb/s demonstrated capacity" Optical Communication Fiber OSA Conference, Baltimore, 2000.

[67] Noll R. J., "Zernike polynomials and atmospheric turbulence" J. Opt. Soc. Am. **66**, 207-211, 1976.

[68] Noll R. J., "Phase estimates from the slope-type wave-front sensors" J. Opt. Soc. Am. **68**, 139-140, 1978.

[69] Nussbaum P., Gonté F., Boillat C. Herzig H.P., "Low NA fused silica refractive microlenses for Shack-Hartmann wavefront sensor" OSA topical meeting on diffractive optics and micro-optics, Quebec,247-249, 2000.

[70] Paterson C., Munro I., Dainty J. C., "A low cost adaptive optics system using a membrane mirror" Opt. Express **6**, 175-185, 2000.

[71] Paterson C., Munro I., Dainty J. C., "A low cost adaptive optics system" Proc. Adaptive optics for industry and medicine, World Scientific, 305-310, 1999.

[72] Pfund J., Lindlein N., Schwider J., "Misalignment effects of the shack-Hartmann sensor" Appl. Opt. **37**, 22-27, 1998.

[73] Rippin D. J., Goldberg L., "High efficiency side-coupling of light into optical fibers using embedded V-grooves" Electron. Lett. **30**, 863-865, 1995.

[74] Rochat E., Dändliker R., Haroud K., Czichy R. H., Roth U., Costantini D., Holzner R., "Fiber amplifiers for coherent space communication" IEEE J. Select. Topics Quantum Electron. **7**, 64-80, 2001.

[75] Rochat E. & al., "High power Nd^{3+} doped fiber amplifier for coherent intersatellite links" J. Quant. Electron. **35**, 1419-1423, 1999.

[76] Roddier F., "Curvature sensing and compensation: a new concept in adaptive optics" Appl. Opt. **27**, 1223-1225, 1988.

[77] Roddier F., "Adaptive optics in Astronomy" Cambridge university press, 1st edition, 1999.

[78] Rousset G. and Beuzit J.-L., "The COME-ON/ADONIS systems" Adaptive optics in astronomy, Edit. Roddier F., Cambridge University Press, 1999.

[79] Rousset G., "Wavefront sensing" Adaptive optics for Astronomy, Edit. by D.M. Alloin & J.-M. Mariotti, NATO ASI Series, 115-137, 1993.

[80] Rousset G., Fontanella J. C., Kern P., Gigan P., Rigaut F., Lena P., "First diffraction limited astronomical images with adaptive optics" Astron. Astrophys. **230**, L29-L32, 1990.

[81] Saleh B. E., Teich M. C., "Fundamentals of photonics" John Wiley & Sons, 1st edition 1991.

[82] Shack R. B., Platt, B. C., "Production and use of lenticular Hartmann screen" J. Opt. Soc. Am. **61**, 656, 1971.

[83] Siegman A. E., "lasers" University Sciences Books, 1986.

[84] Snitzer E., Po H., Hakimi F., Tumminelli R., Mac Collum B. C., "Double clad offset core Nd fiber laser" Dig. Conf. on Optical Fiber Sensors, Paper PD5, 1988.

[85] Southwell W. H., "Wave-front estimation from wave-front slop measurements" J. Opt. Soc. Am. **70**, 998-1006, 1980.

[86] Staebler D. L., Burke W. J. Phillips W., "Multiple storage and erasure of fixed holograms in Fe-doped $LiNbO_3$" Appl. Phys. Lett. **26**, 182-184, 1975.

[87] Strasser A. C., Maniloff E. S., Johnson K. M., Goggin S. D. D., "Procedure for recording multiple-exposure holograms with equal diffraction efficiency in photorefractive media" Opt. Lett. **14**, 6-8, 1989.

[88] Taketomi Y., Ford J. E., Sasaki H., Fainman J. M., Lee S. H., "Incremental recording for photorefractive hologram multiplexing" Opt. Lett. **16**, 1774-1776, 1991.

[89] Taranenko V. G., Koshelev G. P., Romanyuk N. S., "Local deformation of solid mirrors and their frequency dependence" J. Sov. Opt. Tech. 48, 650-, 1981.

[90] Timoshenko S., Woinowsky-Krieger S., "Theory of plates and shells " McGraw-Hill Book Company, Inc., 1959.

[91] Turing A. M., "Computing machinery and intelligence" Mind, **59**, 433-460, 1950.

[92] Tyler G. A., Fried D. L., "Image position error associated with a quadrant detector" J. Opt. Soc. Am. **72**, 804-808, 1982.

[93] Tyndall J., Royal Institution of Great Britain Proceedings, **6**, 189, 1870-72.

[94] Tyson R.K., "Principle of adaptive optics" Academic Press, 2nd ed., 1991.

[95] van Heel A. C. S., "A new method of transporting optical images without aberrations" Nature, **173**, 39, 1954.

[96] van Heerden P. J., "Theory of optical information Storage in Solids" Appl. Opt. **2**(4), 393-400, 1963.

[97] Vdovin G., Sarro P. M., "Flexible mirror micromachined in silicon" Appl. Opt. **34**, 2968-2972, 1995.

[98] Vdovin G., Saro P. M., Middelhoek S., "Technology and applications of micromachined adaptive mirrors" J. Miromech. Microeng. **9**, R8-R19, 1999.

[99] Vdovin G., Middelhoek S., Sarro P. M., " Technology and applications of micromachined silcon adaptive mirrors" Opt. Eng. **36**, 1382-1390, 1997.

[100] Verdeyen J. T., "Laser electronics" Prentice Hall International Editions, 3rd edition 1995.

[101] Wilson R. N., "Reflecting telescope optics I", Ch. 1, Springer-Verlag, 1996.

[102] Yang X., Wen Z., Xu Y., Li N., "Hadamard codes of m≠2" in phase-code multiplexed holographic memories" Opt. Eng. **35**, 3639-3641, 1996.

[103] Yariv A., "Optical electronics" Saunders College Publishing, 4th edition, 1991.

[104] Yariv A., Yeh P., "Optical waves in crystal" , Ch.4, John Wiley & Sons, 1984.

[105] Yariv A., Yeh P., "Optical waves in crystal" , Ch.7, John Wiley & Sons, 1984

[106] Yeh P., "Introduction to photorefractive nonlinear optics" Ch. 1, John Wiley & Sons, 1993.

[107] Yeh P., "Introduction to photorefractive nonlinear optics" Ch. 3, John Wiley & Sons, 1993.

[108] Yeh P., "Introduction to photorefractive nonlinear optics" Ch. 4, John Wiley & Sons, 1993.

[109] Yeh P., "Introduction to photorefractive nonlinear optics" ,Ch8, John Wiley & Sons, 1993.

[110] Yin S., Zhou H., Zhao F., Wen M., Yang Z., Zhang J., Yu F. T. S., "Wavelength multiplexed holographic storage in sensitive photorefractive crystal using a visible light tunable diode laser" Opt. Com. **101**, 317-321, 1993.

[111] Yoon G. Y., Jitsuno T., Nakatsuka M. Nakai S., "Shack Hartmann wave-front measurement with a large F-number plastic microlens array" Appl. Opt. **35**, 188-192 , 1996.

[112] Yu F. S., Wu S., Mayers A., Rajan S., Gregory D. A., "Color holographic storage in $LiNbO_3$" Opt. Com. **81**, 348-352, 1991.

[113] Zernike. F., "Beugungstheory des schneidenverfahrens und seiner verbesserten form, der phasenkontrastmethod", Physica, **1**, 689-704, 1934.

[114] Zhu L., Sun P.-C., Bartsch D.-U., Freeman W. R., Fainman Y., "Wave-front generation of Zernike polynomial modes with a micromachined membrane deformable membrane mirror" Appl. Opt. **38**, 6019-6023, 1999.